Stony Brook University

Super-hydrophobic metallic surface formation by short pulsed lasers

A Thesis Presented

by

Di Liu

to

The Graduate School

in Partial Fulfillment of the

Requirements

for the Degree of

Master of Science

in

Mechanical Engineering

Stony Brook University

December 2013

Stony Brook University

The Graduate School

Super-hydrophobic metallic surface formation by short pulsed lasers

Di Liu

We, the thesis committee for the above candidate for the

Master of Science degree, hereby recommend

acceptance of this thesis.

Dr. David Hwang – Thesis Advisor
Assistant Professor, Mechanical Engineering

Dr. Jon Longtin – Second Reader
Professor, Mechanical Engineering

Dr. Carlos Colosqui – Third Reader
Assistant Professor, Mechanical Engineering

This thesis is accepted by the Graduate School

Charles Taber
Dean of the Graduate School

Abstract of the Thesis

Super-hydrophobic metallic surface formation by short pulsed lasers

by

Di Liu

Master of Science

in

Mechanical Engineering

(Laser material processing and heat transfer)

Stony Brook University

2013

Surface texturing in micro/nanoscale plays an important role in many application fields including enhanced light trapping in solar cell, self-cleaning and anti-icing surfaces by achieving super-hydrophobicity in wind turbine and airplane wings, and enhanced convective and radiative heat transfer from surface. For metals such as copper and stainless steel which have been widely used in modern industries, formation of super-hydrophobic surfaces can offer significant benefits in terms of reliable and efficient operation by enabling, for instance, surfaces free from corrosion, contamination, freezing, and crack with improved heat dissipation.

Super-hydrophobic surface is a highly hydrophobic surface typically with water contact angle exceeding 150 °and roll off angle or hysteresis smaller than 10 °, which is also known as Lotus Effect®. Formation of super-hydrophobic surface has been an area of very active research, typically falling into two representative categories: inducing physical roughness in micro/nanoscale, and modification of surface energy by coating method, which are frequently mixed in most practical applications. Laser structuring on the metallic surfaces has been examined to generate surface roughness in micro, even nanoscale to form super-hydrophobic surface utilizing the very limited heat affected zone by ultrashort pulses yet mainly with extra surface chemical treatment or coating to reduce surface energy.

This study will demonstrate high flexibility and control precision offered by the efficient and economic pulsed laser scanning method. Compared with conventional laser-based approach, nanosecond laser scanning method tested corresponds to a highly cost-effective and uniform means for the texturing of arbitrary sample area with excellent precision. Nanosecond pulsed

lasers are employed to scan over the copper, stainless steel and aluminum surfaces for micro/nano patterning and thereby formation of hierarchical structures towards high water repellence (Super-hydrophobicity) and stabilization. Achievement of super-hydrophobic surfaces involves complex surface oxidation mechanisms. For copper, CuO was formed during laser irradiation and deoxidized to Cu_2O which is key to super-hydrophobic phenomenon. For stainless steel, it is believed that carbon is involved with the surface wettability shift.

Relevant texturing mechanisms are explained based on advanced characterization by scanning electron microscope (SEM) and surface chemical composition analysis using Energy Dispersive X-ray Spectroscopy (EDS). Static contact angle and dynamic contact (i.e. hysteresis) indicating water wettability and surface homogeneity were also observed and analyzed by contact angle measurement.

TABLE OF CONTENTS

LIST OF FIGURES

LIST OF TABLES

ACKNOWLEDGMENTS

I would like to thank my research advisor, Prof. David J. Hwang for his guidance and support throughout my study and work for last a few years. His useful and professional opinions helped me complete this thesis. His in-depth knowledge and rich experiences provided me many different views, ways of thinking and inspirations.

I would also like to express my gratitude to Prof. Jon Longtin, Prof. Dong Yu and Dr. Fernando Camino (in CFN/BNL) for their huge support of lab equipment and tools, constructive advises and effective solutions to my questions.

Last but not the least, I am also very grateful to my colleagues Mr. Tao Zhang, Mr. Matthew Quigley and all other members of Laser Solar PV laboratory. I also want to thank all other students who spent time with me for discussion and exploration.

Chapter 1: Introduction

Metals such as copper and stainless steel are important materials used in modern industries because of their excellent electrical and thermal conductivities, relatively nonreactive chemical properties and mechanical workability. In order to mitigate one of the main problems for metals , corrosion issues, formation of water super-hydrophobic metal surface can dramatically reduce the water attachment and thereby contamination and corrosion [1, 2]. The other problem is atmospheric icing occurring when super-cooled water droplets come into contact with exposed metal surfaces, which will in turn cause material damage and socioeconomic cost such as in aircraft and boats. Super-hydrophobic surface on the metal has proven to be efficient in reducing accumulation of snow and ice, even completely preventing formation of ice [3, 4].

Fabrication of functional surfaces such as super-hydrophobic surfaces is a hot topic. Abundant research has been active to address issues on forming super-hydrophobic surfaces. Such surfaces with super-hydrophobicity exhibit micro-/nano-structures covered with low surface energy material. The surface micro-/nano-scale structures amplify the hydrophobicity property, leading to high water repellence (super-hydrophobicity) which only allows water to possess an extreme high contact angle (larger than 150 °) with a surface. Thus water is easy to roll off the surface and leave a dry and clean surfaces. There are also many researches to fabricate surfaces with low friction coefficient, such as a surface with largely improved lubrication in a sliding motion by introducing dimples in one of the surfaces for wet contact and a surface with reduction of friction coefficient by covering with tiny pillars to reduce contact area for dry contact. Other topics including optical properties modification such as generating surfaces with diffraction gratings or enhanced light trapping functions, the latter of which can be applied for anti-glare device and photovoltaic devices. Other fields for example the biomedical applications, functional surfaces can be fabricated to improve cell adhesion.

Super-hydrophobicity or ultra-hydrophobicity is also well known as Lotus Effect® [5], which has high water repellence (contact angle larger than 150 °) sometime with very low contact angle hysteresis (the difference between water advancing and receding angle). This super-hydrophobicity phenomenon was also found on the wings of butterflies [6]. Water droplet does not adhere to lotus or insect wing's surface, rolling off the surface carrying away dust particles which works as perfect self-cleaning function. Surfaces with this interesting self-cleaning functions can be used to number of applications such as fabricating such surfaces for satellite dishes, solar panel, exterior architectural glass on a green house, and heat transfer surfaces in air conditioning equipment. Super-hydrophobic surfaces may also possess the ability to prevent ice or frost formation or adhesion. Besides, the fact that low hysteresis on super-hydrophobic surfaces suggests applications such as microfluidics and piping. The high water repellence has been claimed in biomedical applications ranging from blood vessel replacement to wound management. [7]

A lot of investigations and study showed that surface wettability was governed by two main factors: (Chemically) low surface energy chemical composites and (Physically) surface roughness in micro/nanoscale [5, 7, 8]. Increasing surface roughness by itself will make hydrophobic surface more water repellent and hydrophilic surface more water wetting (based on Wenzel state). However, in some cases air pocket formation can change a hydrophilic surface to hydrophobic surface [9] (Cassie-Baxter state). Wenzel determined that when water has intimate contact with micro-structured surface (Wenzel State [10]) - water fully wets the surface including the gaps between asperities- the hydrophobic surfaces become more hydrophobic while hydrophilic become more hydrophilic. The phenomenon of air pocket formation between asperities describing water droplet is suspended on the tops of asperities was claimed as Cassie-Baxter state [11] by Cassie and Baxter. One way to determine which state is more likely to exist, by minimization of free energy argument, is the relation that predicts the smaller new contact angle [12]. Recent new criteria for the Cassie-Baxter state to exist are 1). Contact line forces overcome body forces of unsupported droplet weight and 2). The microstructures are tall enough to prevent the liquid that bridges microstructures from touching the base of the microstructures [13]. Now considering water stays in smooth and flat surface without any surface roughness, study shows that theoretically, the water lowest possible contact angle is 0 °and highest possible angle is about 120 °for surface covered by densely packed of CF_3 groups [14, 15] and other fluoropolymers, such as PTFE (Teflon®) [16].

In recent years, many researches have been undertaken to form super-hydrophobic surfaces. Techniques being used to process material in order to make super-hydrophobic surfaces based on previous discussion can simply divided into two categories [23]: 1. Making a rough surface from a low surface energy material, 2. Modifying a rough surface with a material of low surface energy. For example, some natural and artificial super-hydrophobic textiles and fibres of the order of micrometers or even smaller themselves can be roughened to enhance the effect. Some research has been carried out on improving the hydrophobicity of woven textiles and non-woven mats of electrospun fibres were found to be super-hydrophobic and can be produced with very small diameters [17, 18]. Etching also can be used to increase surface roughness and in many cases combined with other roughness generation methods to create multiple roughness scales [19, 20].

Laser processing have been proven to be an effective non-contact material processing techniques to texture the surface. The current interest in the use of lasers as a material processing tool is directly linked to the unique properties of laser light, no matter for scientific investigations or for industrial applications. The high spatial coherence of laser beams allows extreme focusing and directional irradiation at various laser energy densities. The monochromaticity of laser light gives the possibility of highly selective narrow-band excitation depend on the material being processed and the wavelength of the laser light. Controlled pulsed excitation offers high temporal resolution (nanosecond, picosecond, femtosecond pulses) and often makes it to minimize heat

diffusion depth (small heat affected zone especially for ultrashort pulses). The combination of all these properties offer a wide range of quite different applications. [21, 22]

Based on established experimental and theoretical works, by controlling the laser output energy density and adjusting laser parameters laser can safely process silicon, metals, ceramics, polymers and other crystalline structures [22]. A lot of study have performed to understand the effect of laser processing parameters on surface morphology such as laser fluence, number of incident pulses and focus position [23, 24, 25] for ultrashort lasers because of its minimized heat affected zone.

However, using laser or other methods to roughen the surface, at most cases, requires post-processing modification of the surface chemistry by covering low surface energy materials to achieve super-hydrophobicity. One of the drawbacks of these super-hydrophobic surfaces is that they are fragile, despite of their good performance of large contact angle (above 160 °) [26].

Compared with other laser-based approaches, nanosecond pulsed lasers scanning method employed here corresponds to a highly cost-effective and uniform means for the texturing of arbitrary sample area and shape in micro/nanoscale without further chemical treatment to reduce surface energy, leading to stable super-hydrophobicity performance on metallic surfaces after placing in the air environment for certain period.

In chapter 2, this thesis will provide the fundamental background and theories about water wettability, definition of contact angle, hydrophilic, hydrophobic and super-hydrophobicity (Lotus Effect®). Related surface tension, Young's equation and two different widely used models regarding water contacting with micro-structured surfaces are also reviewed here.

In chapter 3, there will be introduction of state-of-art super-hydrophobic surfaces fabrication techniques including fabricating of super-hydrophobic materials like textiles, fibres and particles targeting low surface free energy materials, developing roughened surface in small scales and large area using templating, etching, crystal growth and laser structuring (by femtosecond pulsed laser). Fundamental of laser heating such as laser melting and ablation mechanisms are also discussed.

In chapter 4, a description about the experimental set up including laser material processing system and homemade contact angle measurement platform will be presented. Information of advance analytical tools such as Scanning Electron Microscopy (SEM), Energy Dispersive X-ray Spectroscopy (EDS) and Spectrometer which have been used in this study is also provided. SEM images are playing vital role here to reveal detailed micro/nano structures after laser processing. EDS is responsible for the analyzing the chemical components of the sample surface before/after laser treatment and placing in the air for certain period. Automatic high accuracy X-Y sample translation stages controlled by PC-connected controller was used here for rapid processing. Z-axis motorized stages was employed for precise focal adjustment

which is necessary for generating small scale (micro/nanoscale) structures. Several nanosecond pulsed lasers were employed here to scan on copper and stainless steel surfaces.

In chapter 5, a simple laser beam spot size measurement is presented to measure focused Gaussian laser beam by scanning rapid with pulsed laser on single crystal silicon to isolate each laser pulse. By curve fitting the plotted relation of diameter and pulse energy, original laser beam spot size can be estimated. Different wavelength and power level effect on surface morphology was also investigated on silicon surface by cross-sectional SEM images. Surface wettability performance on copper and stainless steel surfaces ware studied by measuring contact angle of the surfaces. Right after laser processing, surfaces were all super-hydrophilic with contact angle less than 5 °. Super-hydrophobicity was then achieved after laser processing and placing in the air environment for two months. Surface morphology was revealed by Scanning Electron Microscopy (SEM) which showed hierarchical structures developed by irradiation to scanned laser pulses. Surface chemical composites analysis was performed by Energy Dispersive X-ray Spectroscopy (EDS) to further disclose the super-hydrophobicity formation mechanism.

In chapter 6, a conclusion will be made on the advantages of scanning based nanosecond pulsed laser micro-structuring approach to form super-hydrophobic metallic surfaces without further chemical treatment to reduce surface energy. Surface wettability transition from super-hydrophilicity to super-hydrophobicity involved deoxidation of copper oxide and nonpolar carbon deposition on surfaces. The 532 nm green nanosecond laser was proved in this study have a better chance to generate favorable surface structures to induce surface wettability change. By scanning the laser 20mm/s and 10μm line spacing the contact angle of highest 161 °at the power of 2.5W was achieved.

In chapter 7, future work about more detailed study of full set of laser/scanning/focusing parameters, dynamic contact angle measurement and dynamic water behavior on super-hydrophobic surfaces will be conducted. More precise quantitative chemical elements analysis will also be performed to understand the transition mechanism. Focus Ion Beam (FIB) cross sectioning of laser structured metal surface will also be a favor method to reveal the structural and chemical information change along the depth.

In chapter 8, more interesting and promising applications of laser treated metal and semiconductor surfaces are presented. For example, by carefully adjust laser processing parameters, different colored stainless steel was achieved by scanning green nanosecond laser. This application can be expended to fully controllable optical property modification of targeting materials. Another example is that laser-assisted doping of selective emitter on bulk silicon based solar cell with simultaneously textured black surface for enhanced light trapping was achieved by laser induced material diffusion.

Chapter 2: Basic of Super-hydrophobicity

In order to understand super-hydrophobicity, this chapter starts with the concept of surface wetting which is the ability for a liquid to maintain contact with a solid surface. Three interfaces are presented when water contacts with a solid surface: gas-liquid, liquid-solid and gas solid interface. Contact angle θ which is between gas-liquid interface and liquid-solid interface is introduced here as a standard indicator of the degree of surface wetting (surface wettability). Contact angle is considered to be the static measurement of surface wettability and while dynamic measurement is contact angle hysteresis [27] or sliding angle. Super-hydrophobicity mean the contact angle θ exceeds 150 °and sometimes, the contact angle hysteresis or sliding angle is less than 10 °. It is also well know that contact angle of the liquid on the flat surface is related to the surface energy and the surface tension concept is introduced by Thomas Young in 1805 which can be regarded as a force per length [28]. Though the biggest contact angle were observed less than 120 °, by a brilliant method to roughen the surface in micro/nanoscale, contact angle of 160 °or 170 °can be achieved. Two models about water contacting with microstructures on the surface have been developed: Wenzel State; and Cassie -Baxter State. In the latter state, air pockets hidden between the asperities help to suspend the water, not surprisingly achieving less hysteresis or sliding angle than the other one.

2.1 Super-hydrophobic Phenomenon in Nature

Super-hydrophobic phenomenon was first discovered on plant leaves, insect legs [29] and wings [6] while people have spent decades on the biomimetic trying to learn from the our mother nature since she is the greatest engineer in the world. Super-hydrophobicity also refers to Lotus Effect® since the excellent water repellence and self-cleaning properties exhibited on the leaves of lotus resulting from the micro- and nanoscopic hierarchical structures covering with hydrophobic wax (Figure. 2.1.1).

Figure. 2.1.1: Photograph of different superhydrophobic surfaces in nature and corresponding SEM with different magnifications. (a) A walking strider on the water (X. F. Gao et.al., 2004), (b) Lotus Effect (Bhushan et.al., 2009), (c) Butterfly wings (Y. M. Zheng et.al., 2007).

The basis of this high water repellence and self-cleaning properties on the upper side of lotus leaves is its hierarchical surface structure. Compared with other plant species with a hierarchical surface structure composed of papillae and wax crystals, the lotus leaf shows special optimization with robustness structure to reduce damage and provide perfection and durability of the water repellency [30].

2.2 Surface Wetting

Surface wetting is the ability for the liquid to contact with solid surface resulting from intermolecular interactions such adhesive and cohesive forces together with the surface roughness in micro/nanoscale if the solid surface is not smooth. This involves three interfaces: gas-liquid, liquid-solid and gas-solid interface. The contact angle θ is the angle between the gas-liquid interface and liquid-solid interface which shows the degree of surface wetting (Surface Wettability) (Figure. 2.2.1).

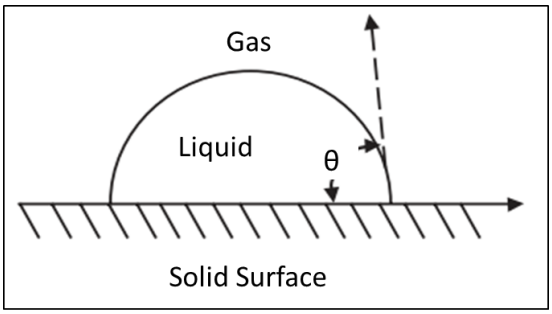

Figure. 2.2.1: Schematic drawing of contact angle.

For water contact with solid, contact angle is less than 90 °means wetting of surface is favorable and water tends to spread a large area on the surface which can be also termed as hydrophilic. When the contact angle is larger than 90 °, the surface wetting is unfavorable and water tends to shrink to maintain truncate sphere shape to minimizing the contact with the solid. This comparison in different contact angle is showed in Figure 2.2.2. Different areas with different water wettability of copper surface show different contact angles (laser processed surfaces and original untreated copper surface).

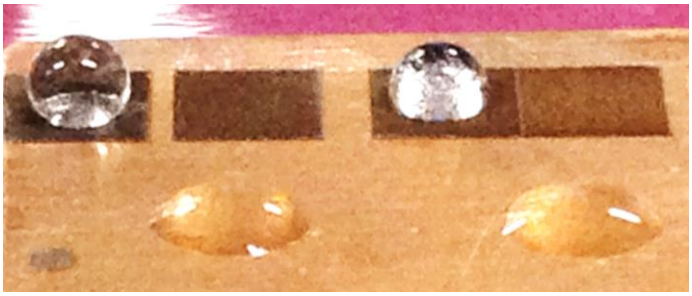

Figure. 2.2.2: Photograph of water droplets contact with copper surface. (Higher contact angle were achieved on laser-structured copper surfaces than on original untreated surface).

Hydrophobicity is the level of the water repellence (non-wetting) when the contact angle is larger than 90 °. When the contact angle exceeds 150 °, the term ultra-hydrophobicity or super-hydrophobicity is used. This phenomenon has been studied for many years because such super-hydrophobic surface possess an excellent ability to repel water, which can be applied for fabrication of self-cleaning surfaces and other promising applications.

2.3 Contact Angle Hysteresis

Contact angle is static measurement of surface wettability while contact angle hysteresis and sliding angle are dynamic measurement [27]. When water is injected and rest on solid surface, contact angle will be formed. As water is kept injected, the droplet will increase in volume as well as contact angle, at the same time, its three phase boundary will remain stationary until it suddenly advances outward. The contact angle of droplet right before advancing outward is termed as advancing angle. The receding contact angle then can be measured by pumping the water out of the droplet. The droplet will decrease in volume as well the contact angle, at the meantime, its three phase boundary will remain stationary until it suddenly recedes inward. The contact angle the droplet right before receding inward is termed as receding angle. So the contact angle hysteresis is the difference between the advancing and receding contact angles and can be used to characterize surface heterogeneity, roughness, and mobility (Figure. 2.3.1).

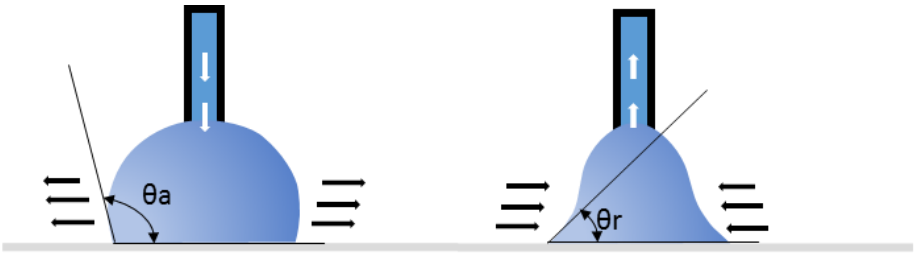

Figure. 2.3.1: Schematic drawing of advancing and receding contact angles.

The sliding angle is another dynamic measurement of hydrophobicity and is measured by depositing a droplet on a surface and tilting the surface until the droplet begins to slide (Figure. 2.3.2). And the advancing angle and receding angle are indicated in the figure respectively. For ideal smooth surface the contact angle hysteresis is zero which means no difference between the two angles. [31]

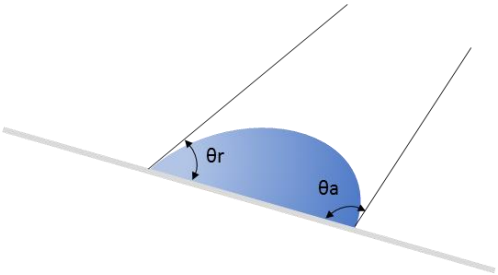

Figure. 2.3.2: Schematic drawing of measuring advancing and receding angles by tilting the plate.

2.4 Surface Energy

There are two major types of solid surfaces regarding contact with liquid. [26] Traditionally, solid surfaces have been divided into high energy and low energy types. The surface energy of a solid has to do with the bulk nature of the solid itself. Solids such as metals, glasses, and ceramics are known as “hard solids” because the chemical bonds within the solid (e.g., covalent, ionic, or metallic) are very strong. Thus, it takes a large input of energy to break these solids so they are termed as high energy. Most molecular liquids achieve complete wetting on surfaces with high energy.

The other type of solids is weak molecular crystals (e.g. fluorocarbons, hydrocarbons, etc.) where the molecules are held together mainly by non-covalent bond and physical forces (e.g. van der Waals and hydrogen bonds). Thus it would take a very low input of energy to break them, and then they are termed as low energy. Depending on the type of liquid chosen, surfaces with low energy can permit either complete or partial wetting.

2.5 Surface Tension and Young’s Equation

When contacting with ideal surface (surface is smooth, flat and homogeneous), the shape of a liquid droplet is determined by the surface tensions of the three interfaces (liquid-gas, liquid-solid and gas-solid interfaces). In a pure liquid such as water, each molecule is pulled equally in every direction by surrounding liquid molecules, resulting zero net force. However, the molecules at the surface do not have surrounding molecules in all directions to provide a balanced net force. Instead, they are pulled inward by other liquid molecules, creating an internal pressure. As a result, the liquid automatically rearranges its surface area to maintain the lowest surface free energy. This intermolecular force to reconstruct the surface is called the surface tension, which is the reason to maintain the liquid droplets shape. In practice, external forces such as gravitational force will deform the droplet shape, thus, the contact angle is determined by a combination of surface tensions of three interfaces and external forces such as gravity.

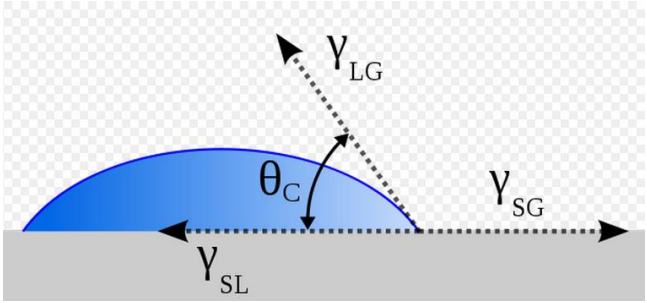

Figure. 2.5.1: Schematic drawing the surface tension balanced to create contact angle without considering the liquid gravity.

Now consider the water droplet formed in the air without contacting to any solid surface but air. Surface tension scales as a function of length ~ R (usually diameter of the spherical water

droplet), whereas gravitational forces scale with the mass of the drop, depending on a length cubed ~ R^3, and the density of the liquid ~ ρ. The ratio of gravitational force to surface tension for a droplet scales as ~ $\rho g R^3/\gamma_{LG} R \sim R^2$ (where g=9.8 m/s^2 is the acceleration due to gravity). The ratio is large when the length is big, but almost vanishes as the length becomes small. This means that the dominant force will change from gravity to surface tension when the characteristic length of the liquid droplet reduces. By equaling the two values: gravitational force and surface tension ($\rho g R^3 = \gamma_{LG} R$), a value R is calculated as 2.73 mm, which is called the capillary length for water. For water droplet diameter much smaller than this value, surface tension will dominate. [15]

When a liquid drop contact with ideal surface, as first described by Thomas Young [28] in 1805, the contact angle is defined by the mechanical equilibrium of the drop under the action of three interfacial tensions (Figure. 2.5.1) and described by follow equation.

$$\gamma_{SG} = \gamma_{SL} + \gamma_{LG} cos\theta \tag{2.1}$$

In Equation 2.1, γ_{SG}, γ_{SL}, γ_{LG} and θ represent the solid-gas, solid-liquid, liquid-gas interfacial tensions and surface contact angle, respectively. Equation 2.1 is usually referred to as Young's equation, and θ is Young's contact angle.

2.6 Wenzel State and Cassie-Baxter State

In practice, solid surfaces are far from this ideal case and relatively more and less rough. Contact angles of the droplet on the real solid surface can be any value between the advancing and receding contact angles (concepts will be provided in next session in this chapter).

Wenzel determined that when the liquid is in intimate contact with a micro-structured surface, contact angle θ will change to θ_{w*}:

$$cos\theta_{w*} = r \cos\theta \tag{2.2}$$

where r is the ratio of the actual surface area to the projected area [10]. Equation 2.2 is usually called Wenzel's equation showing that micro-structures on a surface amplifies the natural wettability of the surface. A hydrophobic surface (original contact angle greater than 90 °) becomes more hydrophobic – its new contact angle θ_{w*} becomes greater than the original contact angle θ. However, a hydrophilic surface (original contact angle less than 90 °) becomes more hydrophilic - its new contact angle becomes less than the original. [33]

Although Equation 2.2 demonstrates that the contact angle of a rough surface is different from the original contact angle, it does not describe contact angle hysteresis. When dealing with a heterogeneous surface, the Wenzel state is not sufficient. A more complex model is needed to measure how the apparent contact angle changes when various materials are involved.

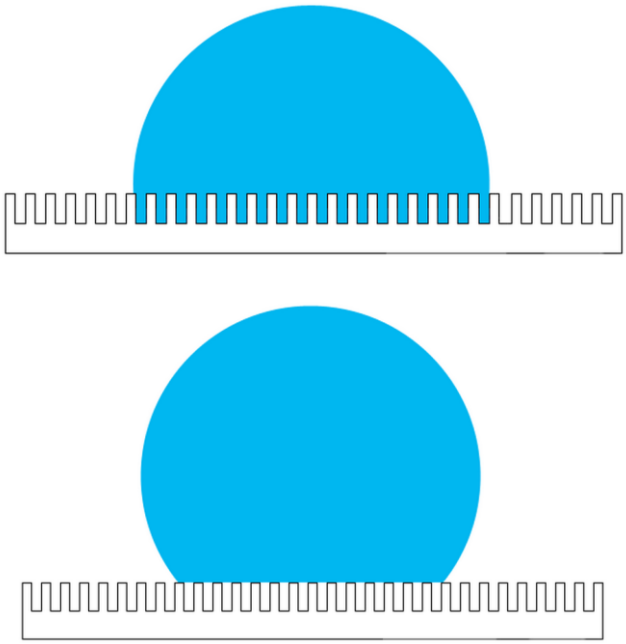

Figure. 2.6.1: Illumination of Wenzel (upper) and Cassie-Baxter (lower) state.

When water contacts with micro-structured surfaces, there exist two major types of states to represent the liquid-solid contact condition, which are Wenzel state and Cassie-Baxter states. (Figure. 2.6.1).

Cassie-Baxter state describes the apparent contact angle θ_{CB} for a liquid on a composite surface. [11] The states explains how simply roughing up a surface increases the apparent surface contact angle. Water contact with 2-component surface in this state can be described as:

$$cos\theta_{CB} = f_1 cos\theta_1 + f_2 cos\theta_2 \quad (2.3)$$

where θ_1 is original contact angle for component 1 with areal fraction f_1 and θ_2 is the original contact angle for component 2 with areal fraction f_2 present in 2-composite material. Special situation is when one component is air with a contact angle θ_2 of 180 °. With cosine (180 °) = –1, Equation 2.3 changes to:

$$cos\theta_{CB} = f_1(cos\theta_1 + 1) - 1 \quad (2.4)$$

where areal fraction f_1 and original contact angle θ_1 are for solid surface in this case. This implies that with a small f_1 and a large θ_1 it is possible to create surfaces with a very large contact angle.

A recent alternative criteria for the Cassie-Baxter state claims that the Cassie-Baxter state exists when the following two criteria are satisfied: 1) Contact line forces overcome body forces of unsupported droplet weight and 2) The microstructures are tall enough to prevent the liquid that bridges microstructures from touching the base of the microstructures. [13]

When the surface roughness is small meaning the aspect ratio of asperities is low, Wenzel state is more likely to be dominant. However, Cassie-Baxter state becomes dominant with surface roughness increasing. The contact angle of a water droplet on idealized sinusoidal surfaces was simulated by Johnson. The results show that when the roughness factor is greater than a certain level, the dominant state could transit from Wenzel to Cassie-Baxter [34]. In a practical hydrophobic surface with relatively medium level roughness, both states exist. An excellent water-repellent property on a super-hydrophobic surface is obtained by increasing the Cassie-Baxter state contribution, which means reducing the practical contact area between the solid and liquid droplets.

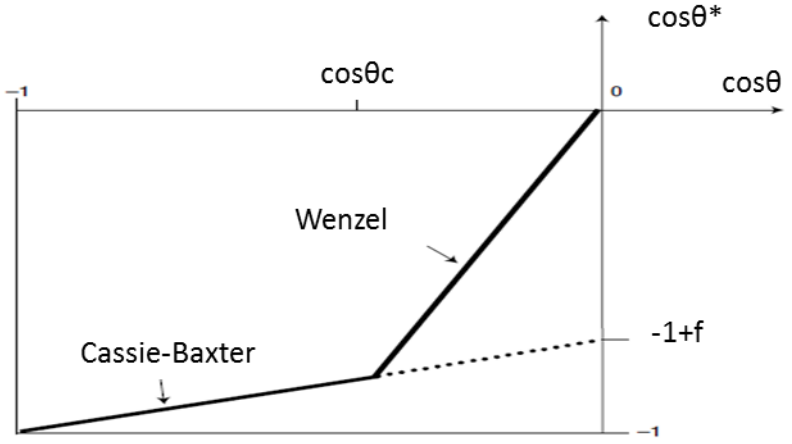

Figure. 2.6.2: Two states of super-hydrophobicity, threshold value is at contact angle of θ_C.

Equations 2.2 and 2.4 should therefore be successively obeyed as the contact angle increases, and the threshold value θc between the two regimes is given by equating the two equations [35]. This yields:

$$cos\theta_C = (f_1 - 1)(\mathrm{r} - f_1) \tag{2.5}$$

The value of cosθc is between –1 and 0. A comparison between the interfacial energies associated with the Wenzel and the Cassie-Baxter states confirms that air pockets should be formed only if original contact angle θ is larger than θc (Figure. 2.6.2). For 90° < θ < θc, the apparent contact angle θ* should be given by the Wenzel state (Equation 2.2). If θ is larger than θc, air remains trapped below the droplet, sitting on a composite surface made of solid and air, apparent contact angle θ* can be given by Equation 2.4. However it has often been reported that the Cassie-Baxter regime can also be observed for θ < θc, which is represented by a dotted line in Figure 2.6.2.

2.7 Wetting Transition Between Wenzel and Cassie-Baxter States

The relationship between water droplet size and surface geometric parameters governs the transition from composite solid–air–liquid interface (Cassie-Baxter state) to homogeneous solid-liquid interface (Wenzel state) on super-hydrophobic surfaces. [36]

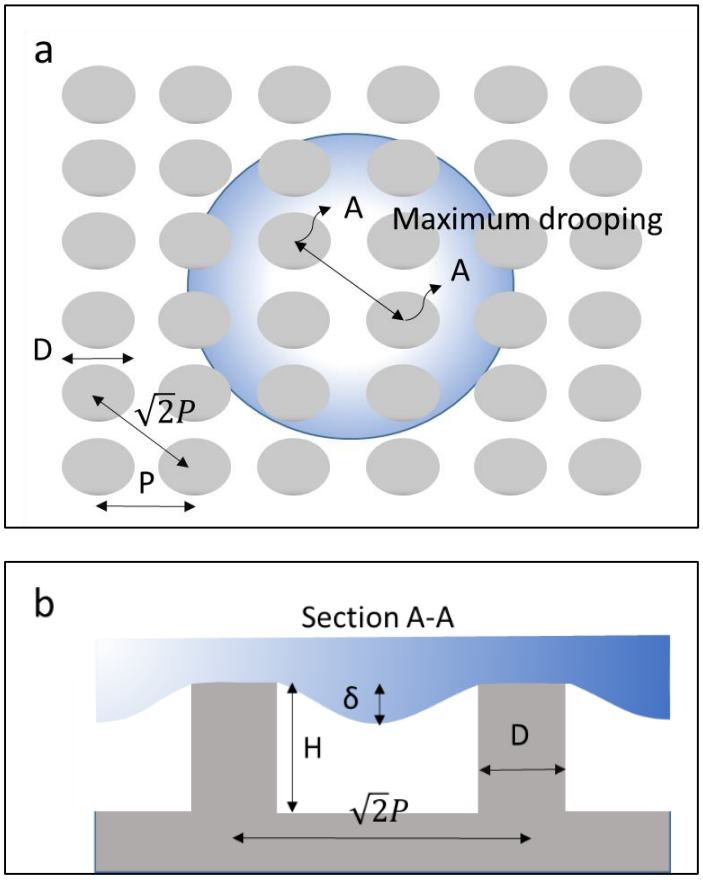

Figure. 2.7.1: A small water droplet suspended on a surface formed by a regular array of circular pillars. (a) Top view. (b) Side view of section A – A.

According to the observation of Jung and Bhushan as the water droplet suspended on super-hydrophobic surface made of solid and air as shown in Figure 2.7.1. The local deformation for small droplets is governed by surface effect rather than gravity. They reported that an equilibrium (or maximum) drooping depth of the droplet δ in the center of the square formed by four pillars can be defined as follows:

$$\delta = \frac{\left(\sqrt{2}P - D\right)^2}{8R} \tag{2.6}$$

where R, P, and D denote the droplet radius, the pitch of pillars, and the pillar diameter, respectively.

The drooping of water droplet maximized in the center of square formed by four pillars and drooping of droplet δ can be found in the middle of two pillars that cross diagonally. If the drooping depth δ is smaller than height H of the pillar, the Cassie-Baxter state exists because of the formation of the air pockets. If the droop (δ) is much greater than height (H) of the pillar (Equation 2.7),

$$\frac{\left(\sqrt{2}P-D\right)^2}{R} \geq \mathrm{H} \tag{2.7}$$

the droplet will just reach the bottom of the cavities between the pillars, resulting in the transition from the Cassie–Baxter state to the Wenzel state. Furthermore, in the case of large distances between the pillars, the liquid–air interface can easily be destabilized due to dynamic effects, such as gravitational or capillary forces. This leads to the formation of a homogeneous solid–liquid interface.

Chapter 3: Methods for Fabricating Super-hydrophobic Surface

Since the group at Kao [37] first demonstrated artificial super-hydrophobic surfaces in the mid-1990s, a very large number of clever ways to produce rough surfaces that exhibit super-hydrophobicity have been reported. Techniques being used to process material in order to make super-hydrophobic surfaces based on previous discussion can be simply divided into two categories [23]: 1). Making a rough surface from a low surface energy material, 2). Modifying a rough surface with a material of low surface energy.

3.1 Roughening a Low Surface Energy Material

Many techniques have been reported to rough the hydrophobic material to achieve super-hydrophobicity. These hydrophobic materials due to their extreme low surface energy can usually be roughened to exhibit super-hydrophobicity directly.

For example Xu et al. [38] fabricated a double-roughened perfluorooctanesulfonate (PFOS) doped conducting polypyrrole (PPy) film by a combination of electro-polymerization and chemical polymerization (Figure 3.1.1a).

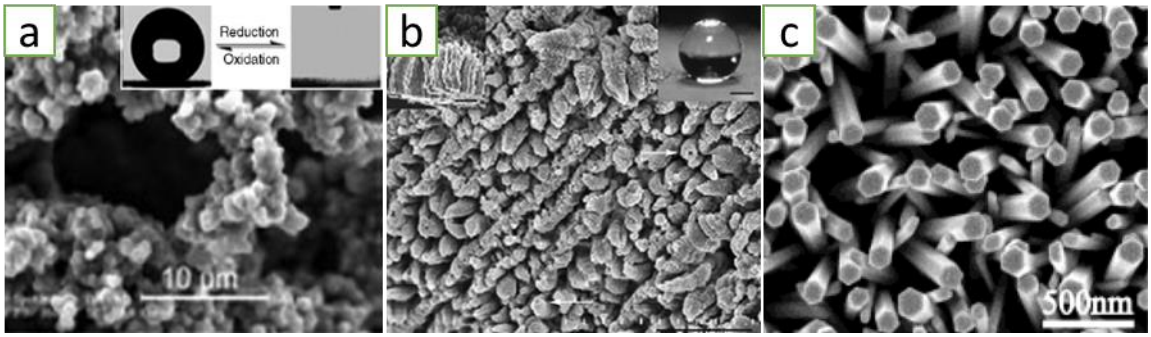

Figure. 3.1.1: SEM images of (a) The PPy porous film made by electro- and chemical polymerization and transition of hydrophobic states (inset) [38]; (b) Double-roughened poly (alkylpyrrole) film made by electrochemical polymerization [49]; (c) Reversible superhydrophobicity to super-hydrophilicity transition of aligned ZnO nanorod films [42].

Another well-known material with low surface energy is polydimethylsiloxane (PDMS)-one kind of silicones. Because of its intrinsic deformability and hydrophobic property, PDMS can be made into super-hydrophobic surfaces using various methods such CO2 pulsed laser [39] and nano-casting [40].

Although fluorocarbons and silicones are known as hydrophobic materials, super-hydrophobic surfaces were achieved using paraffinic hydrocarbons. Recently, several groups have demonstrated super-hydrophobic surfaces made from organic materials (Figure. 3.1.1b), such as polyethylene (PE) by controlling crystallization behavior [41]. Several inorganic materials have also been fabricated into super-hydrophobic surfaces, for example, ZnO [42] (Figure. 3.1.1c)

and TiO_2 nanorods [43]. Some researches have been carried out on improving the hydrophobicity of woven textiles and non-woven mats of electrospun fibres were found to be super-hydrophobic and can be produced with very small diameters [17, 18]. One of the interesting behaviors reported is that super-hydrophobicity can be transferred into hydrophilicity in some conditions and also can be reversibly switched back.

3.2 Roughening a Surface and Modifying with Low Energy Materials

By roughening low surface energy material, it is rather simple process (usually one-step), but limited in small set of materials. In order to overcome this limit, a totally new fabricating strategy is introduced by roughening a substrate surface and then modifying surface chemical properties with low energy materials. With this new strategy, the surface wettability is not just limited to the bulk properties of the material and the application of super-hydrophobic surface is greatly enlarged.

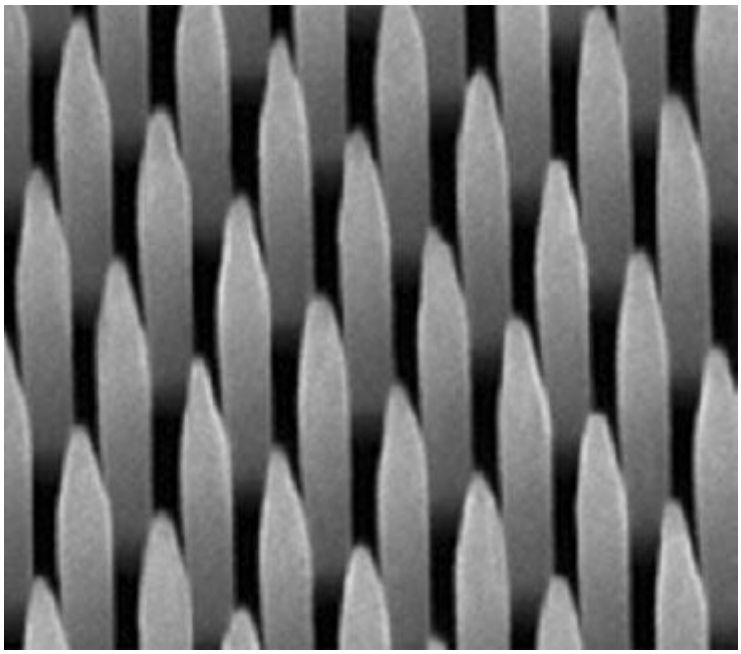

Figure. 3.2.1: SEM image of the nanopillars after hydrophobization the base diameter of the pillars is about 120 nm. [46]

There are many ways to make rough surfaces, including those mentioned above such as laser/plasma/chemical etching [44, 45], lithography [46] (which is well-established technique for fabricating lager area with periodic micro-/nanopatterns) (Figure. 3.2.1), sol–gel processing [47], different deposition methods (electrical/chemical reaction and chemical vapor deposition [48]) and laser processing [50].

On top of that, there are several methods commonly used to modify the chemical property of a surface. For example, covalent bonds can be formed between gold and alkylthiols.

Silanes are often used to decrease the surface energy. Other methods including physical binding, adsorption and coating can also change the surface chemistry.

3.3 Laser Processing on Metallic Surface for Super-hydrophobicity

Laser processing has been proved be an effective way to generate micro/nano structures on various metal surface. Due to the nature of the laser light, its unique characterization provides an exclusive noncontact material processing method to generate ultralow reflectance metal surfaces [53, 54, 55], sometimes even modification of the surface optical properties appearing different colors [56]. For super-hydrophobic surfaces fabrication, a lot of studies have been reported such as femtosecond pulsed laser structuring of aluminum surface [57], copper [22], and stainless steel [51, 58], picosecond pulsed laser-induced nanoscale super-hydrophobic structures formation on stainless steel and Ti alloys [50], nanosecond UV(355 nm wavelength) Nd:YAG laser ablation of metal substrates for super-hydrophobic effect [59].

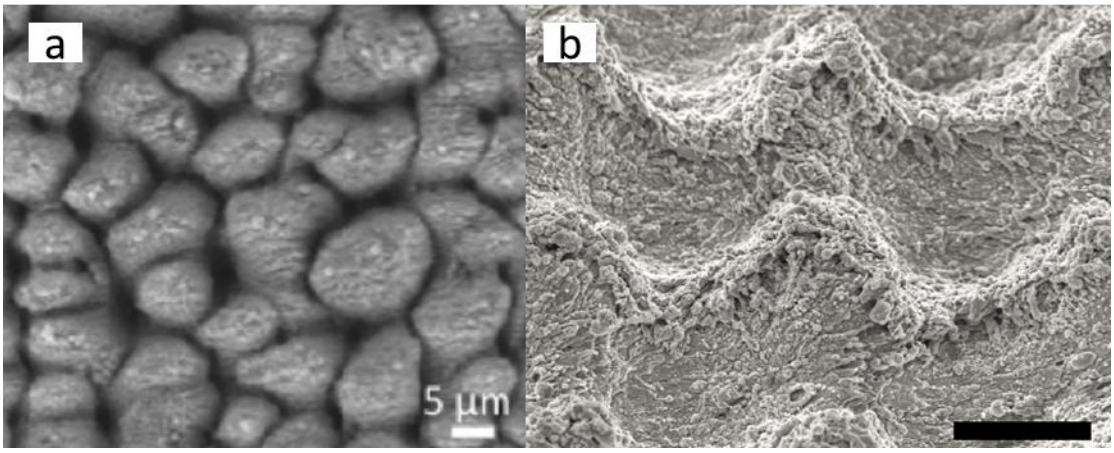

Figure. 3.3.1: SEM images of (a) femtosecond laser irradiated copper surface [22], (b) UV nanosecond laser texturing structure (Scale bar is 20µm) [59].

According to the well-established experiments and theories, pulsed laser, especially ultrafast pulsed laser will minimize the heat diffusion depth, thus increasing the processing precision and form smaller structures. The structures formed by femtosecond laser irradiation (Figure. 3.3.1a) are much smaller than those formed by irradiating of nanosecond laser (Figure. 3.3.1b). However, nanosecond lasers have the advantages of cost-effective, rapid process and stronger laser plasma interaction during laser pulses which is favorable for nano-particles re-deposition on top of the surface (Figure. 3.3.2).

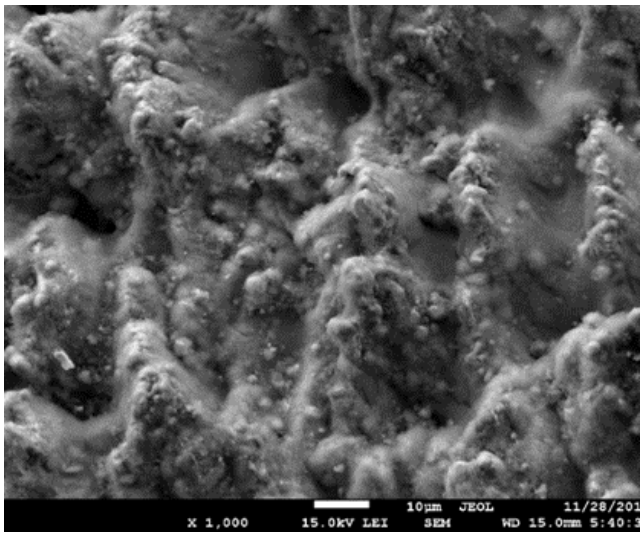

Figure. 3.3.2: SEM images of green nanosecond pulsed laser irradiated stainless steel surface (microstructures with nanostructures decorated on top).

3.4 Basic of Laser Material Processing

Among all the methods mentioned above, the laser patterning became a unique noncontact material processing method to fabricate controllable micro-scale structures to enhance the roughness of the surface. Laser texturing can typically fabricate regular micro-structures on alloy surfaces. It can be explained by the combination of the laser ablation and laser melting.

When material is irradiated with laser beam (Gaussian beam profile), laser-assisted material removal (laser ablation) help to remove center part of laser irradiated area and surrounding area is dominated by laser melting induced thermal capillary effect. After the laser beam is terminated, the molten pool will almost instantaneously solidify because of the high rate of heat dissipation to surroundings. An array of features can be generated by scanning a pulsed laser beam over the surface.

3.4.1 Introduction of Laser

A laser is a device that emits light through a process of optical amplification based on the stimulated emission of electromagnetic radiation. Lasers differ from other sources of light because they emit light coherently (spatial and temporal coherence) with excellent monochromaticity.

A laser consists of a gain medium which is a material with properties that allow it to amplify light by stimulated emission. For the gain medium to amplify light, it needs to be supplied with energy. This process is called pumping. The pumping sources also vary from light

pumping (diode-pumped laser) to electrical pumping (diode laser), chemical reaction (chemical lasers) and lamp pumping (lamp laser). Even the laser itself can be used as pumping source.

Depending on different gain medium being pumped, there are many different kinds of lasers such as gas laser (HeNe, CO2, Ar), solid-state laser, dye lasers and excimer lasers. The most widely used solid-state lasers including ruby, Nd:YVO4, Nd:YLF, Nd:YAG as gain medium generating fundamental wavelength of 1064 nm (near infrared). The laser wavelength can be frequency doubled, tripled and quadrupled to 532 nm green and 355 nm, 255 nm ultraviolet range. Ti:sapphire produces a highly tunable infrared laser, commonly used for spectroscopy also for mode-locked laser producing ultrashort pulses (Femtosecond pulses) with extremely high peak power. Excimer lasers such as ArF, KrCl, usually operate at ultraviolet wavelength with major applications such as semiconductor photolithograph and LASIK eyes surgery.

A laser can be classified as operating in either continuous or pulsed mode, depending on whether the power output is essentially continuous over time or its output consists of pulses of laser on different time scale such millisecond, nanosecond, picosecond and femtosecond. Some applications require the production of pulses with high peak power or energy, thus Q-switch and Mode-lock lasers are two typical methods used to generate pulses. The pulse energy then equals to the average power divided by repetition rate, and the peak power is the pulse energy divided by pulsed duration. As a result, if the laser power is the same, the lower the repetition rate the higher the pulse energy, and the shorter pulse duration the greater peak power.

In laser optics, the Gaussian laser beam profile is most widespread and convenient profile. A Gaussian beam profile means transverse electric field and laser intensity distributions are well approximated by Gaussian distribution.

The Gaussian beam with a fundamental transverse electromagnetic mode (TEM_{00} mode) will follow the mathematical expression:

$$I(r,t) = I_o \exp(-r^2/r_o^2)\exp(-t^2/t_o^2) \tag{3.1}$$

where I_o is the peak intensity, r_o and t_o are the spatial and temporal radius, at the 1/e intensity contour. r is the radial coordinate of distance to the center axis and t is the time variable. The spatial distribution of the energy fluence is then given by:

$$F(r) = \int_{-\infty}^{+\infty} I(r,t)\, dt = F_o \exp(-r^2/r_o^2) \tag{3.2}$$

where $F_o = \sqrt{\pi}\, t_o I_o$ is the peak fluence at the center of the laser beam with the unit of J/cm^2. Pulse energy E then can be write as:

$$E = \int_{-0}^{\omega} F(r) 2\pi r\, dr \tag{3.3}$$

For Gaussian beam propagation in the free space, the spot size ω(z) (radius) can be write in the following expression:

$$\omega(z) = \omega_o \sqrt{1 + (\frac{z}{z_R})^2} \tag{3.4}$$

where ω_o is known as beam waist which is the minimum value of beam spot size along the propagation axis. z is the distance from the beam waist and z_R is where the beam spot area double from the beam waist. z_R is related to the wavelength λ of the light, given by:

$$z_R = \pi\omega_O^2/\lambda_o \tag{3.5}$$

3.4.2 Laser-induced Melting and Ablation

The basic mechanism of laser structuring on top of solid surface is the combination of laser melting and ablations.

Laser ablation is the process of removing material from a solid surface by irradiating it with a laser beam. At relatively low laser flux, the material is heated by the absorbed laser energy and evaporates or sublimates. At high laser flux, the material is typically converted to a plasma. A small volume of material at the surface is evaporated if it is heated in a very short time (pulsed laser is necessary here because high pulse energy with enhance the laser ablation). The laser ablation techniques can be applied to many fields such as laser drilling/cutting, laser induced breakdown spectroscopy (LIBS) for chemical components analysis and laser coating removal.

As is shown in Figure 3.4.1, the Gaussian beam profile will have its peak flunece F_o at the central position. Laser ablation threshold is usually higher than the melting threshold with smaller diameters. The original beam spot size is the location of contour at 1/e of its peal fluence. Detailed experimental study of how to measure beam spot size will be presented in next chapter.

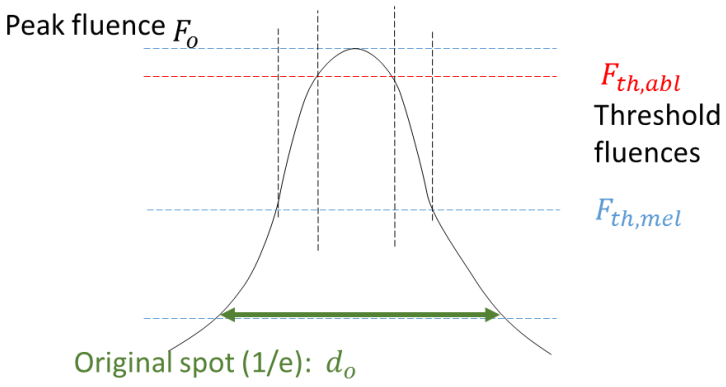

Figure. 3.4.1: Melting and ablation fluences level within single pulse of Gaussian beam.

In laser micro-structuring, direct laser ablation assisted by laser-induced thermal capillary effect on laser melting region helps to generate various periodic structures on the surface of solid. A high energy pulsed laser is used to rapidly melt small area of the surface, and the surface tension will cause the pool to deform [52]. After turning off the laser, the deformed melting material will cool and solidify (Figure. 3.4.2). Groenendijk and Meijer fabricated a microstructure on a stainless steel by ablating with a high repetition rate femtosecond pulsed laser [51].

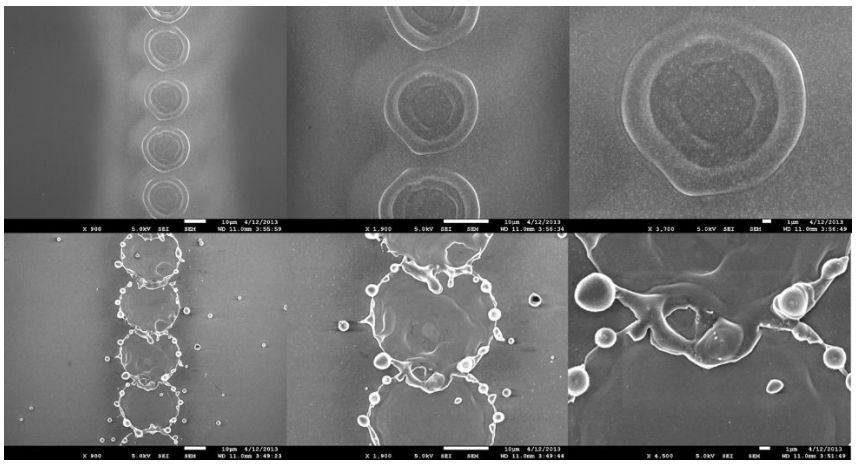

Figure. 3.4.2: SEM image of discrete pulses by 532nm nanosecond laser irradiation on single crystalline silicon surface at (a) 559 mW (b) 600 mW.

The laser-matter interaction mechanisms depend on a lot of factors such as the parameters of the laser beam, physical/chemical properties, surface condition of the material and the alignment and motion strategies. It was pointed out that the frequency and energy of pulses have a significant influence on laser surface texturing process. However, it is not scientific to ignore factors which in some cases become essential factors of the laser processing. To summarize, laser parameters include wavelength, intensity, spatial coherence, polarization and angle of incidence; for pulsed-laser irradiation, parameters include pulse duration, laser fluence and repetition rate; for alignment and motion strategies, parameters include focal spot size, focal position and pulses overlapping. The material is characterized by its chemical composition and arrangement of atoms or molecules, which determines the type of elementary excitation and their interactions with laser light. These material characteristics such refraction index, thermal diffusivity (which is combined factor of material density, conductivity and specific heat capacity) will have different effect on the penetration (absorption) depth when irradiated by laser light. (See Equation 3.6)

$$\delta_p = 1/\alpha \tag{3.6}$$

Where α is the absorption coefficient. The penetration or absorption depth is thus depend on the wavelength of the laser light since α is differ for light of different wavelength even for the

same material. For example, shorter wavelength light has smaller absorption depth on silicon, so the absorbed energy will be kept on shallower surface of the samples.

After the penetration or absorption, the other important depth to be consider is the diffusion depth which is related to the duration the laser irradiation (pulse duration or pulse width if for pulsed laser) and the diffusivity of the materials. For ultra-short laser pulses such as femtosecond laser, the pulse duration is femtosecond order. Usually the heat diffusion depth can be neglected which gives ultra-short pulsed laser very limited thermal effect. However, because of the ultra-short laser's natural complexity and high cost, femtosecond or picosecond lasers are restraint in the scientific or rigid study where there is strict requirement of minimized diffusion depth. Thus, the most widely used pulsed lasers in industries are nanosecond pulsed lasers. Thermal diffusion depth can be calculated by solving the heat conduction equation with constant heat flux boundary condition following the error function. The diffusion length d ~ $\sqrt{\alpha t_p}$, where α is material diffusivity and t_p is the pulse duration.

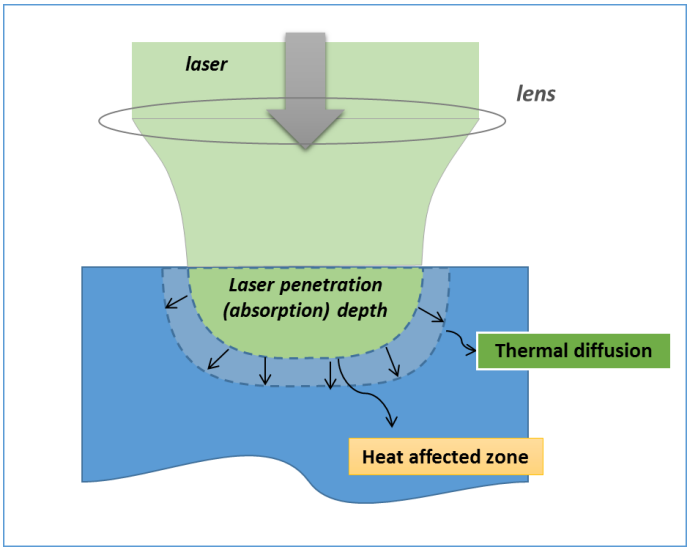

Figure. 3.4.3: Illumination of laser heating mechanism. Heat affected zone is the combination of absorption depth and thermal diffusion depth.

The penetration depth together with the thermal diffusion depth can be termed as heat affected zone (HAZ) which is basic concept and definition to understand laser heating mechanism. (Figure. 3.4.3) For example, if HAZ is small which means the volume of the material being affected by the laser is limited which will result in a very high temperature of the material volume. Depend on how much energy input of the laser light, the temperature be calculated. This will explain why people need very high pulse energy laser to assist laser ablation (Such as in LIBS, plasma signal is amplified by enhanced laser ablation). Since the temperature of melting, vaporization or sublimates are known for majority materials, the link can be built as the Equation 3.7, from the temperature increase to pulse energy or, at the most cases, laser fluence (J/cm^2):

$$(1\text{-R})\ F_{avg}\pi d_o^2/4 = \rho C_P V \Delta T \tag{3.7}$$

where R is the reflectance of the surface, d_o is the diameter of the laser post size, F_{avg} is the average laser fluence, C_P is specific heat capacity, ρ and V are the mass density of material and volume of the heat affected zone, respectively. Then the temperature increase ΔT can estimated by this equation. If the temperature increased to such a value higher than the melting temperature, the laser will induce the material melting. If the laser fluence further increases, the temperature after laser irradiation will be much higher and material vaporization or sublimation will occur (laser ablation). In laser micro-structuring, direct laser ablation assisted by laser melting induced thermo-capillary effect help to generate various periodic structures on the surface of solid (Figure. 3.4.4 and Figure. 3.4.5). Surface tension driven by the temperature gradient will cause the molten pool to reflow and solidify after cooling down.

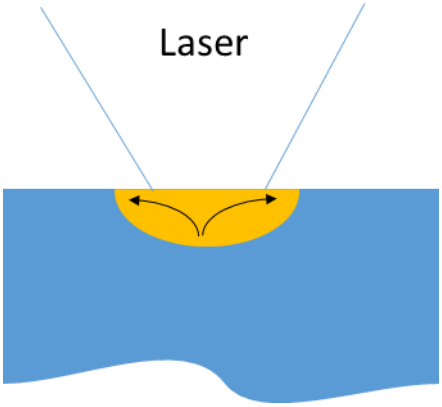

Figure. 3.4.4: Illumination of laser melting induced molten pool reflow driven by surface tension.

When heat treatment of surface with laser fluence is below the melting threshold, the laser beam can be considered as a heat source which induces a temperature gradient at the material surface (Figure. 3.4.3). Then after the laser fluence is over the melting threshold, molten pool will be formed since the temperature exceeding the melting temperature of the solid. This molten pool will deform because of surface tension driven by temperature gradient and solidify after laser irradiation and cooling down (Figure. 3.4.4). When the laser fluence reaches a certain level (ablation threshold) which will cause significant material vaporization and sublimation (Figure. 3.4.5).

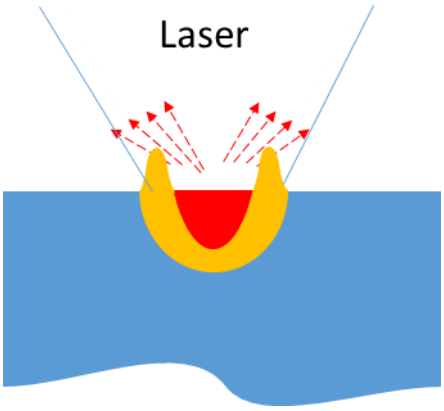

Figure. 3.4.5: Illumination of laser ablation and laser melting induced thermo-capillary effect when laser fluence over the ablation threshold

Laser beam profile is usually Gaussian beam (laser used in this work is Gaussian beam). Ablation happens around the center of laser irradiated area with higher temperature. Melting happens on the surrounding areas with the relatively lower temperature. A vapor plume can be formed above the substrate surface. With further increasing laser fluence, the number of species within the plume increases and interactions between the laser beam and the ablated material become important. Subsequently, laser ablation will always result in the ionization of species. Above a certain laser fluence, the vapor plume is more appropriately considered as plasma. Because of the strong nonlinearity in this interaction, small changes in laser parameters may cause big changes in processing results as reported by Savastenko et al 2000 [60]. For this reason, precise control of the various processing parameters is important for repeatable experimental results.

Nano-particles are generated of the laser ablation where laser light have strong interaction with the laser-induced plasma. This will cause the nano-particles re-depositing onto the surface after the laser ablation, resulting in changing the surface morphology and chemical composition. Oxygen, water vapor or other gases and contaminants in the ambient air interact with the nano-particles at a high temperature [18].

Chapter 4: Experiments

4.1 Laser Specifications

The laser employed here to generate microstructures on metal surface is Nd:YAG DPSS (Diode-Pump Solid-State) nanosecond Q-Switch laser (F2W-30 green and FW-200 IR) from Yuco Optics Corporation. Green laser with 532 nm wavelength is optimized at 10 kHz pulse repetition rate with maximum average power of 3.15W. The corresponding pulse width is 16ns. Laser test report is listed at Table 4.1.

Table. 4.1: Test Report of the F2W-30 DPSS green nanosecond laser at current setting at 29A. IS means setting current, DT means Diode Temperature and LT means Laser Heat Temperature. (The data was provided by the Yuco Optics.)

Repetition Rate (kHz)	Average Power (W)	Pulse Width (ns)
3	0.88 (@I=24.5)	12
4	1.38 (@I=24.5)	12
5	2.53	13
6	2.81	13
7	2.87	14
8	2.88	14
9	2.86	15
10	2.96	16
11	3.05	17
12	3.10	18
Optimized at 10kHz, IS=29.5A, DT=28 ℃, LT=28 ℃	3.15	16

Initially, laser with gain medium Nd:YAG emits the fundamental wavelength of 1064 nm infrared light (IR). Then the wavelength can be modified by second harmonic crystal to generate green light of 532 nm wavelength (Figure. 4.1.1).

The laser is pumped by 808 nm laser diode, humidity of the laser cavity is reduced by desiccants and the temperatures of diode and laser head is controlled by controller with air-cool system. The front and back of the control box is shown in Figure 4.1.2, from where repetition rate, diode current, as well as monitor diode and laser cavity temperatures which are the key factors responsible for a good quality and stability of the laser output can be monitored and adjusted.

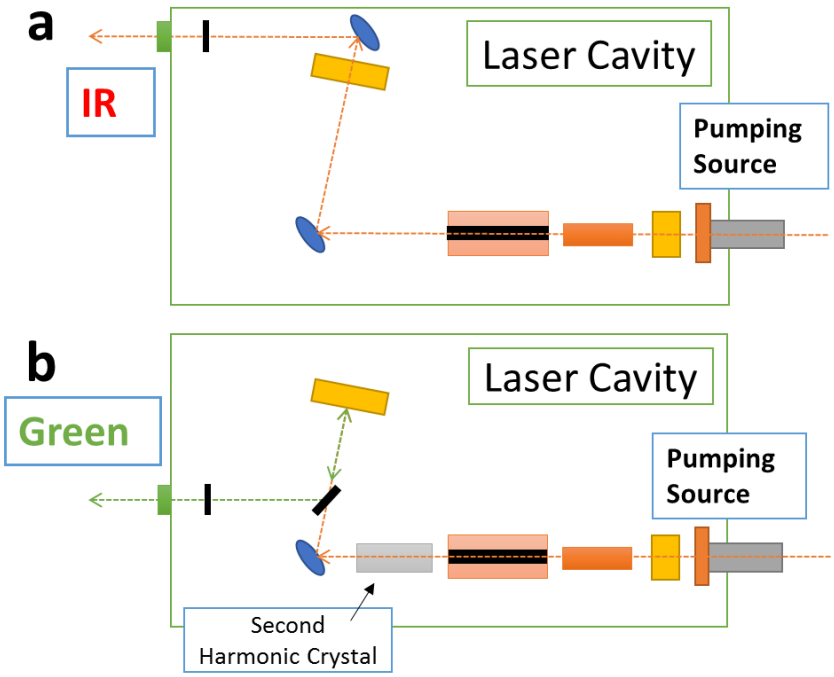

Figure. 4.1.1: Simplified schematic drawing of laser cavity emitting (a) 1064nm wavelength light (b) 532nm wavelength light with second harmonic crystal.

Figure. 4.1.2: Photograph of the laser controller front (upper) and back interface (lower).

4.2 Experiment Set Up (I): Laser Material Processing System

The laser material processing system is presented in Figure 4.2.1. Laser beam is directed by specific reflecting mirrors for certain wavelength laser light. Since the laser is linear polarized instead of circular or elliptical, the laser power was adjusted by adding two external optics: half-wave plate (Polarizer) and polarizing beam splitter (PBS). The half-wave plate mounted to rotational holder allows the plate to rotate 360 °which enable the half-wave plate to change the original polarized laser light to arbitrary linear polarizing direction. The PBS works as beam separator which can reflect horizontal portion of polarized electromagnetic (light) while pass the vertical portion or vice versa. Since the laser beam polarization is initially modified when rotating the half-wave plate, the horizontal and vertical portion of the light change correspondingly. By put the two optics together, it is convenient and feasible to control the laser power without touching the current of the pumping diode which ensures the quality and stability of laser beam.

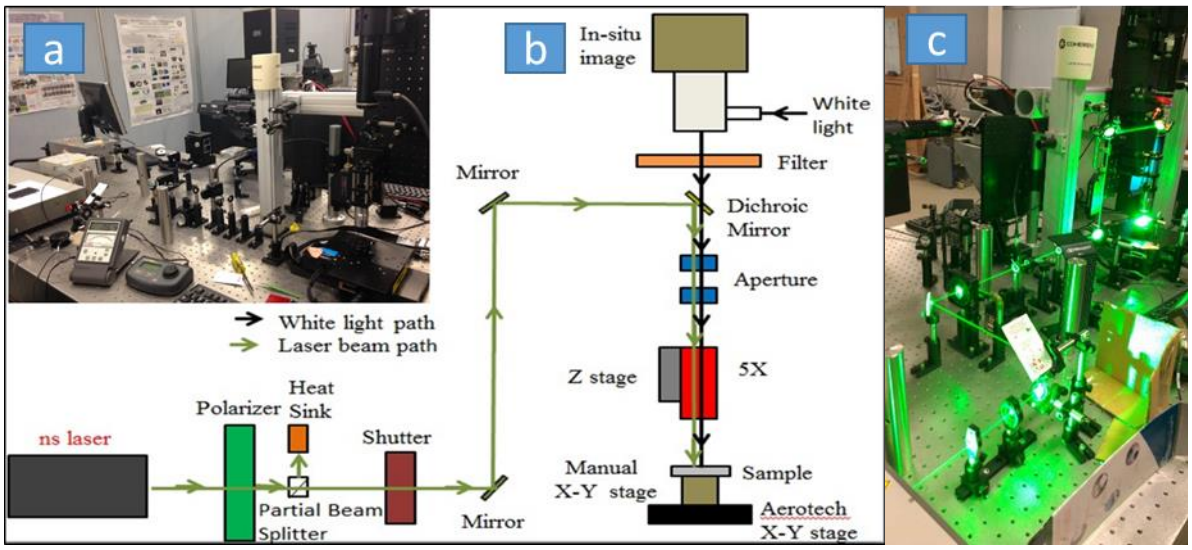

Figure. 4.2.1: (a) Photograph of the laser material processing system without laser turning on and (c) with laser operating. (b)Schematic drawing of the system.

Mechanical shutter was also used here linked with motion stage controller to control the laser irradiation on the sample surface. Mitutoyo M-plan lens of 5x magnification (NA=0.14, f=200) was used for focusing the laser beam. Lens attached to Z-axis Newport motion stage (ESP 301 motion controller) was to adjust laser focal position. Sample specimen was placed on the X-Y linear translation stage from Aerotech (Nominal resolution of 10 nm). The Aerotech stage is controlled by A3200 control software installed in PC with convenient GUI (Graphic User Interface) (Figure. 4.2.2) and programming language (based on G-code or M-code with of AeroBasic modifications). Sample was first put on to a small stage with tilting adjustment, then placed on the Aerotech stage, in order balance the sample as flat as possible and make sample surface perpendicular to the vertical laser beam. Making the sample surface flat is important

when moving the sample based on raster scan manner. Unbalanced sample surface will results in laser focal position variation along the scanning direction, leading to non-uniform results.

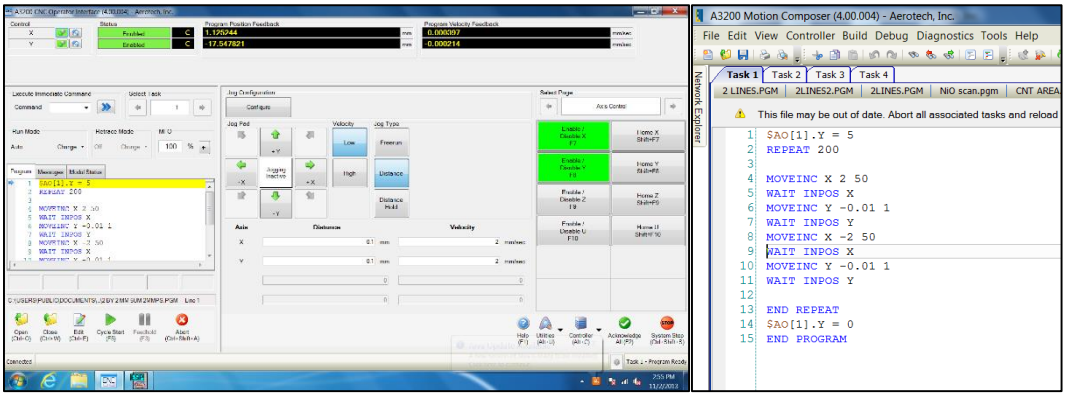

Figure. 4.2.2: Screenshot of Aerotech A3200 motion control software (a) Graphic User Interface (b) Example of programming language for raster scan.

In order to in-situ monitor the laser-matter interactions as well as precisely adjust focal position of the laser, AmScope MU500 CCD camera was coupled with microscope tube of 12x magnification on the top of the laser irradiated area. Dichroic mirror with back side polished was used here to allow the illumination white light pass through and reflect 532 nm wavelength green laser light.

And making the laser beam perpendicular to the sample surface is very important in this case. People already studied the influence of different laser incident angles, but in this case, the laser beam was fixed vertical to the surface in order to ensure results can be reproduced. By introducing the three mirrors with 2-D adjusting mirror mounts, it provided more flexibility to align the laser beam. This set up also included two mechanical apertures (Iris) for guiding purpose. By locating the laser beam at the center of the two apertures and sample surface, the laser beam was fixed in a line by 3-points: two irises and one laser-matter interaction spot.

4.3 Experiment Set Up (II): Contact Angle Measurement Platform

The contact angle measurement platform was assembled with several basic components (Figure. 4.3.1): a) CCD camera with focusing lens system for image and video capture; b) Back white light source for illumination; c) One PC connected to digital camera for real time monitoring, capturing image and storing data; d) Adjustable sample stage; e) Syringe pipet with scalable volume control to apply water; f) one-axis motion stage working as syringe pump to control the water volume; g) Motorized Z-axis stage to adjust the position of the syringe.

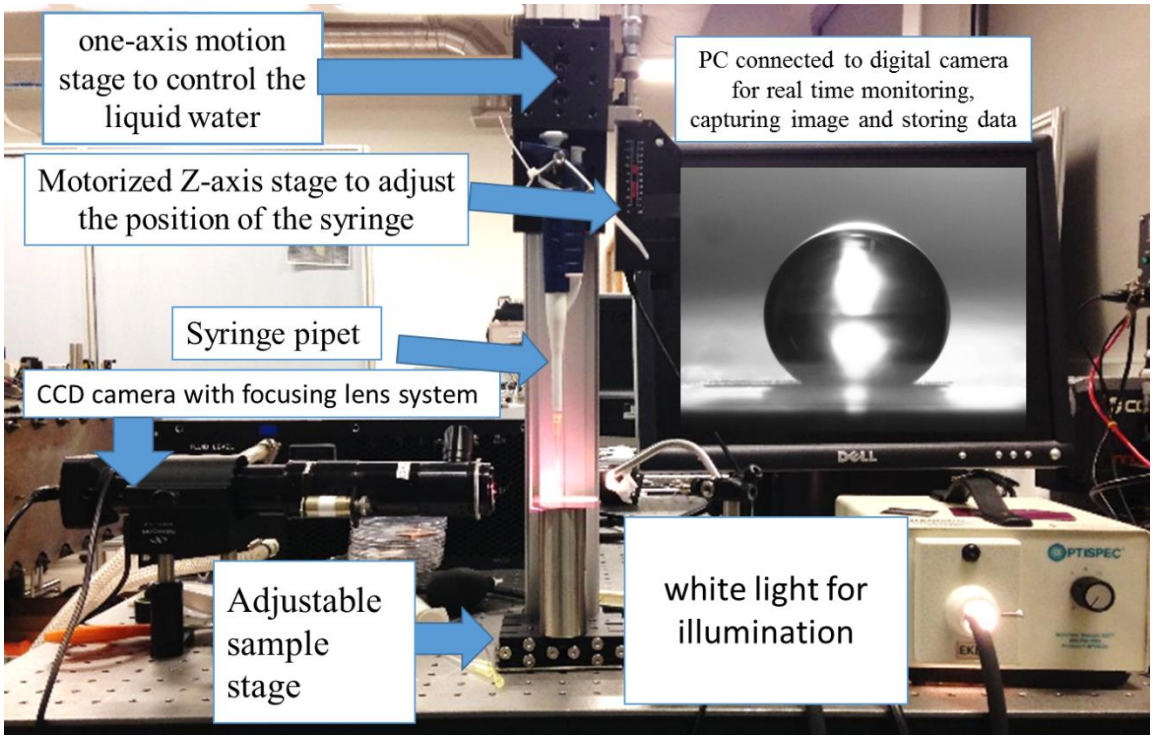

Figure. 4.3.1: Homemade contact angle measurement platform.

Static contact angle measurement as well as contact angle hysteresis were measured by adjusting the size of the water droplets. Distilled water was used here to decrease the influence from contamination or impurity from the liquid. By replacing the sample stage with hot plat or thermal electrical cooler (TEC), more experiments for example Leidenfrost effect and anti-freezing performance can be conducted with this platform.

4.4 Characterization Tools

4.4.1 SEM and EDS

To study the morphology of small scale structures, scanning electron microscope (SEM) located in Center of Functional Nanomaterials in Brookhaven Nation Laboratory was used in this work.

A scanning electron microscope is a type of electron microscope that generates images of a sample specimen by scanning with a focused electron beam. The electron beam is generally scanned based on a raster scan pattern, and the combination the beam's position and detected signals form basic information of the image. SEM can achieve resolution better than 1 nanometer and in most case require vacuum condition.

The electrons interact with atoms in the sample, producing secondary electrons and X-ray signals that can be detected and that contain information about the sample's surface topography (SEM) and chemical composition. The method using the X-ray generated from the interaction

between the electrons and atoms to reveal the chemical composition is call Energy Dispersive X-ray Spectroscopy (EDS).

Figure. 4.4.1: Photography of (a) Dual beam SEM/FIB Hellius Nanolab (b) vacuum chamber and sample stage with holder (c) Joy-stick operation interface.

Helious Nanolab Dual Beam SEM/EDS/FIB located in clean room (Figure. 4.4.1a) and Analytical SEM JEOL 7600F have been used in this study. Vacuum condition is required for both machine. In Figure. 4.4.1b, a photograph of open vacuum chamber of JEOL 7600F I s presented. Sample specimen can be fixed to top of the sample holder and then relocated into the center of the vacuum chamber. Typical 20minutes waiting period for vacuum pumping procedure is expected. Metal and semiconductor such as silicon can be easily fixed by conducting tape and mechanical tips. Other sample with low electrical conductivity should be coated with a few nanometer of gold film to enhance the conductivity of the sample surface. The reason using conducting tape or metal tips to fix the sample is for guiding the electrons from the conduction sample to sample holder in order to reduce charging effect which is one of the major influence factors of the image quality. A photography of joy-stick image improving panel is shown in Figure 4.4.1c.

4.4.2 Other Tools

In this works, some other tools have used to assist the analysis of the laser treated samples. For example, the optical microscope with Mitutoyo lens of 5x, 10x, 20x and 100x has been used to have first quick observations. By change the position of illumination white light source, transmission optical images and dark field images can be taken by supplying the white light from the back the sample and side, respectively. The latter, dark field images, can be used as a method to reveal the roughness information of a surface, since the illumination light is applied from one side, roughness signal can be enhanced by the shadow of the high aspect ratio structures.

Secondary Ion Mass Spectroscopy (SIMS) has been used as a technique to analyze chemical composition of solid, providing the profile of the concentration distribution of targeting

chemical element along the depth. The SIMS test of laser doping of phosphorus into a P-type Boron doped single crystalline silicon wafer to form P-N junction for the application of solar photovoltaic is performer by Analytical Instrumentation Facility in North Carolina State University.

Other tools such as Raman spectroscopy and IR camera have also been used. The former was to confirm crystallinity of single crystal silicon after disruption of laser light during laser texturing while the latter was used to capture the emissivity of textured silicon and metal surface for the purpose of heat transfer enhancement.

Chapter 5: Results and Discussion

Gaussian laser beam spot size measurement [61] is presented with a simple technique irradiating pulsed laser on the single crystal silicon surface. This technique has been used for measuring of the laser melting and ablation fluence and laser focal spot size. Different focal position as well as laser beam spot size will affect laser ablation shape and morphology [62]. And both 1064 nm IR and 532 nm Green nanosecond laser have been used to generate surface microstructure to understand basic morphology after laser ablation and their effect on surface wettability. Surface wettability on copper and stainless steel surfaces were being investigated by measuring contact angle of the surfaces. Right after laser processing, surfaces were super-hydrophilic with contact angle less than 5 °. Super-hydrophobicity were achieved after laser processing and place in the air environment for certain period. Leidenfrost effect was also studied. Surface morphology can be analyzed by Scanning Electron Microscopy (SEM) whose results show hierarchical structures obtained by irradiating to laser pulses. Surface chemical components analysis was performed by Energy Dispersive X-ray Spectroscopy (EDS) to further tracking the super-hydrophobicity formation mechanisms.

5.1 Laser Beam Spot Size Measurement

In order to measure different focal spot under various focal condition and calculating the laser melting and ablating threshold, 10 kHz 532nm wavelength green pulsed laser with Gaussian beam profile was couple on the single crystal silicon to perform the test. If the laser is scanned at relative slower speed, the pulses will overlap and the single pulse cannot be separated. To minimizing the overlap and reveal the single pulse irradiated area, sample was moved at the speed of 250mm/s. Since the laser is 10 kHz, each single pulse separated roughly around 25μm from next pulse (Figure. 5.1.1).

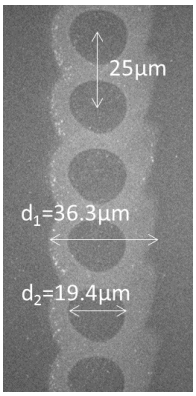

Figure. 5.1.1: SEM images of discrete laser pulses at the scanning speed of 250mm/s at the power level of 530mW using single positive lens (f=150). The oxidation ring occurs when temperature at the surrounding area of the pulse is lower than melting temperature because of heat dissipation.

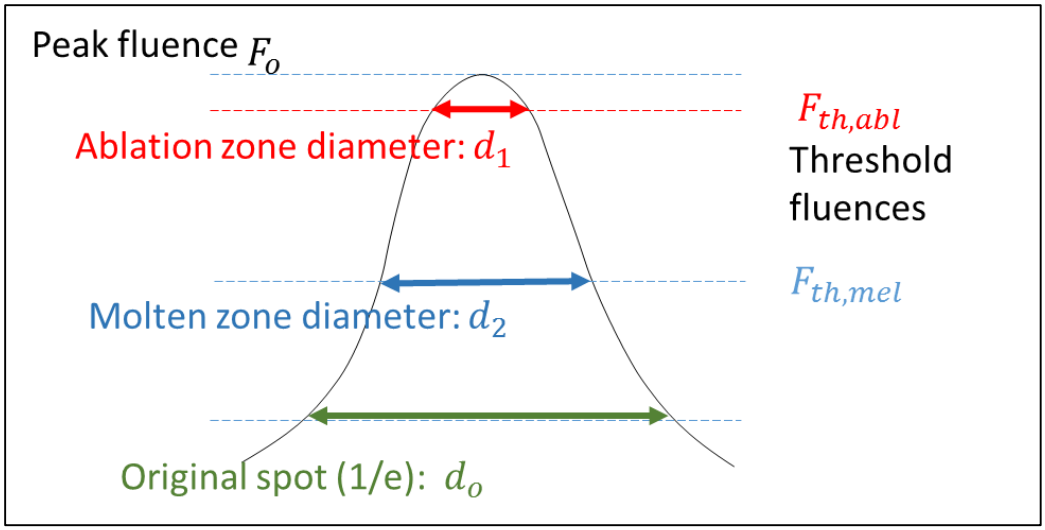

Figure. 5.1.2: Relation showing melting and ablation fluences level with single pulse of Gaussian beam.

For Gaussian beam profile Equation 3.2 about F (laser fluence). Figure 5.1.2 provides the fluence distribution with one Gaussian pulse. Since the laser fluence is pulse energy divided by area, the Equation 3.2 will change into pulse energy relation.

$$E = E_o \exp(-d^2/d_o^2) \tag{5.1}$$

Table 5.1 shows the diameter of the laser melting spot size change with power level. Based the equation provided above, the square of measurement diameter with respect of Ln E can be plotted. Then based on the plot line by curve fitting, information of original beam spot size d_o and melting or ablation fluence ($F_{th,mel}$ and $F_{th.abl}$) can be estimated.

Table. 5.1: Diameters of the laser spot size change with laser power.

Power(W)	Pulse Energy: E (uJ)	Ablation Zone width: d_1 (um)	Melting Zone Width: d_2 (um)	d_1^2	d_2^2	LnE
378	37.8		8.57		73.47	3.63
389	38.9		16.67		277.78	3.66
400	40		20		400	3.68
410	41		21.90		479.81	3.71
421	42.1		25.23		636.96	3.74
429	42.9		25.71		661.22	3.75
440	44.0		27.14		736.73	3.78
449	44.9		27.61		762.81	3.80
460	46	8.13	28.57	66.01	816.32	3.82
471	47.1	11.25	30.47	126.56	928.79	3.85
481	48.1	13.75	30.47	189.06	928.79	3.87
489	48.9	15	30.95	225	958.05	3.88
499	49.9	15.63	30.95	244.14	958.05	3.91
511	51.1	16.88	31.42	284.76	987.75	3.93
520	52	18.75	32.38	351.56	1048.52	3.95
530	53	19.38	32.38	375.39	1048.52	3.97
540	54	20	33.33	400	1111.11	3.98
550	55	20.63		425.39		4.00
559	55.9	21.88		478.51		4.02
571	57.1	23.75		564.06		4.04
582	58.2	25		625		4.06
590	59	28.13		791.01		4.07

From the Figure. 5.1.3, by curve fitting. Two straight lines can be obtained:

$$y = 2480.2\,x - 9440.8 \tag{5.2}$$

$$y = 2577.8\,x - 9099.7 \tag{5.3}$$

which can be rewrote as

$$d = d_{1o}\sqrt{\ln(E/E_{1O})} = 49.8\sqrt{\ln(E/45)} \tag{5.4}$$

$$d = d_{2o}\sqrt{\ln(E/E_{2O})} = 50.8\sqrt{\ln(E/34)} \tag{5.5}$$

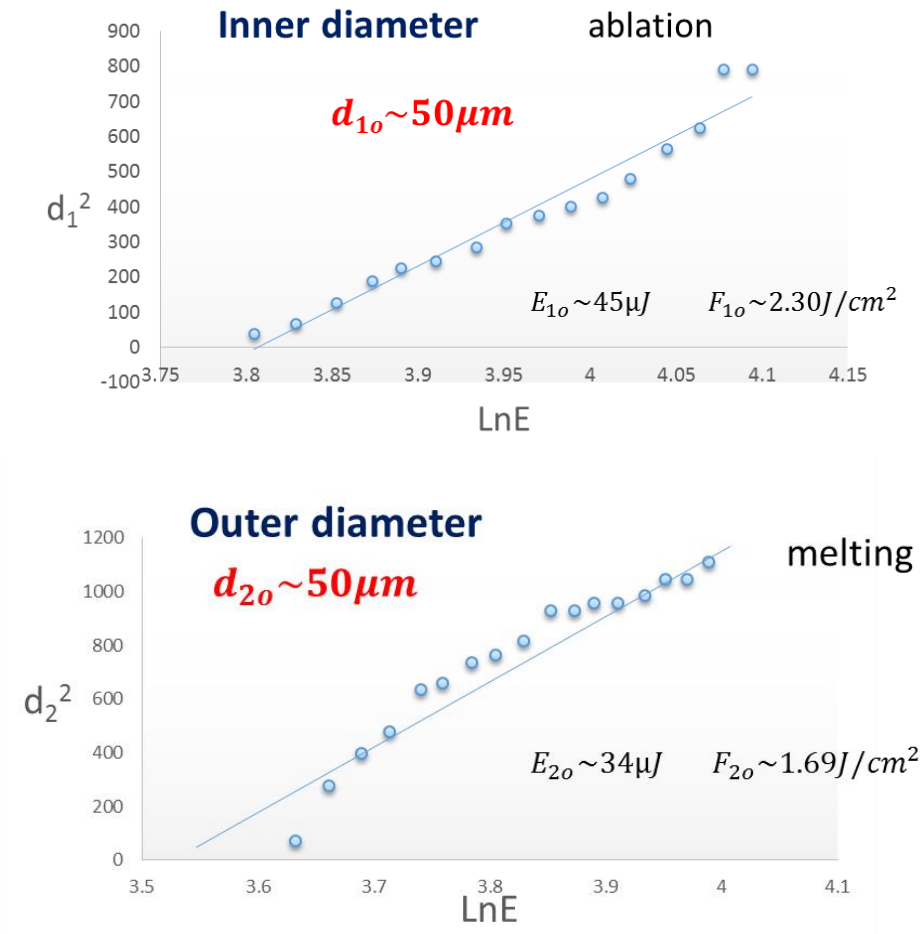

Figure. 5.1.3: d^2 changing with respect of LnE. (d_1 and d_2 is measured melting spot size and ablation diameter respectively, E is pulse energy).

For silicon which is the sample used in this study, the calculated original laser focus spots size $d_{1o} \cong d_{2o} \cong d_o$ is around 50μm, melting threshold is ~ 34μJ (pulse energy) and ~1.7J/cm^2 (laser fluence), ablation threshold is ~ 45μJ (pulse energy) and ~ 2.3J/cm^2 (laser fluence) respectively.

5.2 Laser Focal Position Effect

In actual experiment, Mitotuyo M plan 5x lens with long working distance instead of single positive lens was used here. To enhance the laser ablation of metal, focusing the laser inside the metal surface will help reduce the effect so called plasma shield. But simply putting the laser focus inside the sample may cause the change the of the laser spot size because the nature of Gaussian beam. Laser beam spot size tent to be bigger when it is more away from the laser focal position ($w>w_o$). This effect is showed in Figure 5.2.1.

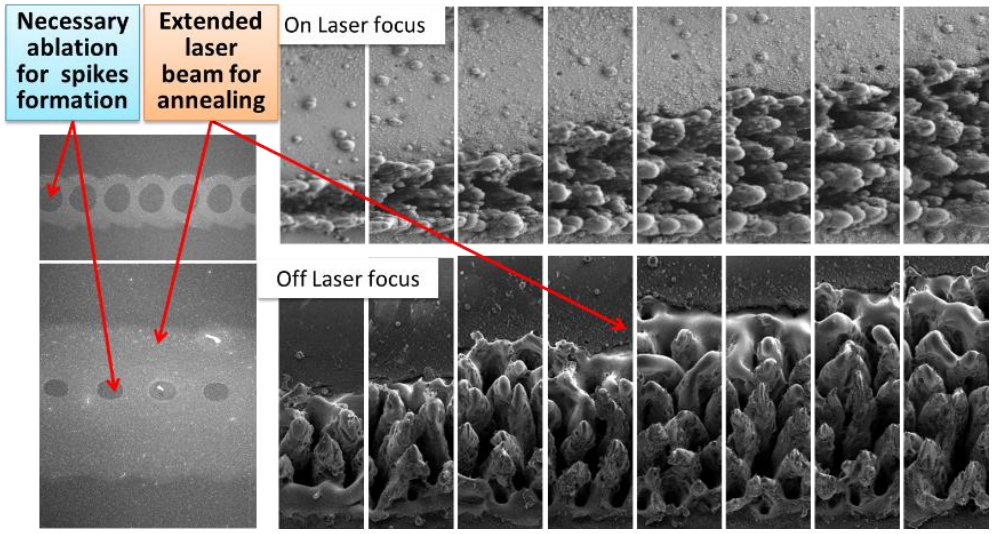

Figure. 5.2.1: SEM images of study on laser focal position effect on simultaneous annealing. Upper images are focusing laser with f=150mm single position lens, laser focus on sample surface. Lower images are focusing laser with Mitutoyo 5x lens, laser position is inside the sample surface 0.7mm.

For the result in Figure 5.2.1, 10 kHz green nanosecond laser was used. Left two images were created by scanning the laser at speed of 250mm/s to show the discrete dots of single laser pulse. Laser beam sizes differ for two cases based on the melting on the surrounding area of laser pulses. On the right, two set of data about different number of scans (one to eight from left to right) are provided. On upper level, the laser power was kept at 600mw and laser was scanned at the speed of 8mm/s with vertical shift of 8μm per scan (Figure. 5.2.2). Laser focus is on top of the sample surface. On the lower level, although the beam spot size is big, center laser fluence is still high enough to ablate the material once the laser power stays as high as 2.5W. At this power level, laser was scanned at speed of 10mm/s and 10μm vertical shift per scan and laser's focal position was inside the sample of 0.7mm.

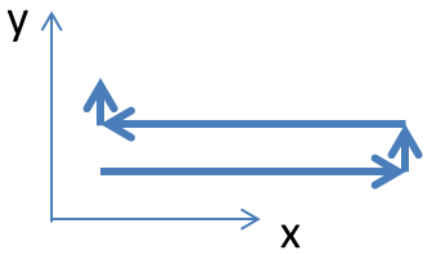

Figure. 5.2.2: Raster scanning direction: Laser scan along x direction and vertical shift long y direction.

By expending the laser beam simultaneous secondary annealing was achieved to reheat the solidified laser microstructures to have better crystallinity which is favorable for efficient light-current conversion in photovoltaic application at the same time enhancing total amount of

light absorbed by light trapping mechanism. Similar results can be found by using the same laser and f=50mm lens and placing the laser focus inside the sample surface (Figure. 5.2.3)

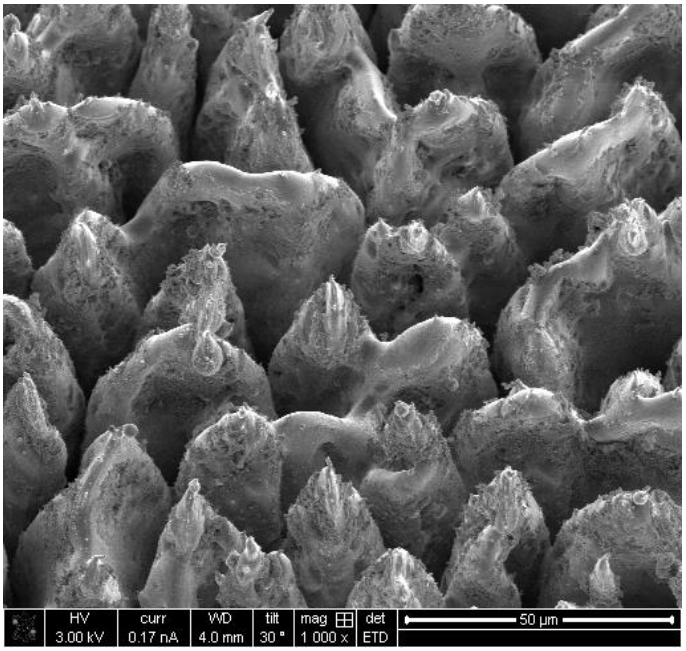

Figure. 5.2.3: SEM of simultaneous secondary annealing results at laser power of 1.6W.

For metal, laser focal position effect is different by the natural difference on laser heating mechanism of metal and semiconductor. In metal, there is no band gap to be overcame since the electrons of metal are already on the "conduction band" (The difference of valence band and conduction band is called band gap). It is very difficult for the photons from the light to penetrate most of the light is reflected which is the reason that most metals are not transparent and can be used to make mirrors. The "penetration depth" of the metal is called skin depth which refers to the decay of electrical current. For the same metal, skin depth could be different when the metal is interacting with lights of different wavelengths, thus different photon energy. However, big power of laser can be used (the amount of photons is bigger) to damage the metal and usually plasma can be formed. Laser plasma is formed around certain distance of surface (a few hundred micrometers) during laser ablation. If the laser focal position is on the surface or sometime outside the laser focus, the plasma formation will form so called "plasma shield" which will compromise further laser interaction of the material being processed. Instead, laser will have more interaction of the plasma resulting in the re-deposition of ablated materials (nano-particles). Thus placing laser focus inside the surface can enhance the laser ablation by reduce the contact between plasma and laser light..

5.3 Laser Power and Wavelength Effect

As it was mention above, different wavelength of laser light will penetration different depth. In order to study this effect, two different nanosecond lasers, 532 nm green and 355 nm

UV were used to demonstrate. Beside the difference in laser affected depth, there are also differences in the morphology of the laser micro-structures.

In order to have a better understanding the laser affected region, sample first was scanned by laser light, then broken along the cross section A-A. SEM images were taken on the cross sections. (Scanning direction and cross sectioning direction shown in Figure. 5.3.1).

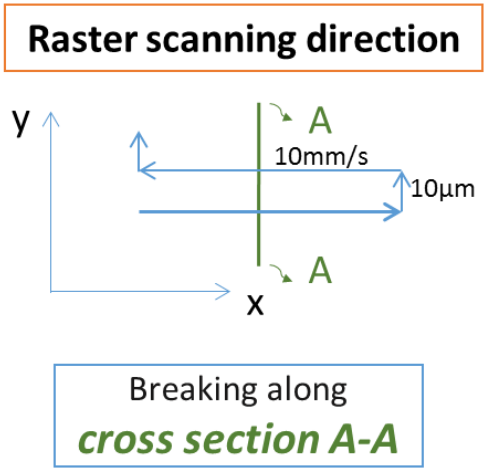

Figure. 5.3.1: Illumination of laser scanning direction and cross section direction.

First, power variation study of 532nm nanosecond laser was performed as shown in the Figure 5.3.2. Laser was scanned at speed of 10mm/s, and the vertical shift between two scanning lines was 10µm. As the power increasing, the affected depth increases because of bigger laser power input. The total affected depth changed from 100µm, 150µm to 200µm for the power level of 1.8W, 2.4W and 3W respectively.

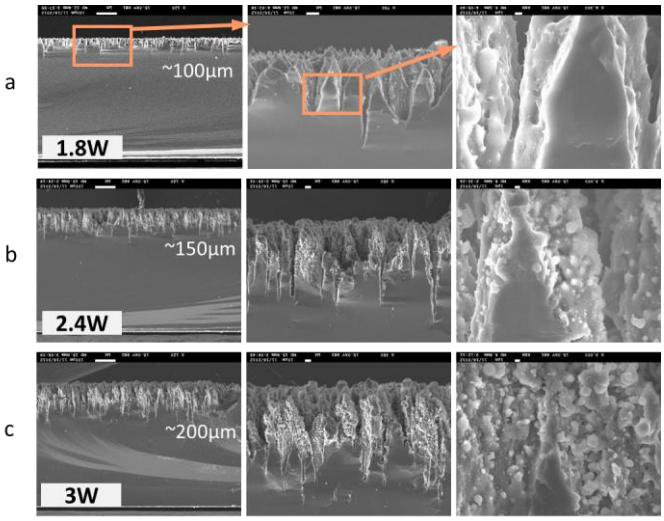

Figure. 5.3.2: Cross sectional SEM image of 532 nm green nanosecond pulsed laser at the power of (a) 1.8W, (b) 2.4W, (c) 3W. (The scale bar is 100µm, 10µm and 1µm respectively).

In the affected region, the microstructures were formed based on laser induced localizing thermal capillary. For 1.8W case, the structures are more uniformed than other cases. Bigger power input will cause more damage to the surface because at those cases, higher temperatures were achieved, thus, stronger plasma effect will result in more active chemical reaction and physical phase change. The other interesting thing is the roughness of the spikes increased for higher power cases. This may because of two reasons: 1) ablated nanoparticles re-deposition, 2) higher temperature resulting in longer cooling time for molten liquid to reflow. This effect was more obvious with metals as it is discussed in following chapter.

Then, comparison results of different nanosecond lasers with 355 nm and 532 nm wavelength are presented in Figure. 5.3.3.

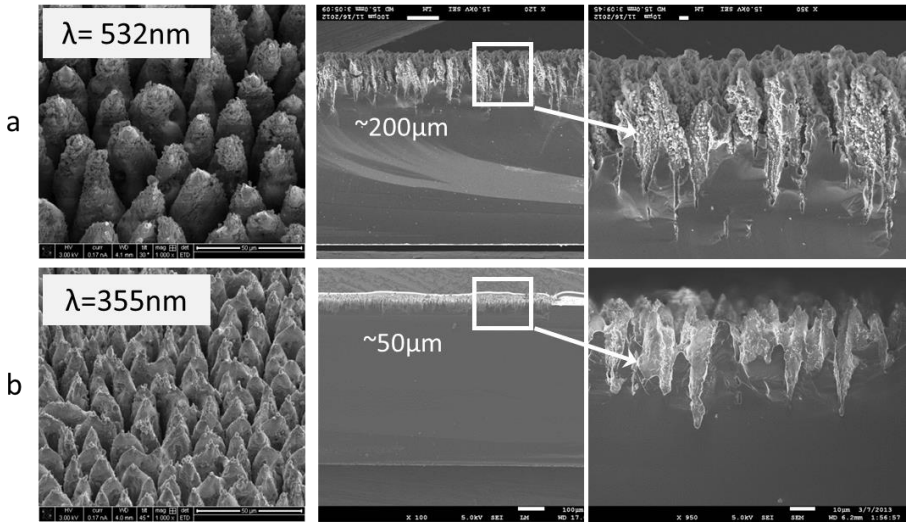

Figure. 5.3.3: SEM images of surface textured tilted view, cress section and magnified images for laser wavelength, power and repetition rate of (a) 532 nm, 3 W and 10 kHz (b) 355 nm, 0.9 W and 25 kHz, respectively.

From the SEM images shown in Figure. 5.3.3, it is obvious 355 nm UV nanosecond laser gives more sharp spikes because of its shallow melting depth during the laser treatment. The other significant difference is the total affected depth. The surface being irradiated by UV laser showed a very thin layer of the affected depth of around ~ 50µm while the green laser affected around ~ 200µm in this case. The zoom in SEM images of affected area also indicated that very good crystallinity achieved since the spikes were broken from the middle.

The silicon was chosen instead of metal because its brittleness, crystallinity (easy to break and breaking line tend to follow the crystalline direction) and less melting and ablation threshold which will make cross sectional SEM images feasible, as the same time, amplify the laser effect more obviously than metal.

5.4 Laser Micro-structuring of Copper Surface

Laser has been used widely as metal machining tool whether for scientific investigation and research or industrial applications such as laser welding and laser drilling. There is a time sequence for the laser heating of solid surface. Photons first interact with the free electrons in metal, then electrons reach equilibrium within 0.1 picosecond. Then electrons will affect phonon and reach equilibrium within a few picosecond. Thirdly, with 100 picosecond, plasma expansion happens. Finally after about 100 picosecond, acoustic wave is generated.

As a results, femtosecond and some short picosecond laser has been used for non-thermal processing while nanosecond laser has more emphasis on thermal process because its pulse duration is much longer than 100 picosecond (16ns second for green laser in this work).

Figure 5.4.1 shows a SEM image of 1064 nm nanosecond pulsed laser scanning line. There is a lot of ball shape particles at both side of the line which are solidified copper liquid droplets. Since the metal is very conductive of heat. The heat generated by laser will soon dissipate after the laser irradiation is turn off. This results in quick cold down of metal droplets and rapidly solidified. Because of high surface tension of liquid metal, liquid copper ten to shrink its shape to truncate sphere very similar with water droplets.

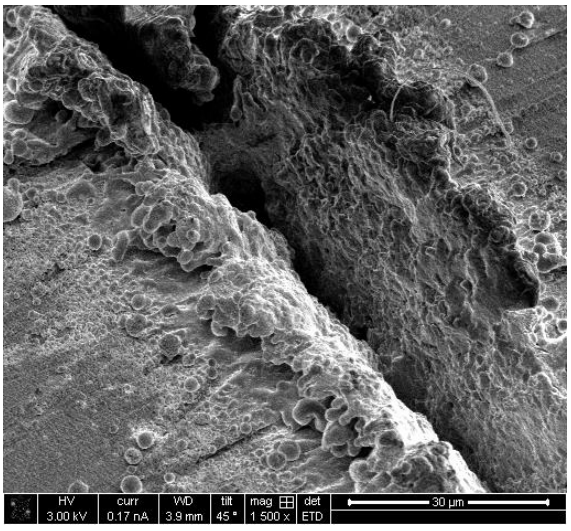

Figure. 5.4.1: 10 W near infrared (IR 1064 nm) nanosecond laser scanning line on copper.

5.4.1 532 nm Nanosecond Laser Structuring

Cu (99.9%) sample was cleaned with acetone before the laser processing. Areas of 3 mm by 3mm were processed with 532 nm green laser focusing with Mitutoyo M plan (5x) lens at scanning speed of 10 mm/s and 10μm spacing between two scanning lines. The laser repetition rate is 10 kHz. Experiments of power variation between 3.46W and 1.6W were performed. (Figure. 5.4.2)

Figure. 5.4.2: Photograph of laser textured copper surface by green nanosecond laser. Laser powers from upper right to lower left are 3.46 W, 3.2 W, 3W, 2.8 W, 2.6 W, 2.4 W, 2.2 W, 2W, 1.8 W and 1.6 W respectively.

After the laser texturing, SEM images of all the laser irradiated area were taken in Helios dual beam SEM/FIB machine in the clean room located in Center of Functional Nanomaterials in Brookhaven National Laboratory. The corresponding SEM images are presented in the Figure 5.4.3.

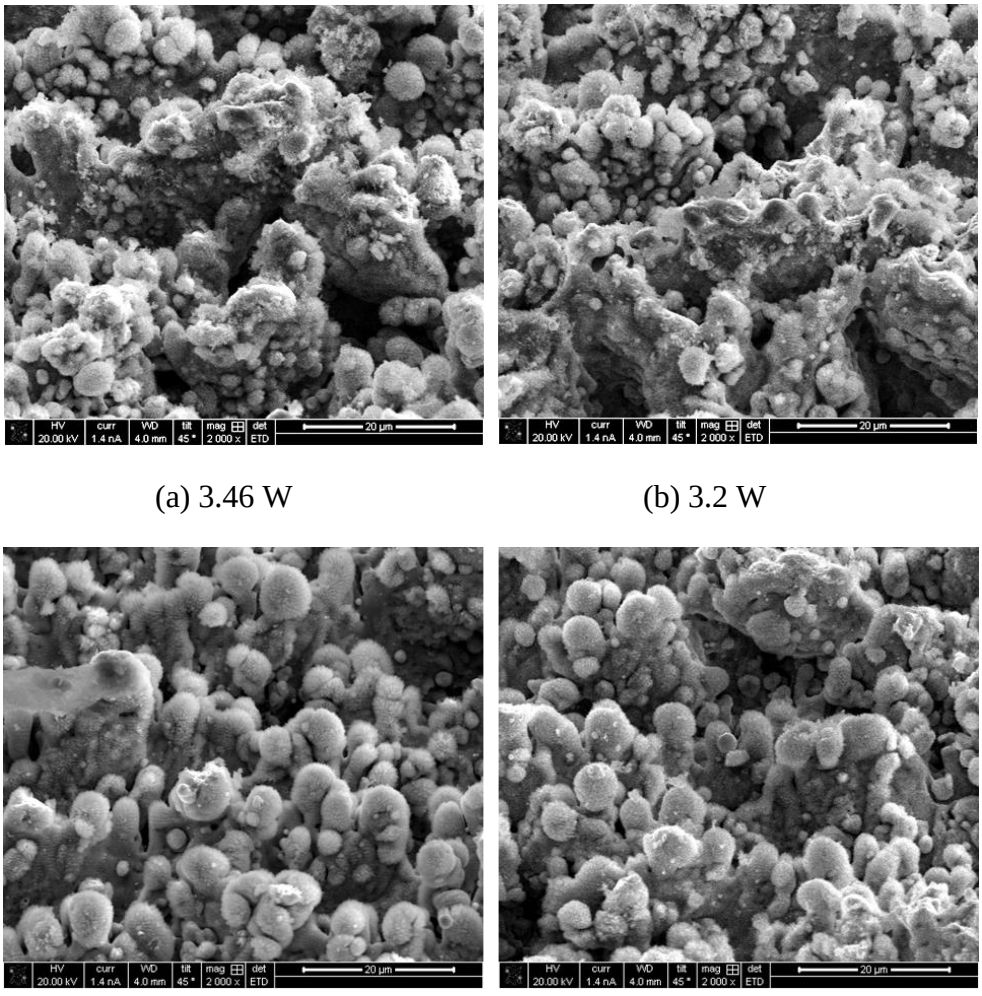

(a) 3.46 W (b) 3.2 W

(c) 3 W (d) 2.8 W

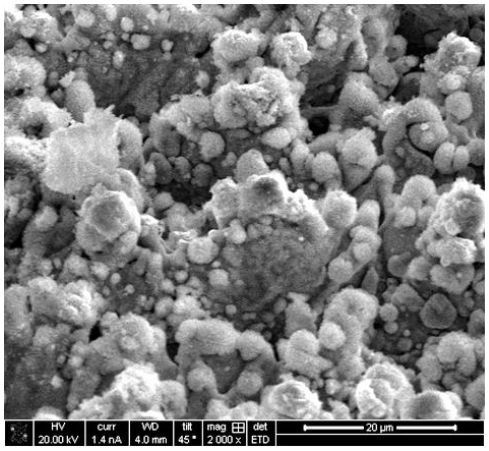

(d) 2.6 W

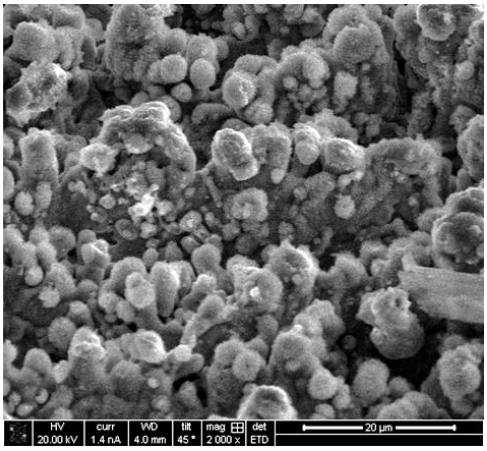

(e) 2.4 W

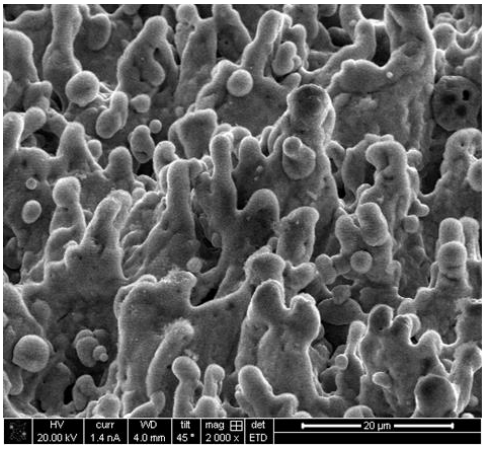

(f) 2.2 W

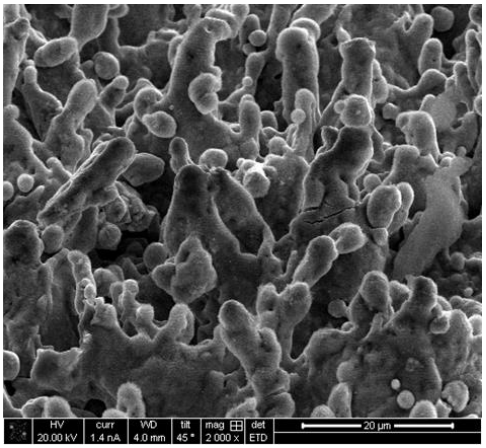

(g) 2 W

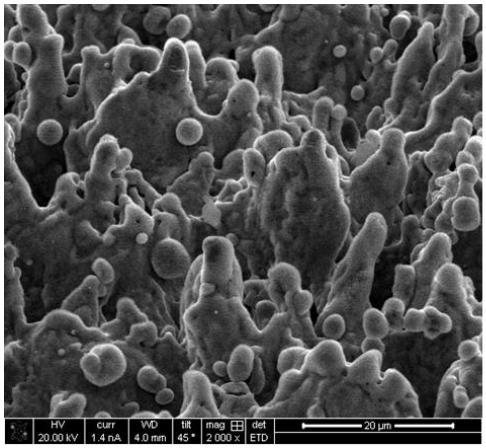

(h) 1.8 W

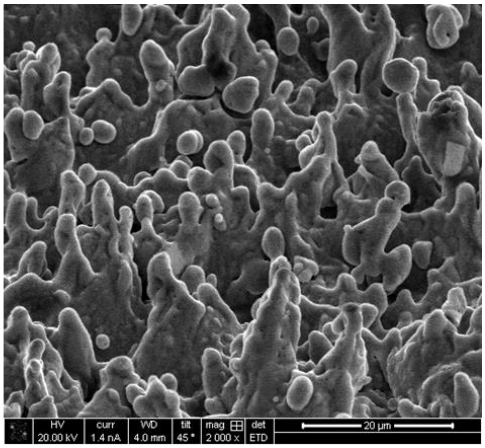

(i) 1.6 W

Figure. 5.4.3: SEM images of 532 nm green nanosecond laser textured area with power variation at 10mm/s and 10µm line spacing. Power from (a) to (i) area shown below of every SEM image.

With similar explanation of laser texturing on silicon surfaces. For cases of power range from 2.4W to maximum power 3.46W, liquid copper was formed like discussed previously in IR laser scanning line on copper. The difference is that possible CuO nanowire growth on top of the copper balls in hair-shape. But these hair-shape nanowires were compromised when the laser power is either too high 3.46W and 3.2W or two low 2.6W and 2.4W. Sudden change happen when the laser power were dropped below 2.4W from 2.2W to 1.6W. Sudden change of laser ablation domination to melting domination happened between the power level of 2.2W and 2.4W.

More detailed parameter study was performed on another copper piece with total dimension of 35mm by 25mm (Figure. 5.4.4). Each processed area was 3mm by 3mm. Different laser parameters such as laser power variation (from 3.2W to 1.4W) scanning speed (10, 20, 30, 40, 50mm/s), the scanning line spacing of (10, 20, 30, 40, 50, 60μm) were tested.

Starting from the column on the left, from bottom to top, on first two columns, the laser power form 3.2W to 1.4W with power decreasing step of 0.2W has been used. And scanning parameter fixed at speed of 10mm/s and 10μm line spacing.

On the third column to the left, laser power and scanning speed were fixed at 3.2W and 10mm/s respectively. Starting from bottom, the line spacing was shifted from 20μm to 60μm with increasing step of 10μm.

On the forth column to the left, laser power was still kept at 3.2W as well as the line spacing was constant at 10μm, the scanning speeds used were 20mm/s to 60mm/s from bottom to top.

On the fifth column to the left, laser power remained at 3.2W and line spacing was moved and stayed at 30μm. Starting from bottom, first two area use the scanning speed of 20mm/s, the difference is the second area is overlapped with vertical raster scan after the initial horizontal scan. The third and fourth area used scanning speed of 30μm and scanning direction is vertical and horizontal respectively. The area on the top scanned at 40mm/s.

On the sixth column to the left, laser scanned vertically and line spacing was fixed at 10μm. From bottom to top, scanning speed varies from 10mm/s to 50mm/s with 10mm/s increasing step.

On the second column to the right, laser was scanned at 50mm/s with line spacing from 20μm to 50μm from the bottom. The top one is vertical scan with 20μm line spacing.

On the first column to the right, vertical scanning method was used at the speed of 50mm/s by changing power from 3W to 2.2W starting from the bottom.

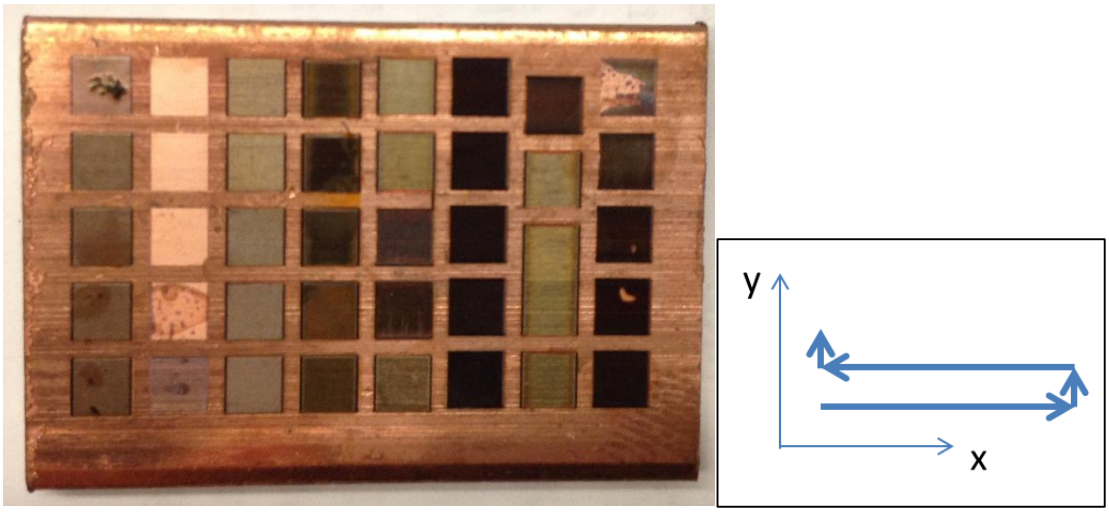

Figure. 5.4.4: (Left) Photography of 532nm nanosecond texturing on copper for detailed parameter studies and (Right) horizontal scanning direction. Vertical scan mean scan along Y direction while shift along X direction.

The original surface has groove with horizontal orientation. This affected laser scanning results by changing scanning directions. Since the surface groove is horizontal orientated, vertical scanning method showed on the sixth column to the left actually make copper more black by increased aspect ratio of structured asperities. (Figure. 5.4.4)

Selected SEM images of several cases of different laser and scanning parameters are presented in Figure 5.4.5.

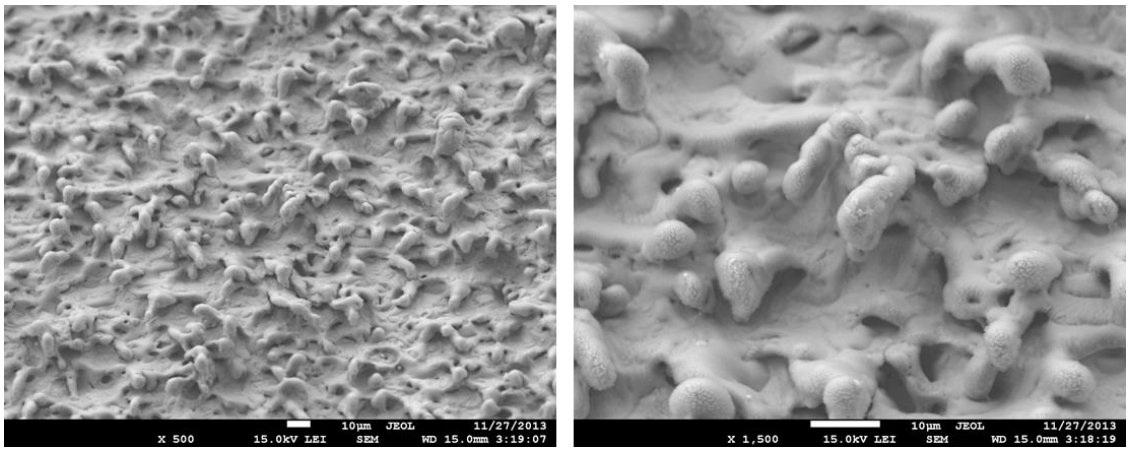

(a) Power 3.2W, scanning speed 10mm/s, line spacing 10µm, scanning direction horizontal

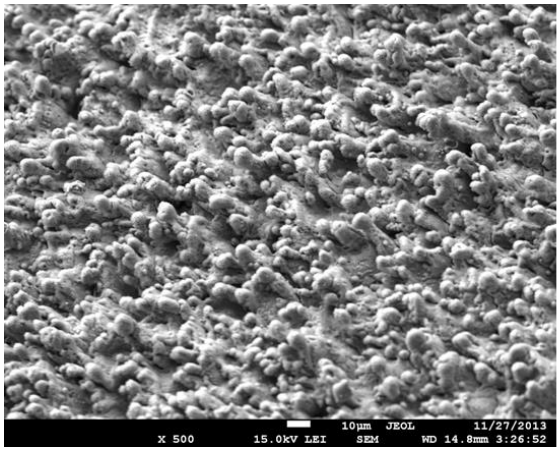

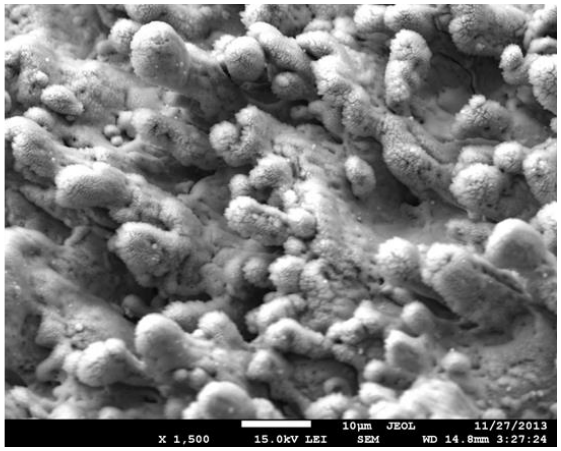

(b) Power 3.2W, scanning speed 10mm/s, line spacing 10µm, scanning direction vertical

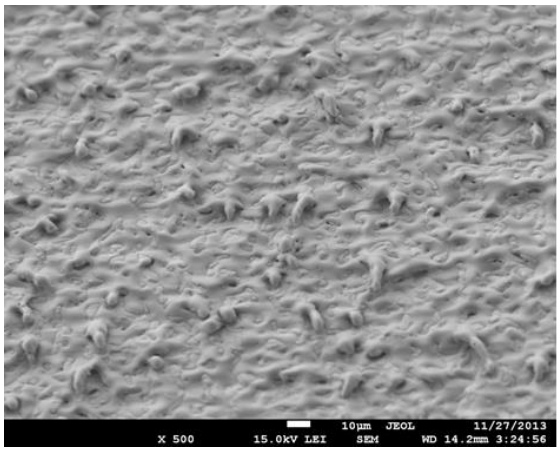

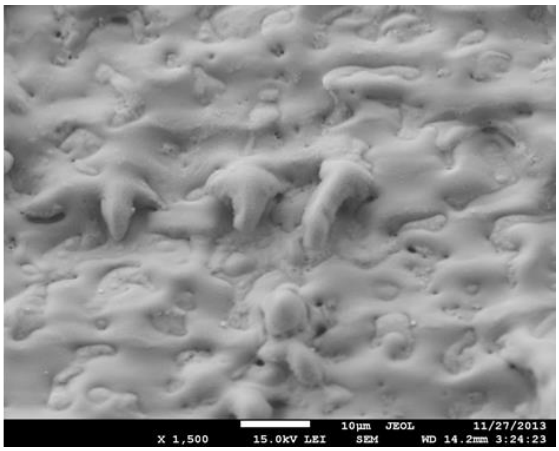

(c) Power 2.6W, scanning speed 10mm/s, line spacing 10µm, scanning direction horizontal

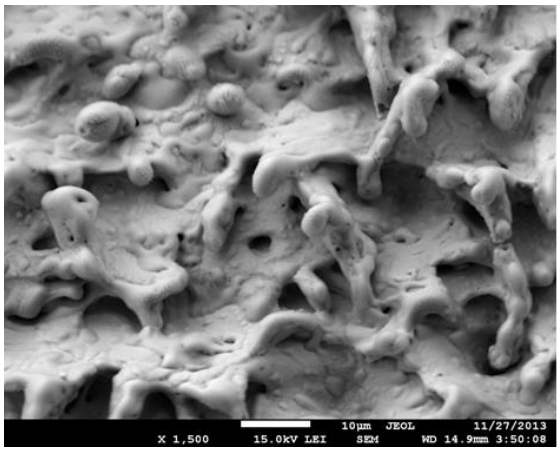

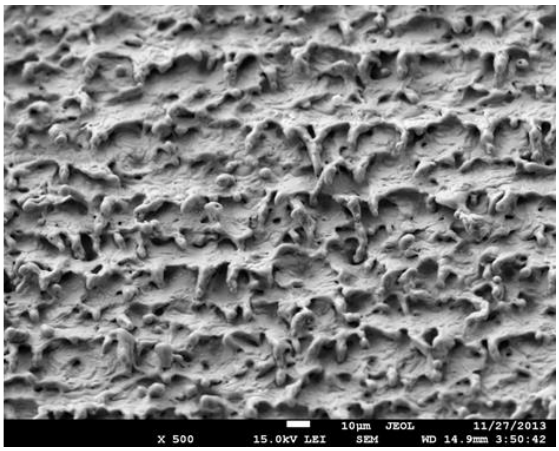

(d) Power 3.2W, scanning speed 10mm/s, line spacing 20µm, scanning direction horizontal

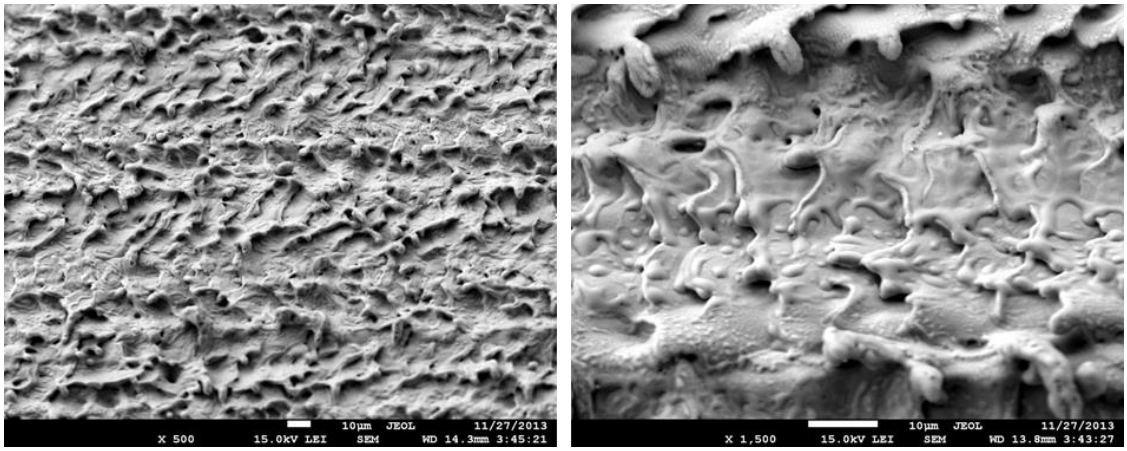

(e) Power 3.2W, scanning speed 10mm/s, line spacing 60µm, scanning direction horizontal

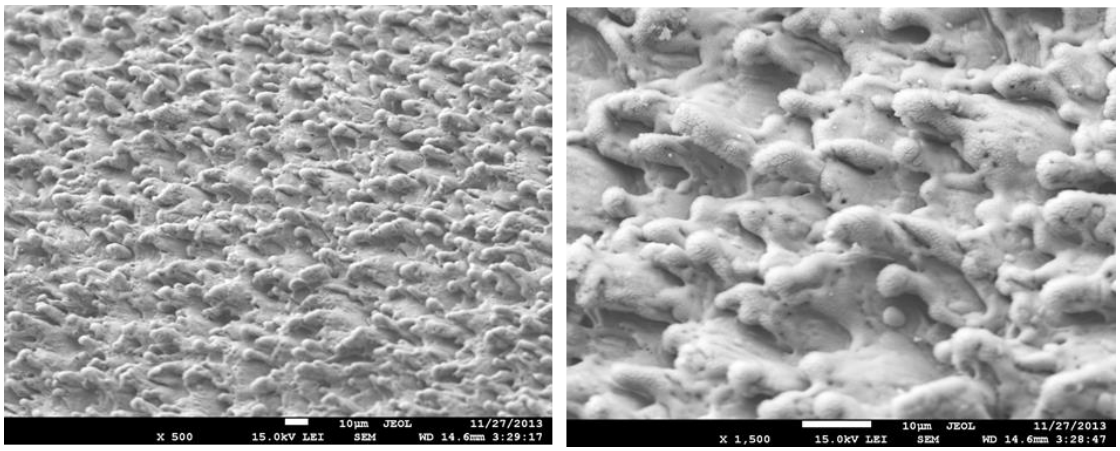

(f) Power 3.2W, scanning speed 20mm/s, line spacing 10µm, scanning direction horizontal

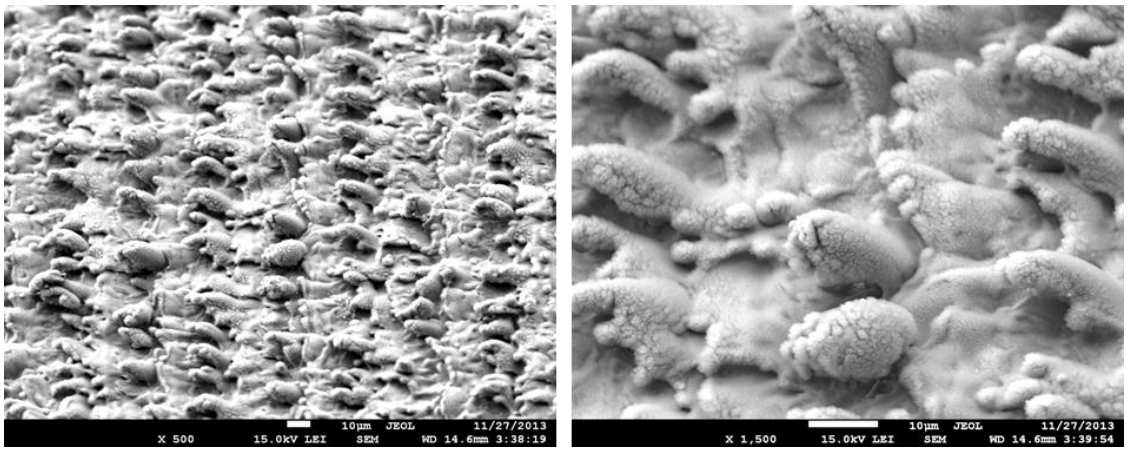

(g) Power 3.2W, scanning speed 20mm/s, line spacing 30µm, scanning direction horizontal (First Scan) and vertical (Second scan overlap on same area)

Figure. 5.4.5: SEM images of copper surfaces structured by different laser and scanning parameters.

5.4.2 1064 nm Nanosecond Laser Structuring

1064 nm wavelength IR nanosecond pulsed laser has been used in this work. Without further detail parameter study of this laser results, texturing on copper was also achieved and black copper was obtained. (Figure. 5.4.6)

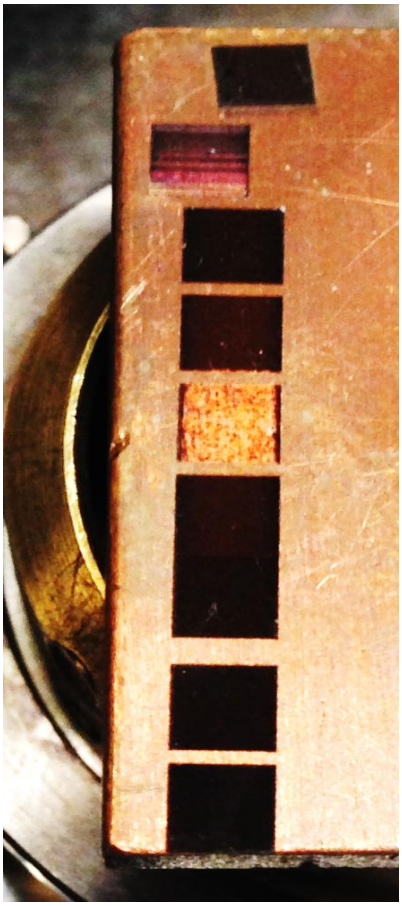

Figure. 5.4.6: Photograph of laser structured black copper with IR nanosecond laser.

Each area is 3mm by 3mm square with laser scanning parameter the same as for green laser (10mm/s and 10μm line spacing). From top to the bottom, there are 9 areas. Area 2 is practice area for testing at what power level it will become black or textured. Area 5 is power below threshold of ablation and copper mild melting was observed. The laser powers for all other cases were located in 10-20W. Starting from smallest power to the maximum power is 10W, 11.5W, 13W, 14.5W, 16W, 17.5W and 20W area 4, 6, 7, 8, 9, 3, 1. And the corresponding SEM images are in Figure 5.4.7.

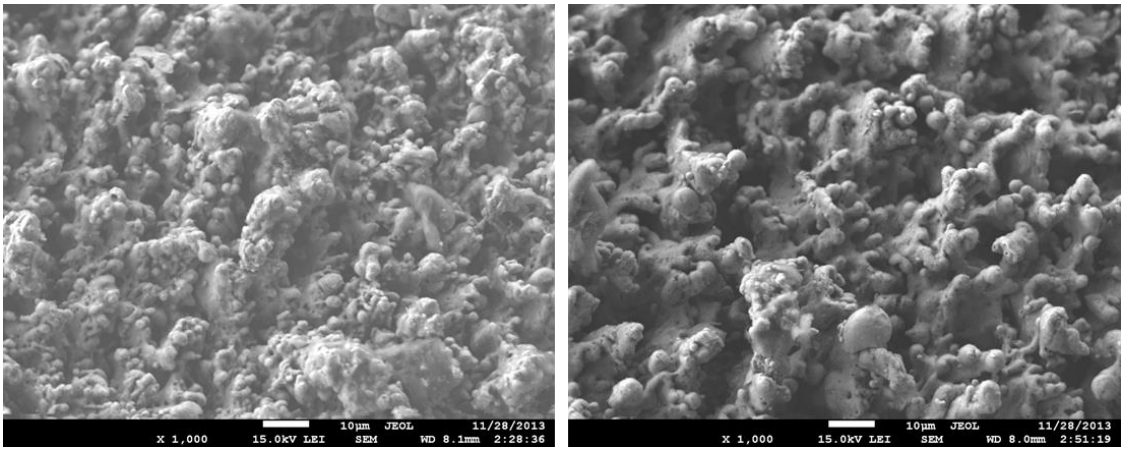

(a) Power of 20W (left) and 17.5W (right)

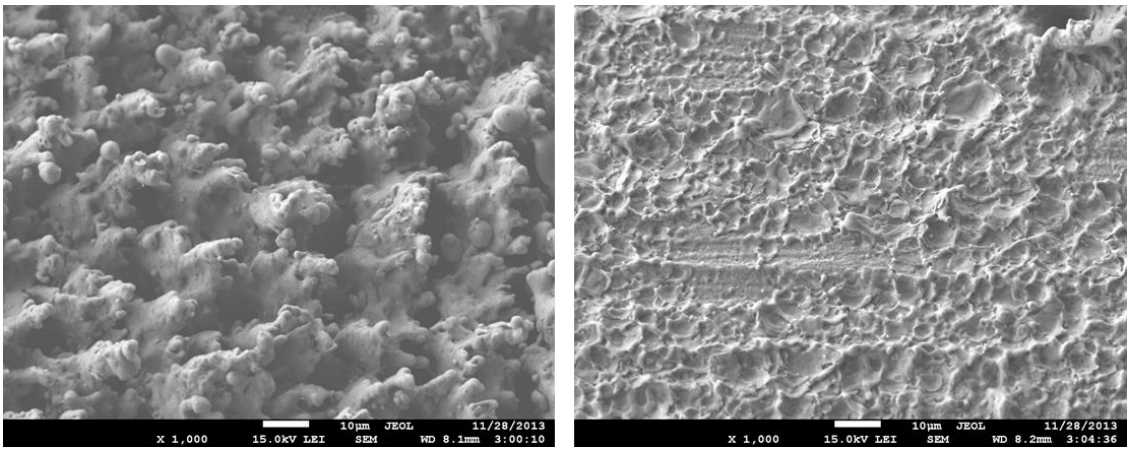

(b) Power of 10W (left) and 9W (right)

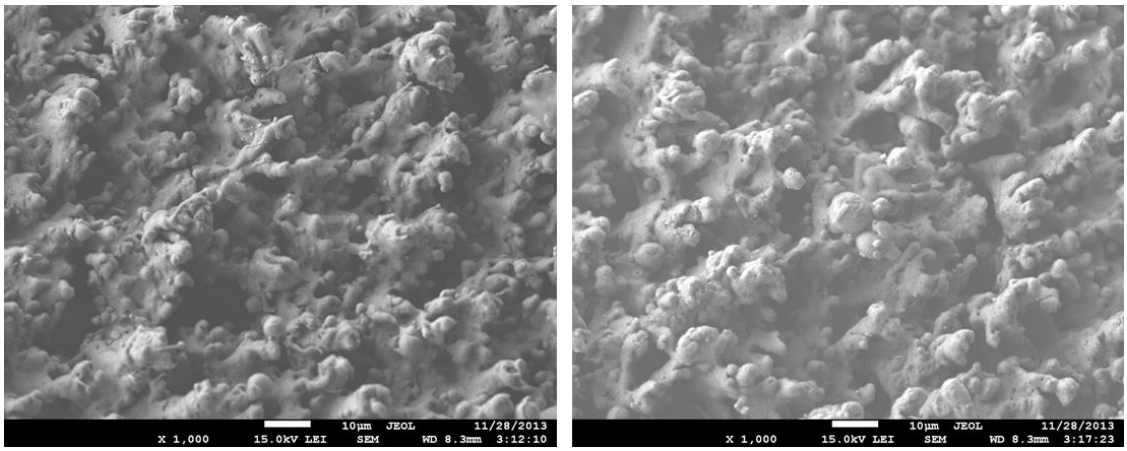

(c) Power of 11.5W (left) and 13W (right)

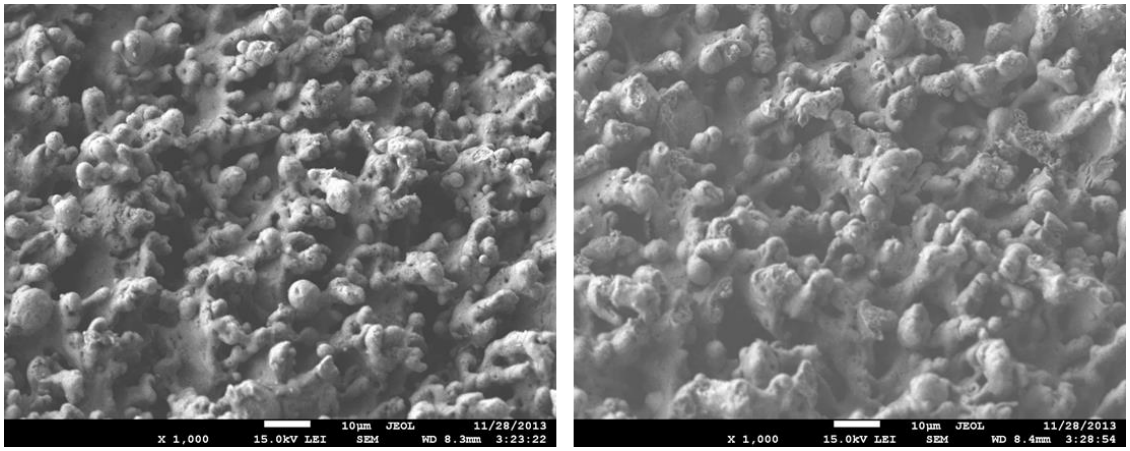

(d) Power of 14.5W (left) and 16W (right)

Figure. 5.4.7: SEM images of IR nanosecond laser texturing on copper surface.

As shown in Figure 5.4.7, IR laser structuring was totally different from green laser. Area 5 was not black because the power was not sufficient enough to induce the light trapping structures. The formation of CuO may be one addition reason why the textured copper looks black. When the power exceeded the ablation threshold, strong ablation happened. 1064 nm wavelength laser has been proved to have very strong interaction with plasma which is the reason for nanoparticles decoration on the micro-scale asperities.

5.5 Laser Micro-structuring of Stainless Steel.

Stainless steel 304 alloy was used in this study, which was irradiated by scanning of 532 nm green nanosecond pulsed laser with 10µm line spacing. Focusing lens is Mitutoyo M plan 5x. Scanned area was 3mm by 3mm squares. Two sets of laser parameter have been used. Upper two lines are results of the scanning speed of 10mm/s power variation study. Starting with top right, the power decreased from 3.25W to 0.5W at the last case on the left of second line. Lower line are laser textured area with scanning speed of 20mm/s. (Figure. 5.5.1)

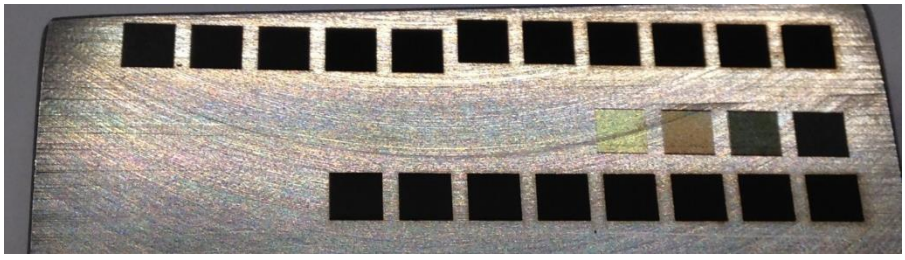

Figure. 5.5.1: Photograph of laser micro-structured stainless steel. Data set No. 1 (upper two lines) : scanning speed 10mm/s, power (starting from upper right to lower left): 3.25W, 3.1W, 2.9W, 2.7W, 2.5W, 2.3W, 2.1W, 1.9W, 1.7W, 1.5W, 1.3W, 1.1W, 0.9W, 0.7W and 0.5W. Data set No.2 (lower one line): scanning speed of 20mm/s, power (from right to left): 3.05W, 2.9W, 2.7W, 2.5W, 2.3W, 2.1W, 1.9W and 1.7W.

The complete sets of SEM images are shown in nest session of this chapter and their hydrophobicity test results will also be disclosed and discussed. At the low power of the data set No. 1 with scanning speed of 10mm/s from 0.5W to 0.9W, different colors appeared. This initiated another application of laser colorizing stainless steel (more discussion will be provide in Chapter 8. Two different microstructures were achieved for the power of 1.9W and above, and the power of 1.7W and below (Figure. 5.5.2). There exists one power level around some threshold value to separate two kinds of microstructures. For laser power of 1.9W, single independent spike was achieved while for 1.7W case, the structures became more like scribed lines with around 10μm width for each lines.

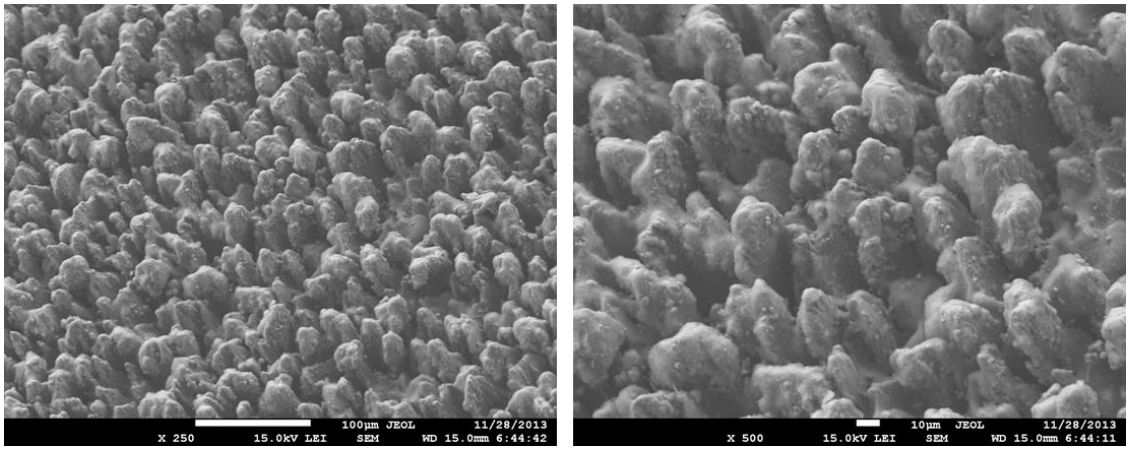

(a) SEM images of laser microstructures for the power of 1.9W

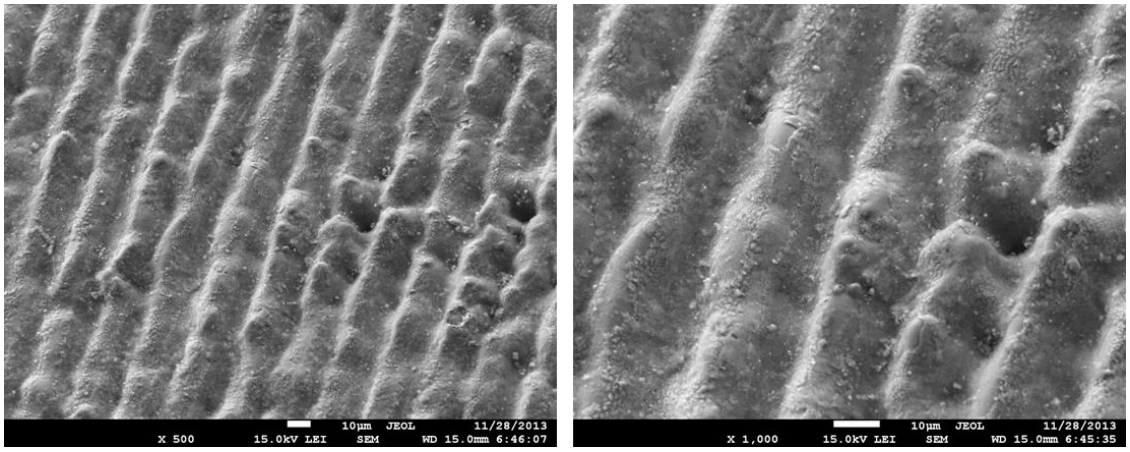

(b) SEM images of laser microstructures for the power of 1.7W

Figure. 5.5.2: SEM images of laser microstructures of different morphology.

For the data set No. 2, this change was more gradual as shown in Figure 5.5.3. For the highest power of 3.05W case, it is more similar than the case of data set No.1 where individual spikes were formed. For lowest power of 1.7W case, it looks like laser scribed lines. No sudden

change here, instead, the two different kinds of structures are gradually transform from 3W to 1.7W.

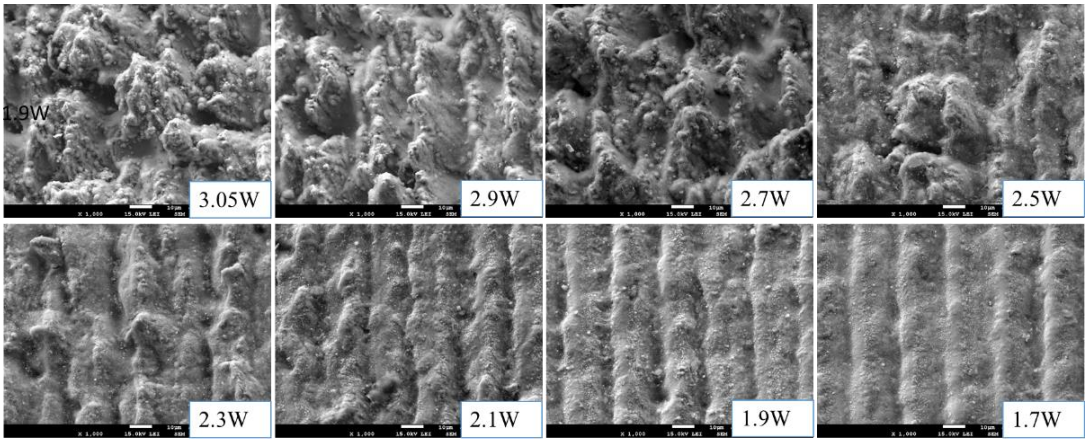

Figure. 5.5.3: SEM laser microstructures for data set No. 2.

5.6 Contact Angle Measurement

The contact angle θ is the angle between the gas-liquid interface and liquid-solid interface which shows the degree of surface wetting (Surface Wettability). And one the microscope side-view image is presented here as an example of the how to measure the contact angle. (Figure. 5.6.1)

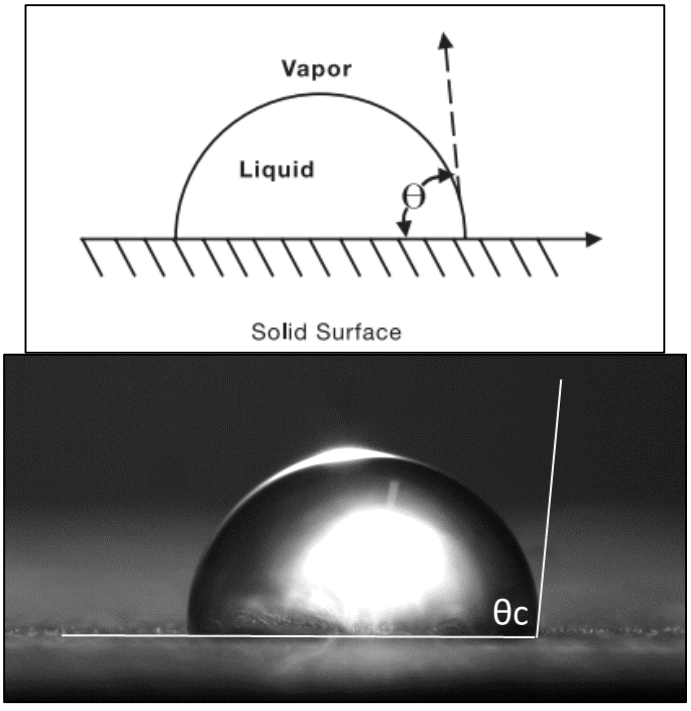

Figure. 5.6.1: Illumination of the concept of contact angle and one microscope side-view image of water contact with non-processed copper with θc=95°.

Laser ablation and laser-induced localized capillary effect discussed in previous chapters were responsible for generating microstructures to make the surface rough. Figure 5.6.2 shows a microscope image zoomed in the rough surface and there is clear comparison of the laser structured surface and flat non-structured surface.

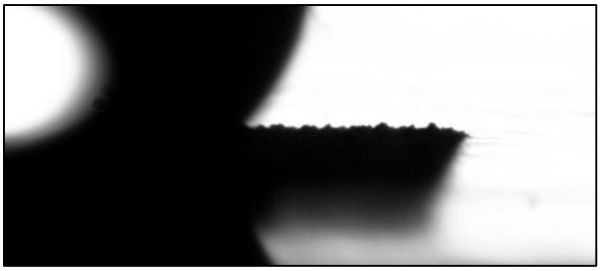

Figure. 5.6.2: Zoom-in microscope image of the roughness comparison between laser structured surface and non-structured surface during contact angle measurement. (The sample is stainless steel textured by green nanosecond laser).

As showed in Figure. 5.6.2, balanced of surface tension drove the water droplets to shrink to spherical shape which indicated the surface wettability was altered by laser processing. In fact, right after laser processing, all the laser treated areas tend to be more super-hydrophilic with contact angle smaller than 5 °. This phenomenon has been studied by A. M Kietzig et al. [63] (2009) by femtosecond laser on different steel including stainless steel alloy 304 and M. Tang [26] (2012) by UV nanosecond laser textured surfaces on brass.

5.6.1 Contact Angle Measurement for Laser Micro-structured Copper Surface.

Copper (99.9%) was textured by 1064 nm IR nanosecond laser here to generating microstructures on the copper surface and the SEM of the detailed laser-structured surface has been shown in Figure. 5.4.7 in previous chapter.

From the Figure. 5.6.3, it can be clearly observed the surface wettability difference from original untreated surface with laser-structured surfaces.

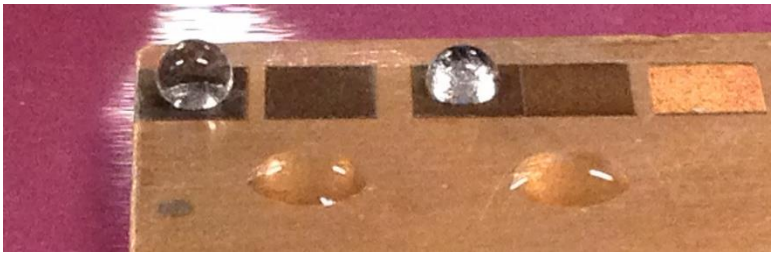

Figure. 5.6.3: Photography of the water droplet stay spherical shape on laser textured area and water tend to spread over the copper surface.

Initially, sample surface right after the laser process is super-hydrophilic which is because of the strong oxidation happened during laser ablation. After the sample was placed in

the air condition for around one month. And different laser scanning parameter will result in the different surface morphology thus affected the surface contact angle.

In Figure. 5.6.4, dark field image was taken using optical microscope with10x Mitutoyo lens by applying the illumination light from the side. Dark field image contains the information of surface roughness. As shown in the figure, the peak of spikes are bright and white, and gaps between different spikes are dark and black because the shadow of spikes is enhanced. The roughness of surface will be different if the aspect ratio of spikes are different.

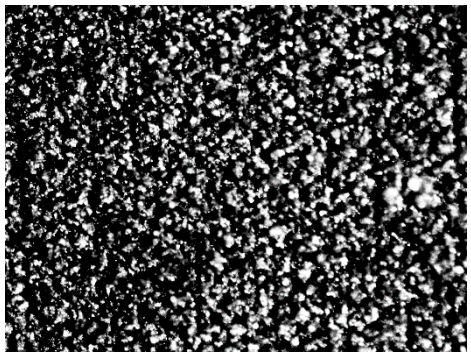

Figure. 5.6.4: Dark field image of laser structured copper surface (16W).

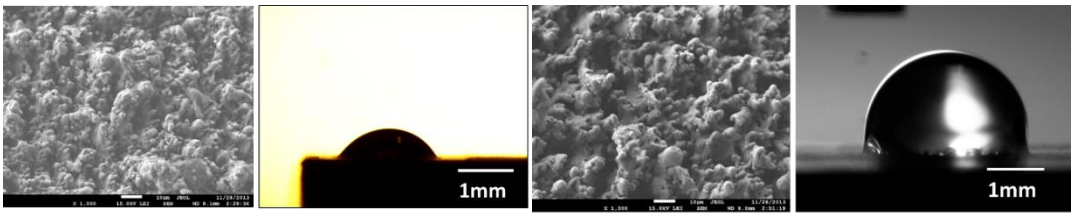

(a) 20W (left two images) and 17.5W (right two images)

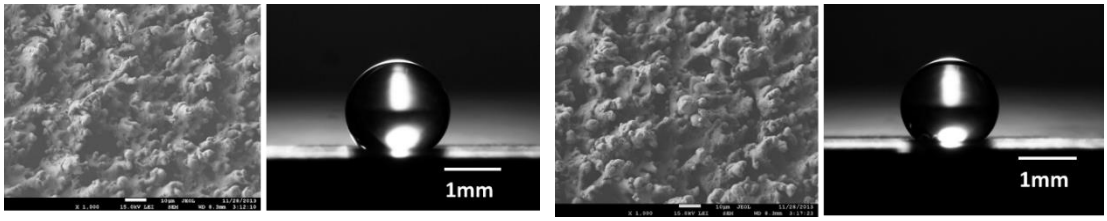

(b) 11.5W (left two images) and 13W (right two images)

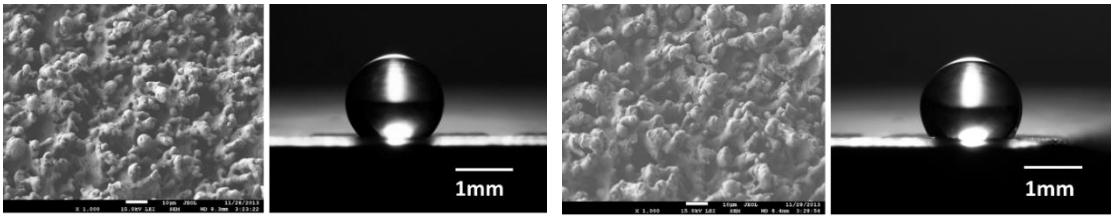

(c) 14.5W (left two images) and 16W (right two images)

Figure. 5.6.5: SEM images and optical microscope images of water contact with surfaces (copper) structured with different laser power 11.5W, 13W, 14.5W, 16W, 17.5W and 20W.

The contact angles were measured for each power case. SEM images with corresponding optical microscope images to measure the static contact angle are presented in Figure 5.6.5. There is big shift of contact for different power cases. Especially for 20W case, the contact was very small and surface was considered hydrophilic.

The corresponding contact angle and laser power relation is list in Table. 5.2. For 20W, because the power of laser was relatively big together with other reasons such as the high overlapping by scanning 10mm/s and between two scanning lines by line spacing 10μm, laser tent to damage the surface more resulting in ununiformed structures with different height of spikes as it is shown in Figure 5.6.5a.

Table. 5.2: Contact angle measurement results for copper.

Power (W)	Contact angle (٩)
20	57
17.5	83
16	123
14.5	125
13	150
11.5	151

As it is shown from the Table. 5.2, the contact angle increases with laser power decreases at this scanning conditions. Plotting contact with respect to laser power is presented in Figure. 5.6.6, for better demonstration of this trend.

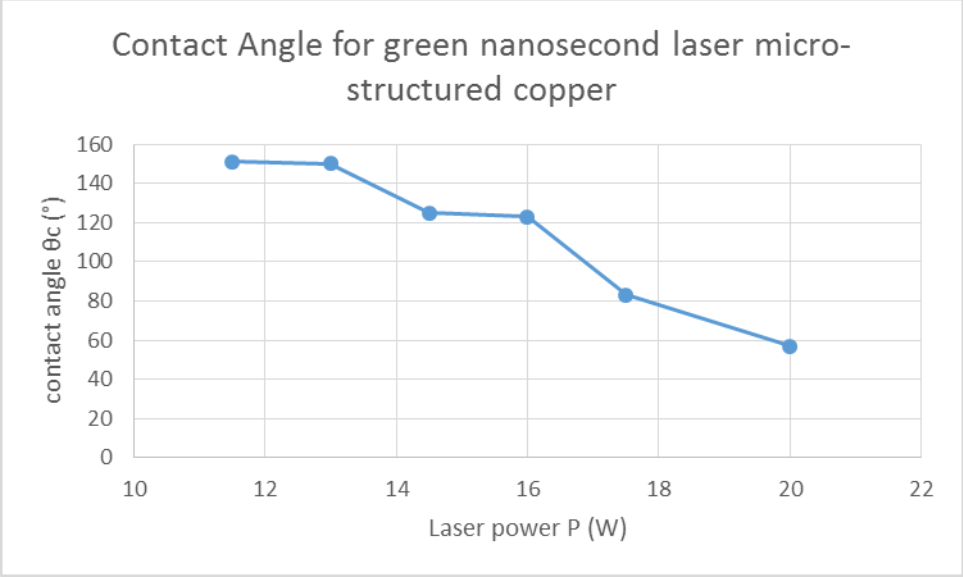

Figure. 5.6.6: Contact angle with respect to laser power for copper.

5.6.2 Contact Angle Measurement for Laser Micro-structured Stainless Steel Surface.

Stainless steel 304 was used in this study with 532nm green nanosecond laser focusing with Mitutoyo 5x lens. A photograph of water droplets resting on laser micro-structured surface and non-structured surface is present in Figure. 5.6.7.

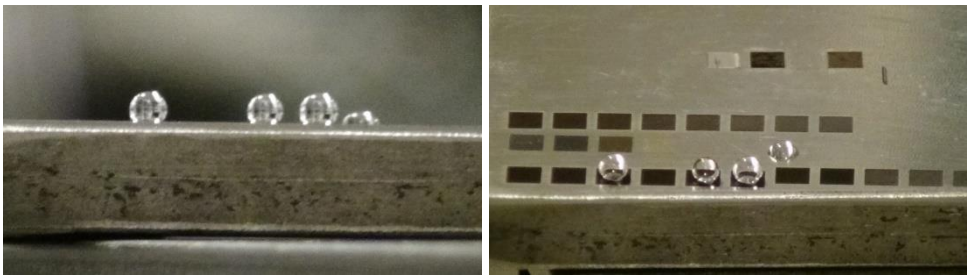

Figure. 5.6.7: Photographs of water droplets resting on top of structured and non-structured surfaces for stainless steel 304 sample.

As discussed previously, two types of surface structures were formed by laser scanning of stainless steel and the dark field images of each case in data set No. 1 is shown in Figure. 5.6.8.

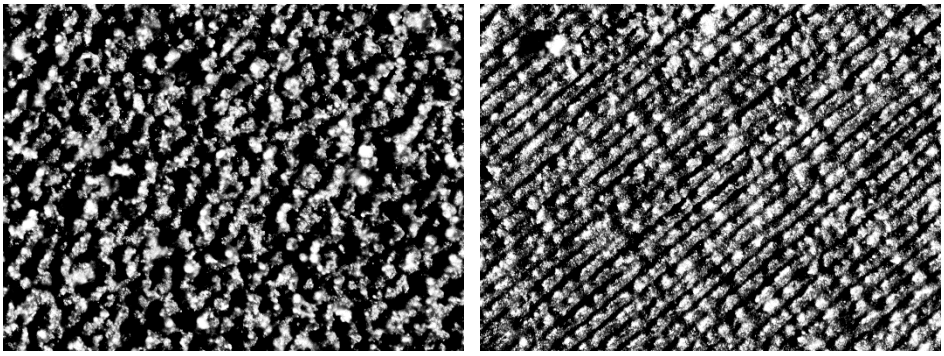

Figure. 5.6.8: Dear field images of the laser power at 1.9W (left) and 1.7W (right).

Contact angles were measured after one month of sample placing in air similar with copper. Initially, right after the laser processing, the laser structured surface were all super-hydrophilic. After two months, super-hydrophobicity were achieved for some cases. There are two data sets of green laser process on stainless steel as discussed previously. For the data set No. 1, SEM and optical images are presented in Figure. 5.6.9. Laser was scanned at the speed of 10mm/s and line spacing was 10μm.

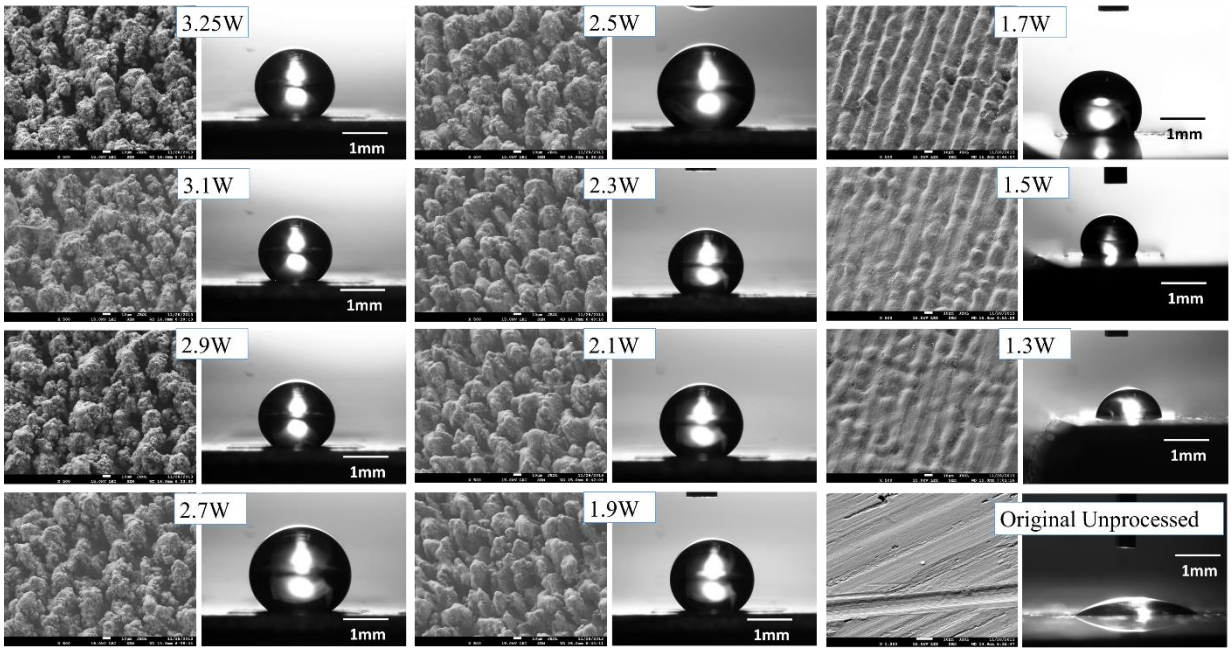

Figure. 5.6.9: SEM images and optical microscope images of water contact with surfaces (stainless steel), laser scanning parameter is 10mm/s of scanning speed and 10μm line spacing, power level are showed for each case.

The contact angle results corresponding to different laser power is provided in Table 5.3. Contact angle decreases with the laser power decreasing. For laser power 1.9W and above, contact angles remains at 160 °. Starting form laser power 1.7W, contact angle reduces to 135 ° and keep decreasing with laser power becomes smaller. (Figure. 5.6.10)

Table. 5.3: Contact angle measurement results for data set No.1 of stainless steel

Laser power (W)	Contact angle (٩)
3.25	150
3.1	149
2.9	149
2.7	150
2.5	151
2.3	149
2.1	150
1.9	149
1.7	135
1.5	120
1.3	82
N/A (Unprocessed)	31

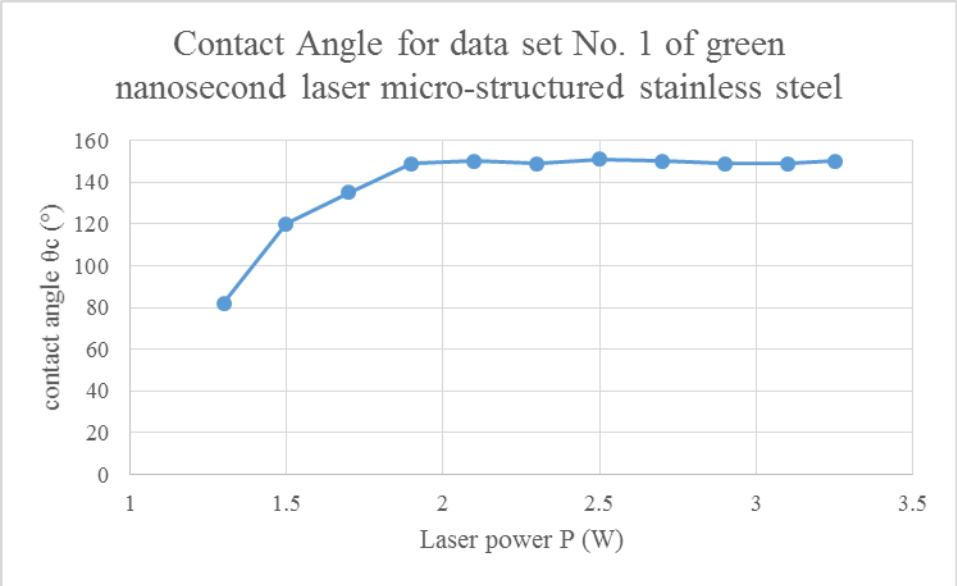

Figure. 5.6.10: Contact angle variation with respect to laser power for data set No. 1

For the data set No. 2, SEM and optical microscope images are presented in Figure. 5.6.11. Laser was scanned at the speed of 20mm/s and line spacing was 10µm.

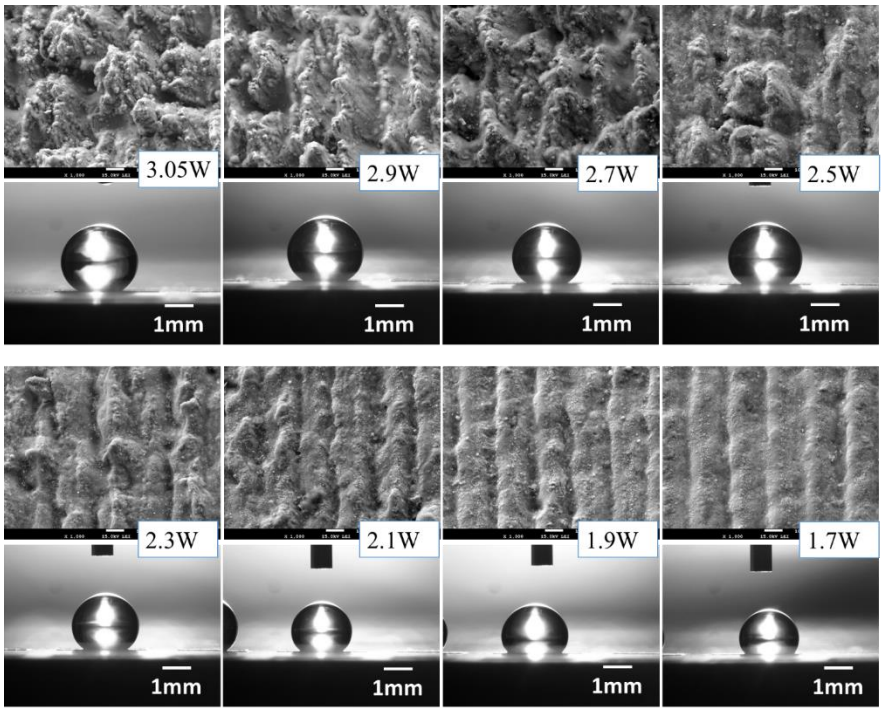

Figure. 5.6.11: SEM images and optical microscope images of water contact with surfaces (stainless steel), laser scanning parameter is 20mm/s of scanning speed and 10µm line spacing, power levels are showed for each case.

The contact angle results corresponding to different laser power is provided in Table 5.4. From the table, super-hydrophobic surface on stainless steel was formed by scanning 532nm green nanosecond laser by the speed of 20mm/s and 10μm line spacing. At the laser power of 2.5W, the contact angle reached the biggest value which is also the biggest possible contact angle value in this work for all the laser structured surfaces.

Table. 5.4: Contact angle measurement results for data set No.2 of stainless steel

Laser power (W)	Contact angle (٩)
3.05	152
2.9	158
2.7	159
2.5	161
2.3	155
2.1	156
1.9	142
1.7	136

Based on the Table 5.4, the contact angle does not follow linear relation with respect of power. Instead, the contact will increase from 152 °to 161 °and then decrease to 136 °with laser power decreasing. (Figure. 5.6.12)

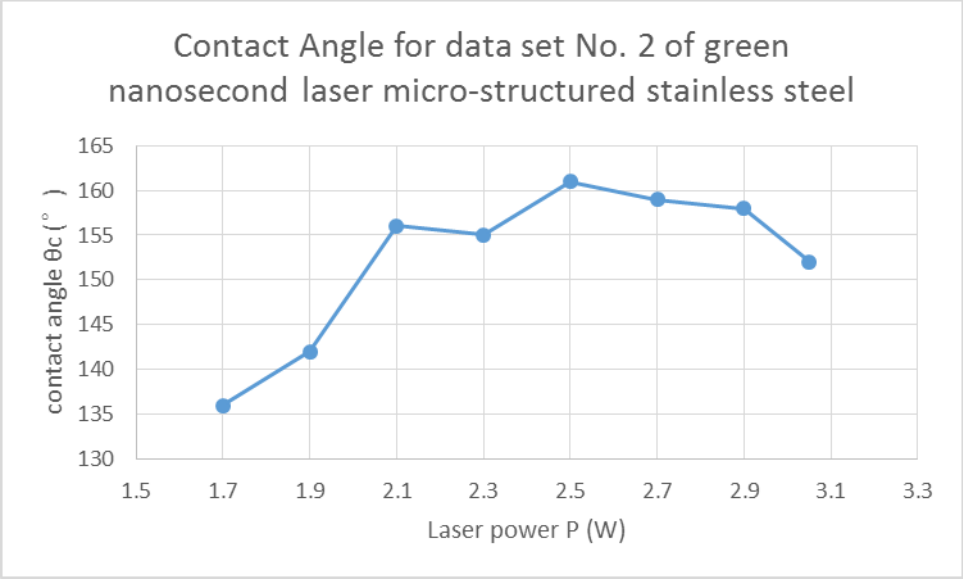

Figure. 5.6.12: Contact angle variation with respect to laser power for data set No. 2

5.7 Contact Angle Hysteresis

In Figure 5.7.1, a set of microscope images show the sequence of measuring contact angle hysteresis. Start from left, the volume of the water droplet is increasing and water begins to touch the surface. Further filling the water liquid will cause the water droplet size increase and begin to advance outward and advancing angle can be measured. After the third image, the liquid is pumped out of the droplet, resulting water volume decreasing. The fifth image is water begin to recede inward and receding angle can be measured. This phenomenon described here is called contact angle hysteresis, which is the difference between advancing and receding contact angle. If the difference is small the droplet experiences a low drag force from the surface and can easily roll off.

Figure. 5.7.1: Microscope images of sequence to measurement contact angle hysteresis. (3.25W of data set No. 1 on stainless steel)

The water droplet was finally all pumped back into the syringe pipe, while in other case, water droplet was not (Figure. 5.7.2). Instead, it was attracted to the surface which indicates a bigger hysteresis.

Figure. 5.7.2: Microscope images of water attracted to stay on the surface of high hysteresis. (2.3W of data set No. 1 on stainless steel)

At some cases the water droplets shifted form center of pipet (Figure. 5.7.3). Red line in Figure 5.7.3 indicates the central axis of pipet and the water droplet shifted to the left since there was larger attraction on left part than right part of scanned area.

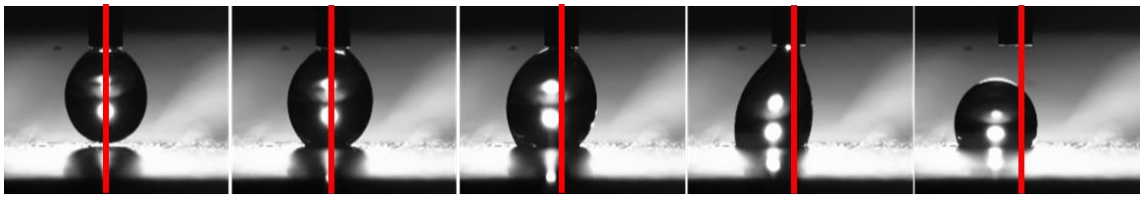

Figure. 5.7.3: Microscope image of water move to left because of surface uniformity (1.7W of data set No. 1 on stainless steel)

The hysteresis of copper surface are all over 60 °which means water is easy to be attached on copper surface.

Contact angle hysteresis results of data set No.1 on stainless steel are listed in Table 5.5.

Table. 5.5: Contact angle, advancing and receding angle and contact angle hysteresis measurement results for data set No.1 on stainless steel.

Laser power (W)	Contact angle ( )	Advancing angle θa (°)	Receding angle θr ( )	Contact angle hysteresis ( )
3.25	150	157	122	25
3.1	149	157	116	41
2.9	149	159	129	30
2.7	150	155	135	20
2.5	151	157	135	22
2.3	149	170	116	54
2.1	150	169	131	38
1.9	149	168	131	37

For power of 1.7W, 1.5W and 1.3W, contact angles were decreasing a lot as showed in Table 5.3. While their hysteresis were all increased over 60 °. Because of their directional water droplet shifting, the actual hysteresis varies at different locations within one scanned area.

Contact angle hysteresis results for data set No.2 of stainless steel are list in Table 5.6.

Table. 5.6: Contact angle, advancing and receding angle and contact angle hysteresis measurement results for data set No.2 on stainless steel.

Laser power (W)	Contact angle ( )	Advancing angle θa (°)	Receding angle Θr (°)	Contact angle hysteresis ( )
3.05	152	168	147	21
2.9	158	167	145	22
2.7	159	170	137	33
2.5	161	169	125	44
2.3	155	171	127	43

For laser power of 2.1W, 1.9W and 1.7W cases, contact angle hysteresis increased to a larger value and directional water droplets shift was also observed for these cases.

The high contact angle hysteresis may result from the existence of Wenzel State as it was described previously in the work. In Wenzel State, water reaches the bottom of cavities between asperities, resulting high contact angle hysteresis.

In addition, sliding test is not a favorable method to measurement hysteresis when hysteresis is relatively high because the water droplets are unable to slide on surface.

5.8 Chemical Components Analysis

Right after laser process, copper was oxidized in CuO (weight percentage ~23% from Table. 5.7) and then after placing in the air. The CuO was deoxidized in Cu_2O, which is hydrophobic material with original contact angle around 110 °. This phenomenon was also reported by Chang et al. that the partial deoxidation of the CuO (which is grown on top of copper oxide nanowires at 300 ℃) into Cu_2O happens when the sample is exposed to the air at room temperature [64]. This deoxidation process can explain why the oxygen concentration of the laser ablated surface reduced after the two months exposure in air environment.

EDS analysis results were obtained by analytical SEM (JEOL 7600F) with EDS function. In Figure 5.8.1, EDS results for copper surface are presented. From the Figure 5.8.1a, there was limited amount of oxygen element (from native oxide) before the laser process. Figure 5.8.1b shows the EDS results right after laser process. The high peak of oxygen signal indicates more oxygen existed in the sample which was mainly due to the highly active oxidation during the laser process. A good amount of CuO was then formed during the laser irradiation. After placing in the air environment for two months, from Figure 5.8.1c, the oxygen level became less which means CuO was partially deoxidized to Cu_2O.

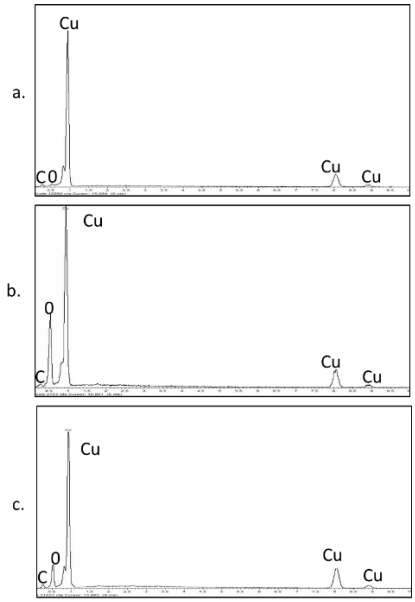

Figure. 5.8.1: EDS analysis of copper (a) before laser process (b) right after laser process (c) after laser process and place in air for two month.

Table. 5.7: Weight percentage of different elements on copper.

Weight percentage (%)	before laser process	right after laser process	after laser process and place in air for two month
C	1.74	1.94	2.48
O	0.65	22.56	13.42
Cu	96.67	60.88	84.1

Bhattacharya's findings on hydrophobic clustered copper nanowires [65] are, to the best of our knowledge, the only reports on altering a material's surface wettability from hydrophilic to hydrophobic without using a coating. As it is shown in Figure 5.8.1 and Table 5.7, the oxygen weight percentage increase a lot (from ~ 0.65% to ~ 22%) right after the laser process and then after staying in air environment for 2 month, it became less (~ 13%). Some of the CuO deoxidized to Cu_2O is responsible for this change. As discussed previously, Cu_2O will contribute the surface wettability transition from the super-hydrophilicity to super-hydrophobicity.

Stainless steel 304 chemical components analysis was also performed with EDS. As shown in Figure. 5.8.2.

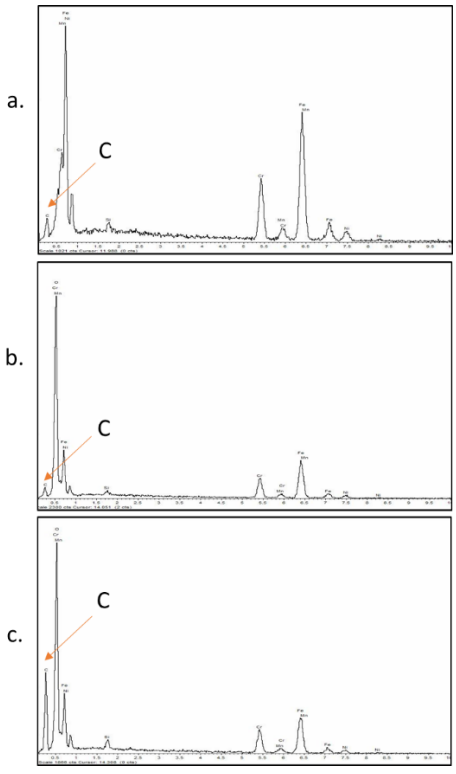

Figure. 5.8.2: EDS analysis of stainless steel (a) before laser process (b) right after laser process (c) after laser process and place in air for two month.

Table. 5.8: Weight percentage of different elements on stainless steel.

Weight percentage (%)	C	O	Si	Cr	Mn	Fe	Ni	Total
Before laser process	3.90	0	0.66	18.36	2.01	66.16	8.91	100.00
Right after laser process	3.43	33.27	0.45	12.89	1.47	42.94	5.53	100.00
After laser process and placed in air for two month	9.76	23.89	0.41	14.98	2.11	44.84	4.00	100.00

The change in wetting behavior resulted from the amount of carbon deposited on the structured surface. It is apparent that the relative amount of carbon increases with time, comparing the EDS results before laser process (Figure. 5.8.2a), right after laser irradiation (Figure. 5.8.2b), and after laser process and placing in air for two months (Figure 5.8.2c). Over time, nonpolar carbon was deposited and accumulated on the rough surface (carbon weight percentage increased from ~3.5% to ~10% from Table 5.8) in the air. Together with the laser-induced surface micro/nano-structures, the surface wettability was transferred to super-hydrophobicity.

5.9 Leidenfrost Effect

More than two hundred years, Leidenfrost described a remarkable behavior of liquid drops on a very hot plate, such as water on steel at 300 ℃. Leidenfrost drops are very easy moving [66]. And the liquid motion is driven by a liquid vaporization between the solid and the liquid. Copper surface was kept at 300 ℃ and water droplets was placed on top of two different surfaces: laser textured (Figure. 5.9.1) and original non-textured (Figure. 5.9.2) surface.

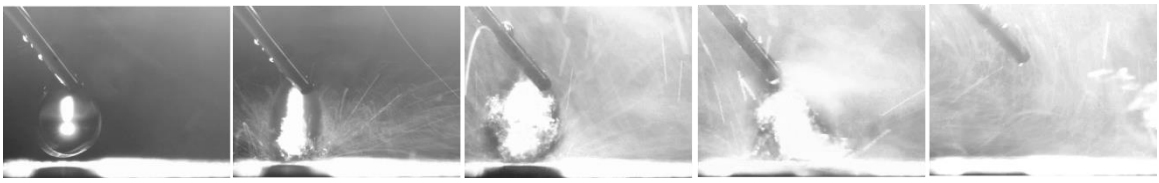

Figure. 5.9.1: Water droplet contact with laser-structured copper surface at 300 ℃. From left to right, volume was increased until the droplet moved away very fast.

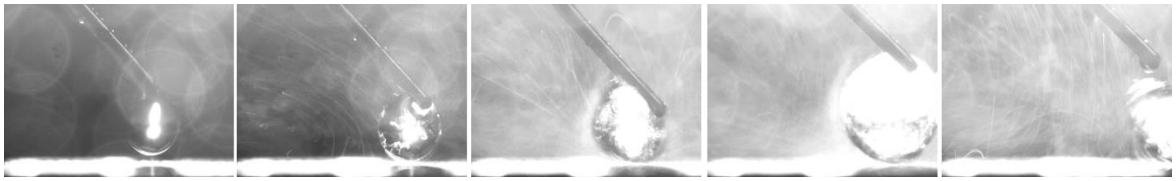

Figure. 5.9.2: Water droplet contact with non-structured copper surface at 300 ℃. From left to right, volume was increased until the droplet moved away.

From the images showed in Figure 5.9.1, the structured copper surface had very strong vaporization at the solid-liquid interface, resulting more unstable shape of water droplet until it was detached and moved away very fast. While on the original copper surface (Figure. 5.9.2), the vaporization was less and the water intent to keep its spherical shape until it was detached from the pipet and moved away relatively slower than the other case. Meanwhile, final volume of the droplet before detaching was bigger.

Then another test was performed by dropping water droplet from certain amount of height (Figure 5.9.3 and Figure 5.9.4) to the laser-structured and non-structured copper surface.

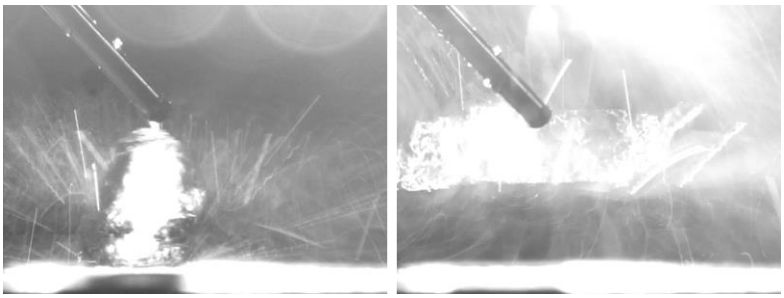

Figure. 5.9.3: Dropping one water droplet on laser-structured copper surface at 300 ℃. The water was attached to the pipet to keep spherical shape (Left) then water was detached and immediately "exploded" from the solid-liquid interface (Right).

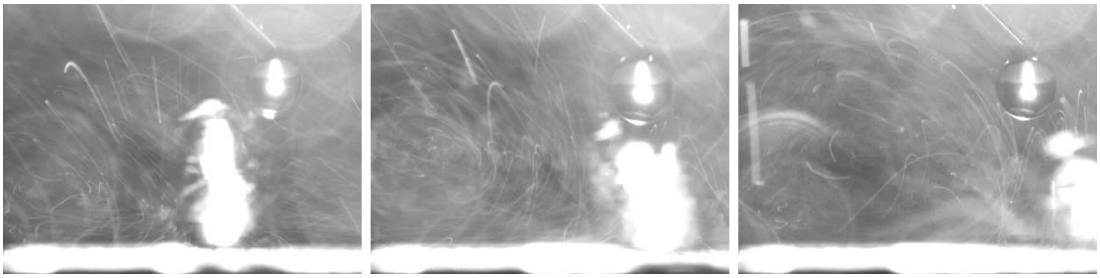

Figure. 5.9.4: Dropping one water droplet on non-structured copper surface at 300 ℃. Water droplet tend to bounce back and forth (Left two images) and then move away (Right).

After the Leidenfrost experiment by heating the copper in the air to 300 ℃ for 20 minutes, the original super-hydrophobicity of the copper surface was compromised to hydrophilicity. (Figure. 5.9.5).

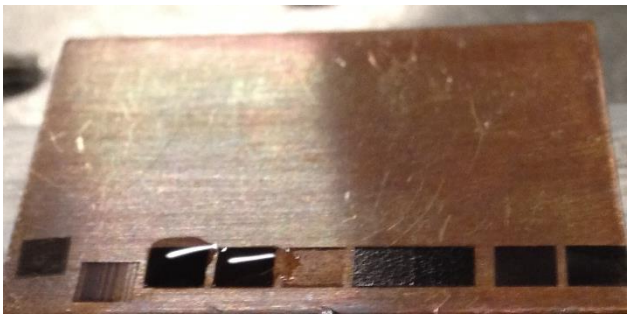

Figure. 5.9.5: Photograph of water contact with hydrophilic copper surfaces after heating up originally super-hydrophobic surfaces at temperature of 300 ℃ for 20 minutes.

Chapter 6: Future Works

For the surface morphology effect on the super-hydrophobic behavior, more detailed studies about different laser parameters (wavelength, power, repetition rate and pulsed duration), scanning parameters (scanning speed and scanning line spacing) and focusing conditions (different lens and focal positions) will be performed in future work. Different super-hydrophobic behaviors will also be studied correspondingly.

For the surface chemical analysis, a more precise chemical compositions analysis tool such as XPS will be used to quantitatively study the surface chemistry during surface wettability transition in air environment.

As discussed in this work, super-hydrophobicity only happened after placing the samples in the air environment for a certain period which is not well controlled engineering approach to form the super-hydrophobic surfaces. To solve this issue, more studies will be conducted to identify the exact mechanism of this transition to super-hydrophobicity in the air. Then, more controlled and fast approach should be provided in order to apply super-hydrophobic surface formation method to industrial level.

Another analysis will be conducted is the structural and chemical components changing along the depth by Focus Ion Beam (FIB) cross sectioning. Different oxidation may occur at the different depth. By the end of this FIB study, a clue of the oxidation formation and how it will affect the wettability of the surface will be provided.

There are more studies can be done on super-hydrophobic surfaces, such as experiments of liquid evaporation on surfaces in controlled environment (humidity and temperature) and anti-icing performance (Freezing rain and surface temperature below the freezing point of water).

Chapter 7: Conclusion and Summary

Super-hydrophobic metallic surface formation by short pulsed lasers has been studied in this thesis. Nanosecond pulsed lasers (wavelength of 532 nm and 1064 nm) were used here to scan on top of copper and stainless steel (304) surfaces. The resulting surface morphology and corresponding surface wetting performance (contact angles, contact angle hysteresis) was investigated as well.

Micro-structures on copper and stainless steel surfaces were generated by irradiating nanosecond pulsed lasers. Right after the laser processing, the surfaces were all super-hydrophilic instead of hydrophobic, resulting from the large amount of oxidation formation during the laser irradiation. Then after placing the sample in air environment for two month, the surfaces became hydrophobic and some were even super-hydrophobic.

In order to reveal the basic mechanism of super-hydrophobic surface formation, analysis of surface morphology, wettability and chemical composition was performed in this work. SEM images were taken for different laser micro-structured areas to show the basic morphology information. Besides, contact angle and contact angle hysteresis for different cases were measured correspondingly to indicate surface wettability. In addition, EDS (chemical composition analysis) results were also provided on copper and stainless steel samples to disclose the surface chemistry revolution during wettability transition in air environment.

Green nanosecond laser was proved in this study having a better chance to generate favorable surface structures to induce surface super-hydrophobicity. By scanning the laser 20mm/s with 10μm line spacing, contact angle of highest 161 °at the power of 2.5W was achieved.

This study provides a cost-effective laser solution to form super-hydrophobic surfaces. By analysis surface morphology, wettability and chemistry, an insight into the designing of efficient super-hydrophobic metallic surfaces was presented which will benefit the future study of this phenomenon, providing an effective solution to the practice applications - anti-corrosion, anti-icing and self-cleaning functions.

Chapter 8: Other Applications

Laser processing has many different applications. For example, laser cutting and welding have already been widely used for industrial applications. Among the large amount of various laser applications, surface treatment by nanosecond pulsed laser (laser micro-structuring, laser heating and ablation) of different materials provide an unique way for surface properties modification.

A few of these surface properties modification examples are provided in this chapter. Nanosecond pulsed lasers were responsible for processing on crystal silicon and metallic surfaces. These applications will be divided into three major categories - surface chemical property, optical property and heat transfer performance modification.

8.1 Surface Chemical Property Modification - Laser-assisted Doping

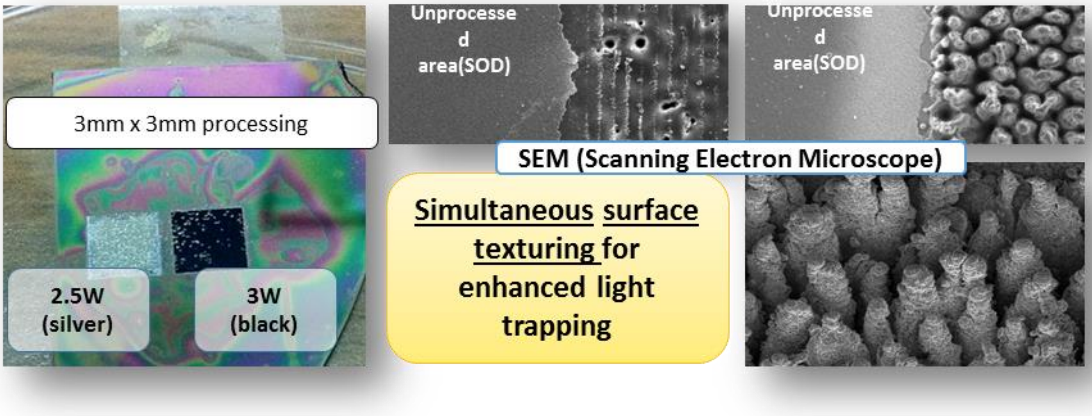

Figure. 8.1.1: Laser-assisted doping of Phosphorus in to P-type B-doped single crystal silicon for photovoltaic application

In Figure 8.1.1, two power cases were studied and result of doping level for each power case is presented. Before laser irradiation, one layer of phosphorus containing SOD (spin-on dopant) layer was spin-coated on top of P-type, B-doped single crystal silicon. In order to form the P-N junction which is essential structure for bulk silicon based solar cell, 532 nm green nanosecond pulsed laser was employed here. After heating up at 200 ℃ for 30mins to remove the solvent in SOD, two different laser powers (2.5W and 3W) were tested, resulting different colored areas - silver and black. Scanning speed, line spacing and repetition rate are 10mm/s, 10μm and 10 kHz, respectively. Simultaneous surface texturing for light trapping was achieved for 3W case. The doping performance was then measured by Secondary Ion Mass Spectroscopy (SIMS) and presented in Figure 8.1.2

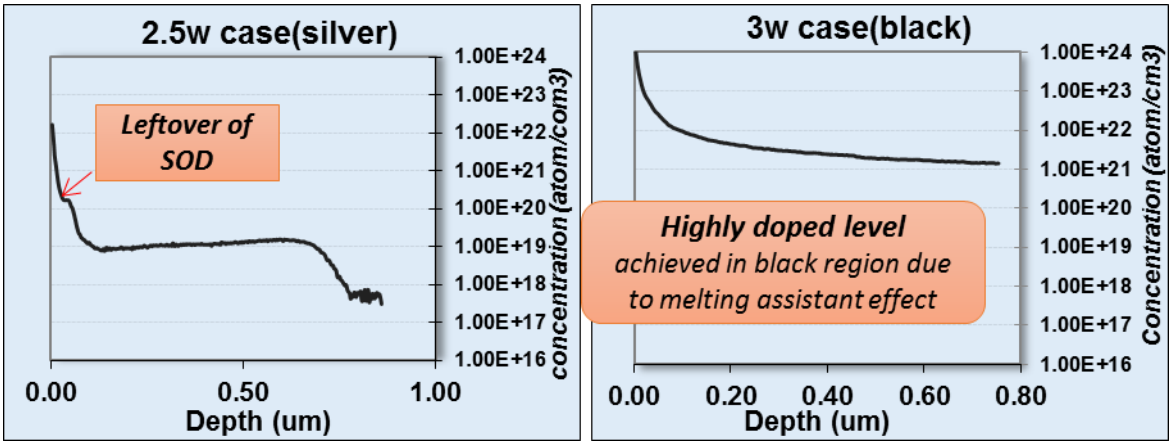

Figure. 8.1.2: SIMS results for laser doping for two different cases. Horizontal axis is the depth from sample surface, vertical axis is the concentration of phosphorus.

8.2 Surface Optical Properties Modification - Colorizing Stainless Steel Surfaces

Surface microstructures will also induce the selective absorption and reflection of certain wavelength of light. The ultimate target can be fully controllable surface optical properties modification.

532 nm nanosecond laser with repetition rate of 10 kHz was used to scan on top of stainless steel (304) surface. Various colored areas were achieved with the variation of scanning parameters. (Figure. 8.2.1)

Figure. 8.2.1: Photograph of different color texturing on stainless steel

In Figure 8.2.1, left image shows detail parameter study by changing the laser scanning speed, line spacing and power. Each area is 3mm by 3mm. Starting from the left bottom corner, the scanning speed is 10mm/s and line spacing is 10μm with laser power of 3.2, 1.5, 1.2, 1, 0.8, 0.6, 0.4, 0.5 and 0.55 watt. Then at the second line to left, the scanning speed is 20mm/s and line spacing is 10μm with laser power of 2, 2.5, 3, 1.5, 1.2, 1, 0.8, 0.6 and 0.55 watt. (Numbers of "mm/s" unit represent scanning speed, numbers with "μm" unit represent line spacing). Starting from the bottom of the third line to the left, with 10mm/s scanning speed and 10μm line spacing, powers are 3.2, 2.5, 1.5 and 0.8 watt. Then 10mm/s and 20μm, powers are 3.2, 2, 1, 0.6 watt.

Then 20mm/s and 20µm, powers are 3.2, 2, 1 and 0.6 watt. Following cases are 50mm/s and 20µm, powers are 3, 2 and 1 watt. Next a few cases are 10mm/s and 30µm, powers are 2.5, 1.8, 1, 1, 0.7 and 0.6 watt. Then 20mm/s and 30µm, powers are 2.5 and 1 watt. Then 50mm/s and 30µm, power is 1.5 watt. After that, more cases for scanning speed of 10mm/s and 20µm line spacing and 20mm/s with 20µm and 20mm/s with 30µm were studied since those regions are more interesting regions.

In Figure 8.2.2, polychromatic optical microscopes and SEM images are presented for a few selected cases. Since the optical microscope images were taken from the top, diffraction grating from different angles is not considered here.

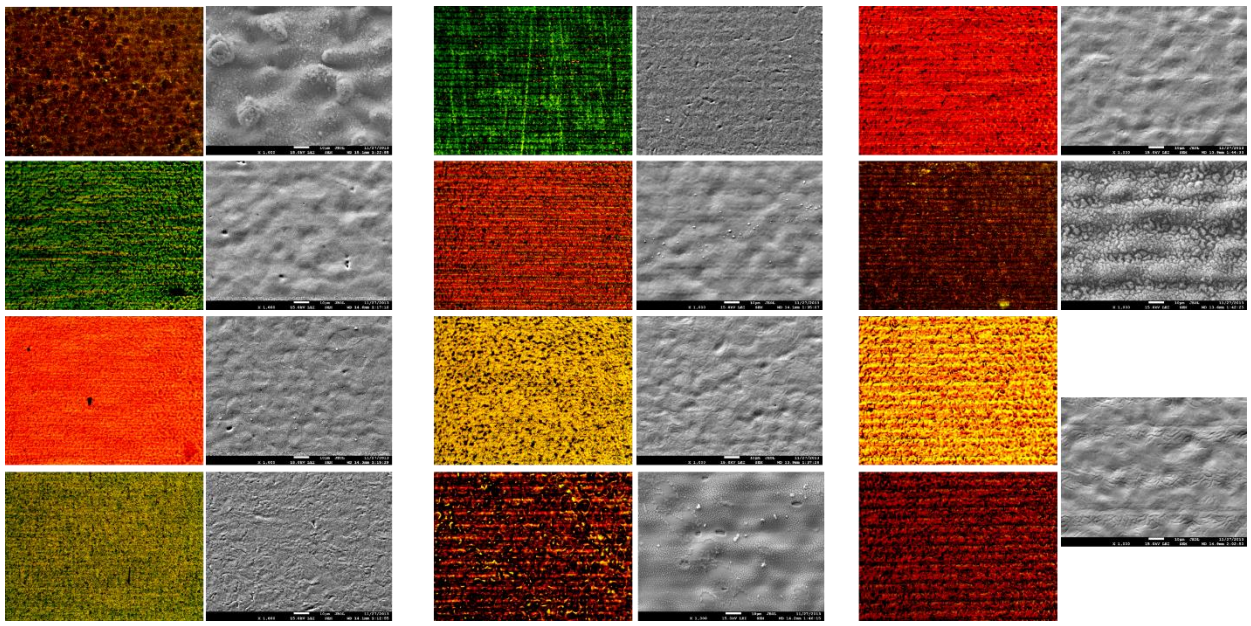

Figure. 8.2.2: Polychromatic optical microscope and corresponding SEM for a few case. Scanning speed, line spacing and laser powers (starting from top right): 10mm/s, 10µm with power of 3.2W, 1W, 0.8W, 0.6W and 0.55W; 20mm/s, 10µm with power of 1W and 0.8W; 10mm/s, 20µm with power of 2W and 1W; 20mm/s, 20µm with power of 3.2W; 10mm/s, 30µm with power of 1W with different illumination light intensity: medium and small (the last SEM correspond to last two microscope images)

Some reflection spectrum of different colored area were also measured in Figure. 8.2.3.

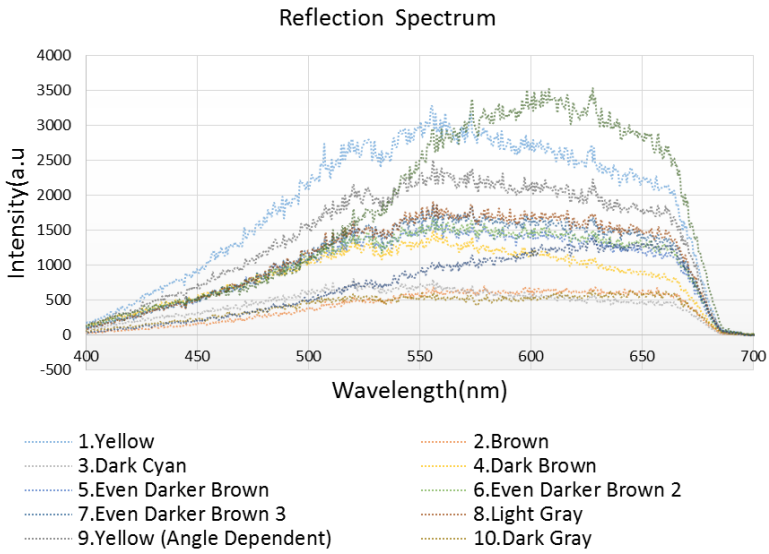

Figure. 8.2.3: Reflection spectrum with different colored stainless steel surfaces.

8.3 Surface Heat Transfer Enhancement - Texturing Semiconductor and Metal

By generating surface roughness, surface heat transfer performance can be enhanced. For example, the radiative heat transfer will be increased by generating black surface due to the increased thermal radiative emissivity. IR camera images of laser structured black silicon and copper are presented in Figure 8.3.1.

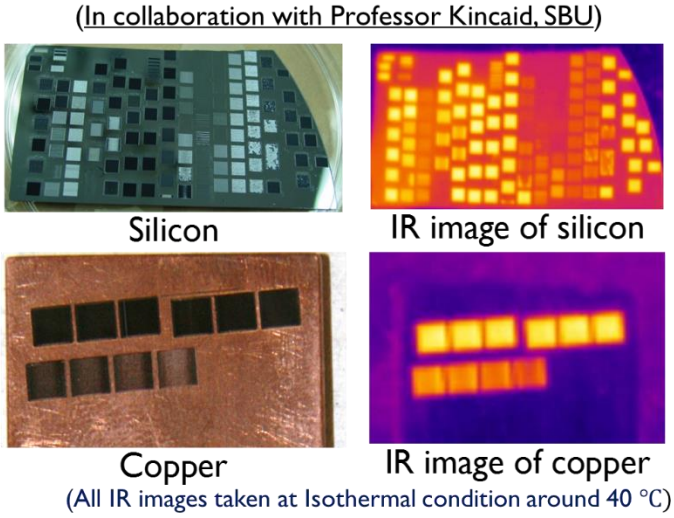

Figure. 8.3.1: IR camera images of laser-textured silicon and copper (By Matt Quigley, 2012)

Rough surfaces also can increase the heat transfer during the boiling of liquid (e.g. water). During pool boiling of water, there exists a sequence describing this phase change phenomenon. Starting with free convection, nucleate, transition and film boiling will follow

successively. Because of the existence of this vapor film boiling region, heat transfer will be affected and reduced first, then climb up after film formation. In order to minimize the heat transfer reduction, rough surfaces can be introduced because surface micro-structures will break and disturb the vapor film formation (Figure. 8.3.2). As a result, heat

Figure. 8.3.2: Enforcing pool boiling heat transfer by reducing film formation on rough surfaces (http://isnps.unm.edu/research/facilities/)

References

1. W. Manly, Fundamentals of liquid metal corrosion, Corrosion, vol. 12, 1956.
2. T. Liu, Y. Yin, S. Chen, X. Chang, and S. Cheng, Super-hydrophobic surfaces improve corrosion resistance of copper in seawater, 2007, Electrochim. Acta, vol. 52, no. 11, pp. 3709–3713
3. J.L. Laforte, M.A. Allaire, J. Laflamme, State of art on power line de-icing, Atmos. Res. 46 (1998) 143–158.
4. Kulinich, SA. and Farzaneh, M. Ice adhesion on super-hydrophobic surfaces. 2009, Appl. Surf. Sci., 255, 8153—8157
5. W. Barthlott and C. Neinhuis, Purity of the sacred lotus, or escape from contamination in biological surfaces, Planta, vol. 202, no. 1, pp. 1-8, 1997
6. Wagner T, Neinhuis C, Barthlott W, Wettability and contminability of insect wings as a function of their surface sculptures. Acta Zool 1996; 77:213-25
7. M. Ma, R.M. Hill, Superhydrophobic surfaces, Curr. Opin. Colloid Interface Sci. 11 (2006) 193-202
8. Z. Guo, W. Liu, B. Su, Superhydrophobic surfaces: from natural to biomimetic to functional. J. Colloid Interface Sci. 353 (2011) 335-355
9. B. Bhushan, M. Nosonovsky, Lotus Effect: Surfaces with Roughness-Induced Superhydrophobicity, Self-Cleaning, and low adhesion. Springer, New York, 2010, pp1437-1524
10. Wenzel, RN. Resistance of Solid Surfaces to Wetting by Water. Ind. Eng. Chem. 1936. 28 (8): 988–994
11. Cassie, ABD; Baxter, S. Wettability of Porous Surfaces. Trans. Faraday Soc. 40. 1944: 546–551
12. Quere, D. Non-sticking Drops. Reports on Progress in Physics 68 (11) 2005: 2495–2532
13. Extrand, C. Criteria for Ultralyophobic Surfaces. Langmuir 68 2005: 2495–2532
14. Nishino T, Meguro M, Nakamae K, Matsushita M and Ueda Y. The lowest surface free energy based on –CF3 alignment, 1999, Langmuir 15 4321-3
15. Hozumi A and Takai O, Preparation of ultra water-repellent films by microwave plasma-enhanced CVD, 1997, Thin Solid Films 303 222-5
16. N.J. Shirtcliffe, G. Mchale, S. Atherton, M.I. Newton, An introduction to superhydrophobicity, Adv. Colloid and Interface Science 161 (2010) 124-138
17. Michielsen S, Lee HJ. Design of a superhydrophobic surface using woven structures. Langmuir. 2007 May 22;23(11):6004-10
18. Liu YY,Wang RH, LuHF, Li L,KongYY,QiKH, et al. Artificial lotus leaf structures from assembling carbon nanotubes and their applications in hydrophobic textiles J Mater Chem2007;17(11):1071–8.
19. Guo, Z., Zhou, F., Hao, J., Liu, W., Effects of system parameters on making aluminum alloy lotus, 2006, J. Colloid Interface Sci. 303, pp. 298-305

20. Tommaso Baldacchini, James E. Carey, Ming Zhou, and Eric Mazur, Superhydrophobic Surfaces Prepared by Microstructuring of Silicon Using a Femtosecond Laser, Langmuir, 2006, 22 (11), 4917-4919
21. D. Bauerle, Laser processing and chemistry, Second Edition, Springer Series in Material Sciences, Vol.1
22. M. Sona, K. Saeid, E. Peter and G.H. Savvas, femtosecond laser irradiation of metallic surfaces: effects of laser parameters on superhydrophobicity, Nanotechnology24 (2013) 415302
23. Kurˇselis K, Kudrius T, Paipulas D, Balachninait˙e O and Sirutkaitis V, Experimental study on femtosecond laser micromachining of grooves in stainless steel, 2010, Lithunian J. Phys. 50 95–103
24. Raillard B, Gouton L, Ramos-Moore E, Grandthyll S, Muller F and Mucklich F, Ablation effects of femtosecond laser functionalization on steel surfaces, 2012, Surf. Coat. Technol. 207 102–9
25. Kurˇselis K, Kiyan R and Chichkov B N, Formation of corrugated and porous steel surfaces by femtosecond laser Irradiation, 2012, Appl. Surf. Sci. 258 8845–52
26. Tang Min, Design and fabrication of super-hydrophobic surfaces by laser micro/nano-processing, Phd thesis, 2012.
27. Johnson, RE; Dettre, Robert H. Contact Angle Hysteresis. 1964. J. Phys. Chem. 68 (7): 1744–1750.
28. Young, T. An Essay on the Cohesion of Fluids.1805. Phil. Trans. R. Soc. Lond. 95: 65–87
29. X. F. Gao, and L. Jiang, Water-repellent legs of water striders. Nature 2004, 432, 36-36
30. H. J. Ensikat, P. Ditsche-Kuru, C. Neinhuis and W. Barthlott, Superhydrophobicity in perfection: the outstanding properties of the lotus leaf. Beilstein J. Nanotechnol. 2011, 2, 152-161
31. Y. Yuan and T. R. Lee, surface science technology, chapter 1: contact angle and wetting properties
32. J. J. Bikeman, Surface Energy of Solid, phy. Status Solidi B, 1965, Vol. 49, no. 1, pp. 3-26
33. de Gennes, Pierre-Gilles. Capillarity and Wetting Phenomena. 2004
34. R. E. Johnson and R. H. Dettre, Contact Angle Hysteresis. III. Study of an Idealized Heterogeneous Surface, J. Phys. Chem., vol. 107, no. 43, pp. 1744–1750, 1963.
35. Lafuma and D. Quere, superhydrophobic states, nature material, 2003, vol.2
36. Y. C. Jung and B. Bhushan, Wetting transition of water droplets on hydrophobic patterned surfaces. Scripta Materialia 57 (2007) 1057–1060
37. Onda T, Shibuichi S, Satoh N, Tsujii K. Super-water-repellent fractal surfaces. Langmuir 1996;12:2125–7.
38. Xu L, Chen W, Mulchandani A, Yan Y. Reversible conversion of conducting polymer films from superhydrophobic to superhydrophilic. Angew Chem Int Ed 2005;44:6009–12

39. Khorasani MT, Mirzadeh H, Kermani Z. Wettability of porous polydimethylsiloxane surface: morphology study. Appl Surf Sci 2005;242:339–45.
40. Jin MH, Feng XJ, Xi JM, Zhai J, Cho KW, Feng L, et al. Superhydrophobic PDMS surface with ultra-low adhesive force. Macromol Rapid Commun 2005;26:1805–9.
41. Lu XY, Zhang CC, Han YC. Low-density polyethylene superhydrophobic surface by control of its crystallization behavior. Macromol Rapid Commun 2004;25:1606–10.
42. Feng XJ, Feng L, Jin MH, Zhai J, Jiang L, Zhu DB. Reversible superhydrophobicity to super-hydrophilicity transition of aligned ZnO nanorod films. J Am Chem Soc 2004;126:62–3.
43. Feng XJ, Zhai J, Jiang L. The fabrication and switchable superhydrophobicity of TiO2 nanorod films. Angew Chem Int Ed 2005;44:5115–8.
44. Shiu J-Y, Kuo C-W, Chen P. Fabrication of tunable superhydrophobic surfaces. Proceedings of SPIE-The International Society for Optical Engineering, vol. 5648; 2005. p. 325–32.
45. Qian BT, Shen ZQ. Fabrication of superhydrophobic surfaces by dislocation-selective chemical etching on aluminum, copper, and zinc substrates. Langmuir 2005;21:9007–9
46. Martines E, Seunarine K, Morgan H, Gadegaard N, Wilkinson CDW, Riehle MO. Superhydrophobicity and superhydrophilicity of regular nanopatterns. Nano Lett 2005;5:2097–103.
47. Feng XJ, Feng L, Jin MH, Zhai J, Jiang L, Zhu DB. Reversible superhydrophobicity to super-hydrophilicity transition of aligned ZnO nanorod films. J Am Chem Soc 2004;
48. Liu H, Feng L, Zhai J, Jiang L, Zhu DB. Reversible wettability of a chemical vapor deposition prepared ZnO film between superhydrophobicity and superhydrophilicity. Langmuir 2004;20:5659–61.
49. Yan H, Kurogi K, Mayama H, Tsujii K. Environmentally stable super water-repellent poly(alkylpyrrole) films. Angew Chem Int Ed 2005;44:3453–6.
50. R. Jagdheesh, B. Pathiraj et al. Laser-induced nanoscale superhydrophobic structures on metal surface. Langmuir 2011, 27, 8464-8469
51. Groenendijk, M., Meijer, J., 2006. Influence of the repetition rate on self organized surface structuring during femtosecond pulsed laser ablation. In: ICALEO 2006 – 25th International Congress on Applications of Laser and Electro-Optics , Scottsdale, AZ, USA, pp. 127–134.
52. Chilamakuri, S., Bhushan, B., Effect of peak radius on design of W-type donut shaped laser textured surfaces. Wear 1999. 230, 118–123.
53. B. K. Nayak, M. C. Gupta, K. W. Kolasinski, formation of nano-textured conical microstructures in titanium metal surface by femtosecond laser irradiation. Appl. Phys. 2008, A 90 399-402
54. V. V. Iyengar and K. Barada et al. Ultralow reflectance metal surfaces ultrafast laser texturing, 2010, Applied Optics Vol. 49, No. 31

55. G. Tang, A. C. Hourd and A. Abdolvand, Nanosecond pulsed laser blackening of copper, Appl. Phys. Lett. 2012. 101, 231902
56. Y. Vorobyev and Chunlei Guo, Colorizing metal with femtosecond laser pulses. Appl. Phys. Lett. 2008. 92, 041914
57. X. H. Li and Q. Xu et al. Al superhydrophobic surfaces fabraicated with femtosecond laser pulses. ICEOE, 2011, V2-109
58. B. Wu, M. Zhou and J. Li et al. Superhydrophobic surfaces fabricated by micrsostructuring of stainless steel using a femtosecond laser. Applied Surface Science (2009) 256, 61-66
59. M. Tang, V. Shim, Z. Y. Pan, Y. S. Choo and M. H. Hong, laser ablation of metal substrates for super-hydrophobic effect. JLMN-Journal of Laser Micro/Nanoengineeing, 2011, Vol. 6, No. 1.
60. V. S. U. Burakov, N. V. Tarasenko, and N. A. Savastenko, Plasma chemistry in laser ablation processes, At. Spectrosc. 2001, vol. 56, no. October 2000, pp. 961–971
61. J. M. Liu, Simple technique for measurements of pulsed Gaussian-beam spot size. 1982, Optics Letters, Vol. 7, No. 5.
62. Wang W, Mei X, Jiang G, Lei Sh and Yang Ch 2008 Effect of two typical focus positions on microstructure shape and morphology in femtosecond laser multi-pulse ablation of metals Appl. Surf. Sci. 255 2303–11.
63. M. Kietzig, S. G. Hatzikiriakos,* and P. Englezos, Patterned Superhydrophobic Metallic Surfaces. Langmuir 2009, 25(8), 4821–4827.
64. F.-M. Chang, S.-L. Cheng, S.-J. Hong, Y.-J. Sheng, and H.-K. Tsao, Superhydrophilicity to superhydrophobicity transition of CuO nanowire films," Appl. Phys. Lett. 2010, vol. 96, no. 11, p. 114101.
65. Bhattacharya, P., Gohil, S., Mazher, J., Ghosh, S. and Ayyub, P. Universal, geometry-driven hydrophobic behaviour of bare metal nanowire clusters, Nanotechnology 2008, 19, 075709.
66. D. Quere, A. Ajdari, Liquid drops: Surfing the hot spot, Nature Material 5 (2006) 429.